

UNCLASSIFIED AU-A107 393 PENNSYLVANIA STATE UNIV UNIVERSITY PARK APPLIED REBE--ETC F/G 7/4  
CORROSION MECHANISM OF CU-9.4 NI-1.7 FE ALLOY IN 3.4 WT% NaCl --ETC(U)  
AUG 81 C KATO  
ANL/PSU/TM-81-181 N00024-79-C-6043

PENNSYLVANIA STATE UNIV UNIVERSITY PARK APPLIED RESE--ETC F/G 7/4  
CORROSION MECHANISM OF CU-9.4 NI-1.7 FE ALLOY IN 3.4 WT% NaCl --ETC(U)  
AUG 81 C KATO  
AML/PSU/TM-81-181  
N00024-79-C-6043

UNCLASSIFIED

NO0024-79-C-6043

NL

142

Abstract





AD A107393

LEVEL II

6

CORROSION MECHANISM OF Cu-9.4 Ni-1.7 Fe ALLOY IN 3.4 WT.%  
NaCl SOLUTION WITH AND WITHOUT SULFIDE CONTAMINATION

Chiaki Kato

Technical Memorandum  
File No. TM 81-181  
August 3, 1981  
Contract No. N00024-79-C-6043

Copy No. 5

DTIC  
ELECTE  
NOV 16 1981  
H

The Pennsylvania State University  
Intercollege Research Programs and Facilities  
APPLIED RESEARCH LABORATORY  
Post Office Box 30  
State College, PA 16801

APPROVED FOR PUBLIC RELEASE  
DISTRIBUTION UNLIMITED

NAVY DEPARTMENT

NAVAL SEA SYSTEMS COMMAND

DTIC FILE COPY

UNCLASSIFIED

SECURITY CLASSIFICATION OF THIS PAGE (When Data Entered)

REPORT DOCUMENTATION PAGE		READ INSTRUCTIONS BEFORE COMPLETING FORM
1. REPORT NUMBER TM 81-181	2. GOVT ACCESSION NO. AD-A107	3. RECIPIENT'S CATALOG NUMBER 393
4. TITLE (and Subtitle) CORROSION MECHANISM OF Cu-9.4 Ni-1.7 Fe ALLOY IN 3.4 WT.% NaCl SOLUTION WITH AND WITHOUT SULFIDE CONTAMINATION.	5. TYPE OF REPORT & PERIOD COVERED Ph.D. Thesis, August 1981	
7. AUTHOR(s) Chiaki/Kato	6. PERFORMING ORG. REPORT NUMBER TM 81-181	
	8. CONTRACT OR GRANT NUMBER(s) N00024-79-C-6043	
9. PERFORMING ORGANIZATION NAME AND ADDRESS The Pennsylvania State University Applied Research Laboratory, P.O. Box 30 State College, PA 16801		10. PROGRAM ELEMENT, PROJECT, TASK AREA & WORK UNIT NUMBERS
11. CONTROLLING OFFICE NAME AND ADDRESS Naval Sea Systems Command Department of the Navy Washington, DC 20362		12. REPORT DATE August 1981
14. MONITORING AGENCY NAME & ADDRESS (if different from Controlling Office)		13. NUMBER OF PAGES 112 pages & figures
		15. SECURITY CLASS. (of this report) Unclassified, Unlimited
		15a. DECLASSIFICATION/DOWNGRADING SCHEDULE
16. DISTRIBUTION STATEMENT (of this Report)  Approved for public release, distribution unlimited, per NSSC (Naval Sea Systems Command), 10/1/81		
17. DISTRIBUTION STATEMENT (of the abstract entered in Block 20, if different from Report)		
18. SUPPLEMENTARY NOTES		
19. KEY WORDS (Continue on reverse side if necessary and identify by block number)  thesis, corrosion, copper, nickel, alloy		
20. ABSTRACT (Continue on reverse side if necessary and identify by block number)  Commercial Cu-9.4 Ni-1.7 Fe alloy has been used successfully as conden- ser tubes in saline environments. It is generally believed that this corro- sion-resistant alloy is protected by the corrosion-product films developed on its surface in sea water. However, under sulfide-contaminated conditions the alloy is known to undergo corrosive attack. The objectives of this research are to determine the corrosion mechanisms which operate when the alloy is immersed in simulated sea water with and without sulfide contamin- ation.		

DD FORM 1473  
1 JAN 73EDITION OF 1 NOV 68 IS OBSOLETE  
S/N 0102-LF-014-6601

UNCLASSIFIED

SECURITY CLASSIFICATION OF THIS PAGE (When Data Entered)

UNCLASSIFIED

SECURITY CLASSIFICATION OF THIS PAGE (When Data Entered)

The corrosion products were developed on the alloy discs which rotated at 800 r.p.m. in 3.4 wt.% NaCl solution with and without sulfide contamination. The developed corrosion products were characterized with X-ray diffraction, SEM, and ESCA studies. Anodic and cathodic polarization curves were measured on the corrosion-product covered alloy surface as well as on the fresh surface to study the electrochemical behavior of the alloy.

The results show that (i) the weight loss of the alloy during immersion in clean 3.4 wt.% NaCl solution increases with time according to a parabolic rate law which is due to the mass-transfer limited anodic metal dissolution rate, and (ii) the cathodic oxygen reduction reaction on the corrosion-product covered alloy in the clean solution is controlled by its poor catalytic nature; however, this catalytic capability is improved by the addition of sulfide during the formation of the corrosion products, thus a high corrosion current is obtained in sulfide-polluted 3.4 wt.% NaCl solution.

SECURITY CLASSIFICATION OF THIS PAGE(When Data Entered)

## ABSTRACT

Corrosion products were developed on commercially available Cu-9.4 Ni-1.7 Fe alloy discs which rotated at 800 r.p.m. in 3.4 wt. % NaCl solution with and without sulfide contamination for various lengths of time up to 10 days. The developed corrosion products were characterized with X-ray diffraction, SEM, and ESCA studies. Anodic and cathodic polarization curves were measured on the corrosion-product covered alloy surface as well as on the fresh surface to study the electrochemical behavior of the alloy.

The results show that (i) the weight loss of the alloy during immersion in clean solution increases with time according to a parabolic rate law which is due to the mass-transfer limited anodic metal dissolution rate, and (ii) the cathodic oxygen reduction reaction on the corrosion-product covered alloy in the clean solution is controlled by the poor catalytic nature of the corrosion products; however, this catalytic capability is improved by the addition of sulfide during the formation of the corrosion products, thus a high corrosion current is obtained in sulfide-polluted 3.4 wt. % NaCl solution.

Accession For	
NTIS GR&I	<input checked="checked" type="checkbox"/>
DTIC TAB	<input type="checkbox"/>
Unannounced	<input type="checkbox"/>
Justification	
By	
Distribution/	
Availability Codes	
Avail and/or	
Dist	Special
A	

## TABLE OF CONTENTS

	Page
Abstract . . . . .	iii
List of Tables . . . . .	vi
List of Figures . . . . .	vii
Acknowledgments . . . . .	x
1. INTRODUCTION . . . . .	1
2. LITERATURE REVIEW AND THEORETICAL CONSIDERATION . . . . .	3
2.1. Thermodynamics of Cu and Cu-Ni Alloy in Sea Water . . . . .	3
2.2. Dissolution Kinetics of Cu and Cu-Ni Alloy in Aqueous Solution Free of Corresponding Ions without Formation of Solid Corrosion Products . . . . .	5
2.3. Formation of Corrosion Product Layers on Cu and Cu-Ni Alloys . . . . .	9
2.4. Corrosion Mechanism of Cu-Ni Alloy in Simulated or Actual Sea Water . . . . .	14
2.5. Influence of Sulfide on Corrosion Mechanism of Cu and Cu-Ni Alloys . . . . .	18
2.5.1. Addition of Sulfide to Simu- lated or Natural Sea Water . . . . .	18
2.5.2. Thermodynamics of Cu and Cu- Ni Alloys in Sulfide-Contami- nated Sea Water . . . . .	20
2.5.3. Corrosion Mechanisms of Cu and Cu-Ni Alloys in Sulfide- Contaminated Sea Water . . . . .	20
3. EXPERIMENTAL . . . . .	25
3.1. Material . . . . .	25
3.2. Surface Preparations . . . . .	25
3.3. Immersion of Cu-Ni Alloy into Simulated Sea Water . . . . .	27
3.4. Rotating Disc Electrode and Electrochemical Cell . . . . .	33
3.5. Experimental Procedure . . . . .	34
3.5.1. Polarization Measurements . . . . .	35
3.5.2. X-ray Diffraction Analysis . . . . .	43

## TABLE OF CONTENTS (Continued)

	Page
3.5.3. ESCA Study of the Corrosion Products . . .	44
3.5.4. SEM Study of the Corrosion Products . . .	45
4. RESULTS . . . . .	46
4.1. X-ray Examination of the Corrosion Product Layers . . . . .	46
4.2. ESCA Examination of the Corrosion Product Layers . . . . .	50
4.3. SEM Examination of the Corrosion Product Layers . . . . .	50
4.4. Polarization Curve Measurements . . . . .	57
4.4.1. Corrosion Current and Potential Determinations . . . . .	57
4.4.2. Polarization Curves on Fresh Surface . . . . .	61
4.4.3. Polarization Curves Measured After Various Periods of Clean Corrosion . . . . .	64
4.4.4. Polarization Curves Measured After Various Periods of Sulfide Corrosion . . . . .	68
5. DISCUSSION . . . . .	77
5.1. Early State of Cu-Ni Alloy Corrosion in Clean 3.4 wt. % NaCl Solution . . . . .	77
5.2. Corrosion of Cu-Ni Alloy in Clean 3.4 wt. % NaCl Solution . . . . .	80
5.3. Effect of Sulfide on Corrosion of Cu-Ni Alloy . . . . .	87
6. CONCLUSIONS . . . . .	95
REFERENCES . . . . .	96
APPENDIX A. MATHEMATICAL INVESTIGATION OF CU DISSOLUTION VIA. $\text{CuCl}_2^-$ IONS IN 3.4 wt. % NaCl SOLUTION . . . . .	100
APPENDIX B. DETERMINATION OF FLOW RATES OF $\text{H}_2$ AND $\text{H}_2\text{S}$ GASES . . . . .	105
APPENDIX C. SULFIDE CONCENTRATION AND pH MEASUREMENTS . . . . .	110



## LIST OF TABLES

Table		Page
1	Composition of the Cu-Ni Alloy . . . . .	26
2	Mechanical Properties of the Cu-Ni Alloy (as Supplied by Hussey Metal Company) . . . . .	27
3	Time Variation of pH and Sulfide Concentration . . . . .	32
4	X-ray Diffraction Analysis of the Total and Outer Part of the Corrosion Products Developed During the 5-day Clean Corrosion Run . . . . .	47
5	X-ray Diffraction Analysis of the Total and Outer Part of the Corrosion Products Developed During the 5-day Sulfide Corrosion Run . . . . .	48
6	ESCA Semi-quantitative Analysis of the Corrosion Products Developed During the 3-day Clean, 3-day Sulfide, and 5-day Sulfide Corrosion Runs (Relative at. %) . . . . .	51
7	Corrosion Currents and Potentials During the Clean and Sulfide Corrosion . . . . .	74

## LIST OF FIGURES

Figure		Page
1	Potential pH diagram (2) for the $\text{Cu-Cl}^- \text{-H}_2\text{O}$ system at 298 K with Cu ion concentration as a variable and 0.56 mole/liter of $\text{Cl}^-$ concentration (the equilibrium lines for hydrogen evolution (line a) and oxygen evolution (line b) have been drawn for gas partial pressure of $10^{-5}$ atm.) . . . . .	4
2	Potential pH diagram (2) for the $\text{Cu-Cl}^- \text{-H}_2\text{O}$ system at 298 K with 4 mg $\text{l}^{-1}$ total dissolved sulfide and 0.56 mole/liter of $\text{Cl}^-$ concentration (the equilibrium line for hydrogen evolution (line a) and oxygen evolution (line b) have been drawn for gas partial pressure of $10^{-5}$ atm.) . . . . .	21
3	Corrosion vessel and gas application system . . . . .	28
4	Schematic of the electrochemical cell and the rotating disc electrode . . . . .	30
5	Current density versus time behavior in de-aerated solution at -350 mV (SCE) . . . . .	37
6	Current density versus time behavior in aerated solution at -350 mV (SCE) . . . . .	39
7	Effect of potential scanning rate on polarization curves . . . . .	42
8	SEM photomicrographs of the top surfaces of the corrosion products after the 5-day clean corrosion; (a) outer surface, (b) outer and inner surfaces . . . . .	52
9	SEM photomicrograph of the cross section of the corrosion products after the 5-day clean corrosion . . . . .	53
10-a	SEM photomicrographs of the top surfaces of the corrosion products after the 5-day sulfide corrosion; (a) outer layer, (b) middle and inner layers . . . . .	54

## LIST OF FIGURES (Continued)

Figure		Page
10-b	SEM photomicrographs of the top surfaces of the corrosion products after the 10-day sulfide corrosion . . . . .	55
11	SEM photomicrograph of the cross section of the corrosion products after the 5-day sulfide corrosion (A, B, and C are positions where X-ray fluorescence chemical analyses are made) . . . . .	56
12	X-ray fluorescence chemical analyses of various portions (A, B, and C in Figure 11) of the corrosion products after 5-day sulfide corrosion . . . . .	58
13	Polarization curves on the fresh surfaces at rotation speed of 8.33 r.p.s. . . . .	59
14	Rotation speed dependence of the polarization curves on the fresh surface . . . . .	62
15	Anodic current density versus square root of the rotation speeds on the fresh surface . . . . .	63
16	Polarization curves measured after various periods of the corrosion . . . . .	65
17	Corrosion current (average weight loss) as a function of the duration of pre-corrosion of the Cu-Ni alloy in 3.4 wt. % NaCl . . . . .	66
18	Time variation of weight loss at open circuit potential for the Cu-Ni alloy stationary electrode (29) and the rotating disc electrode . . . .	67
19-a	Effect of the adherent (inner) layer and the detachable (outer) layer of the corrosion products after the 5-day clean corrosion on the polarization curves (A and A' for 5-day clean, B and B' for stripped 5-day clean, C and C' for fresh surface, and D for Pd-coated stripped 5-day clean) . . . . .	70

## LIST OF FIGURES (Continued)

Figure		Page
19-b	Rotation speed dependence of the anodic polarization curves measured on the inner layer of the 5-day clean corrosion and of the cathodic curves measured on Pd-coated inner layer of the 5-day clean corrosion . . . . .	72
20	Polarization curves measured on the corrosion products after various periods of the sulfide corrosion . . . . .	73
21	Effect of the adherent (inner) layer and of the detachable (outer) layer of the corrosion products after 5-day sulfide corrosion on the polarization curves . . . . .	76
22	A schematic of the cross-section of the corrosion products on the Cu-Ni surface after the 5-day clean corrosion test . . . . .	81
23	A schematic of the cross-section of the corrosion products on the Cu-Ni surface after the 5-day sulfide corrosion test . . . . .	88
24	A schematic model of Cu dissolution in 3.4 wt. % NaCl solution . . . . .	101
25	Flow rate versus pressure head difference for $H_2$ gas . . . . .	106
26	Flow rate versus pressure head difference for $H_2S$ gas . . . . .	107
27	Sulfide concentration versus partial pressure of $H_2S$ gas ( $P_{H_2S}$ ) . . . . .	109
28	Concentration versus potential difference between the sulfide electrode and the saturated calomel reference electrode . . . . .	112

## ACKNOWLEDGMENTS

The author would like to thank his adviser, Dr. Howard W. Pickering, for his valuable assistance throughout the course of his investigation. ESCA studies performed by Dr. Castle of the University of Surrey in England are deeply appreciated. Individual study with Dr. Pigott proved very helpful and is gratefully acknowledged. Financial assistance provided by the Applied Research Laboratory of The Pennsylvania State University under contract with the Naval Sea Systems Command is also gratefully acknowledged.

## 1. INTRODUCTION

Cupro-nickels are widely used as condenser tubes in heat exchangers and desalination systems because they exhibit excellent corrosion resistance in marine environments and good thermal conductivities. It is generally believed that this good corrosion resistance is caused by certain protective films, which are formed on Cu alloys during immersion in sea water. However, in certain situations the cupro-nickels may undergo serious corrosive attack. Such attack has been attributed to contamination of the sea water environment by sulfur. In light of this, it becomes necessary to investigate the corrosion mechanism of this alloy in simulated sea water with and without sulfide contamination.

In this investigation a rotating disc of commercially available Cu-9.4 Ni-1.7 Fe alloy was immersed in 3.4 wt. % NaCl solution to obtain a well-defined fluid flow condition, such as may be obtained in actual condenser tubes. When the alloy is immersed in the solution, anodic metal dissolution and cathodic oxygen reduction reactions take place on the alloy surface at equal rates and corrosion product layers are developed. Polarization curves (current vs. potential relations) were studied on the corrosion-product covered Cu-Ni alloy as well as on the freshly prepared alloy. Thus, the rate controlling step of the cathodic and anodic reactions during the Cu-Ni alloy corrosion is deduced.

Addition of sulfide in the solution was conducted with a gas mixture of  $H_2$  and  $H_2S$  during the alloy immersion. The developed

corrosion products were again studied by the polarization curve measurements and the effects of the sulfide in the corrosion mechanism are discussed.

## 2. LITERATURE REVIEW AND THEORETICAL CONSIDERATION

### 2.1. Thermodynamics of Cu and Cu-Ni Alloy in Sea Water

Equilibrium potential-pH diagrams for pure Cu metal can be constructed from electrochemical and thermodynamic equilibrium data. These diagrams give the thermodynamically stable form of the metal along with the stability of ionic and passivating species as a function of electrode potential and pH. The diagrams for pure Cu in sea water at 298 K were constructed by some investigators (1,2). A typical potential-pH diagram is shown in Figure 1. The formation of cuprous oxide and copper chloride compounds is possible on Cu in sea water of pH 7 to 8 at potential of 0V (S.H.E.).\* These compounds are often found in corrosion products of Cu in sea water (3). However, the formation of these products is sensitive to pH, electrode potential, and concentration (activity) of Cu ions and other species in solution, so they may be altered by local change of pH, turbulence of solution, and/or biological activity. Besides the thermodynamic requirements, the kinetics of formation (nucleation and growth) of films may play important roles in determining the actual corrosion products developed as Cu corrodes in sea water (1).

In order to obtain more useful potential-pH diagrams for practical use, the electrochemical hysteresis method has been developed (4,5). This method involves plotting a series of potentiokinetic polarization

---

\* Potential measured on Cu in sea water is about 0V versus Standard Hydrogen Electrode (S.H.E.) (6).



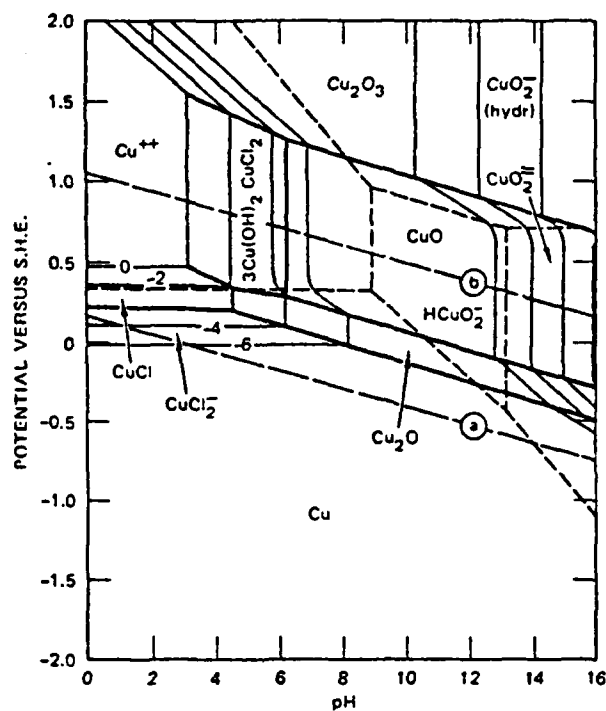


Figure 1. Potential pH diagram (2) for the Cu-Cl<sup>-</sup>-H<sub>2</sub>O system at 298 K with Cu ion concentration as a variable and 0.56 mole/liter of Cl<sup>-</sup> concentration (the equilibrium lines for hydrogen evolution (line a) and oxygen evolution (line b) have been drawn for gas partial pressure of 10<sup>-5</sup> atm.).

curves in the solution of interest at various pH values, and is used for construction of potential-pH diagrams of an alloy which may show a complex metal dissolution mechanism. Efird (6) constructed these diagrams for Cu-Ni alloys in sea water. From his experiments it was found that the Cu-Ni alloys show passivation polarization curves in sea water a passivation region exists when the pH is higher than 8.5 for Cu-10 Ni alloy and 8.0 for Cu-30 Ni alloy. The corrosion potential measurements show that in sea water (pH=7.9) the Cu-30 Ni alloy is in the passive region. The Cu-10 Ni alloy is initially in the active region; however, the corrosion potential is shifted to the passive region after  $5.4 \times 10^4$  seconds (15 hours) of immersion. This potential shift into the passive region may be due to surface enrichment of Ni caused by preferential dissolution of Cu from the matrix.

## 2.2. Dissolution Kinetics of Cu and Cu-Ni Alloy in Aqueous Solution Free of Corresponding Ions without Formation of Solid Corrosion Products

The simplest case of a metal dissolution is the dissolution of pure Cu without formation of solid corrosion products. Bockris et al. (7) studied dissolution of pure Cu in 1 N HCl flowing solution at 300 K by measuring anodic polarization curves. Two distinct linear regions are found with slopes of  $65 \pm 2$  mV/current decay (at lower overvoltage) for diffusion-controlled dissolution and  $158 \pm 2$  mV/current decay (at higher overvoltage) for activation-controlled dissolution. These slopes can be numerically obtained (7) by equating the rate of dissolution to the rate of diffusion from the electrode to the bulk solution. The rate of dissolution into a solution containing no Cu can be shown to be:

$$i = \frac{k_M^0 C_M f_a(E) \frac{FD_M^+/\delta}{k_M^0 + f_c(E) + (FD_M^+/\delta)}}{(1)}$$

where

- $i$ : current density
- $k_M^0, k_M^0$ : electrochemical rate constant ( $M \rightleftharpoons M^+ + e^-$ )
- $f_a(E)$ :  $\exp[(1-\beta)FE/RT]$
- $f_c(E)$ :  $\exp[-\beta FE/RT]$
- $F$ : Faraday's constant
- $\beta$ : transfer coefficient
- $E$ : electrode potential
- $R$ : gas constant
- $T$ : absolute temperature
- $D_M^+$ : diffusion coefficient of  $M^+$  in solution
- $\delta$ : diffusion layer thickness

In Equation (1), if  $k_M^0 + f_c(E) \gg FD_M^+/\delta$ , the slope of  $\log i$  vs.  $E$  becomes  $2.3RT/F$  and is diffusion-controlled and independent of  $\beta$ . If  $(FD_M^+/\delta) \gg k_M^0 + f_c(E)$ , the slope is  $2.3RT/\beta F$  and is activation-controlled. The slopes obtained by Equation (1) agree with the slopes from the polarization measurements. Since Equation (1) was developed for the dissolution of univalent metal, it is reasonable to conclude that pure Cu corrodes solely to  $Cu^+$  in HCl solution.

Bonfiglio et al. (8) also investigated the anodic dissolution of Cu from a Cu rotating disc electrode in HCl solution. They found a chloride concentration dependence of the polarization curve in addition to the diffusion dependence.

An analytical expression obtained is:

$$i = X \frac{k_M^o}{k_{M^+}^o} \cdot \exp\left(\frac{FE}{RT}\right) \cdot \sum_{j=1}^n \frac{\gamma_j}{K_1} [Cl^-]^j \quad (2)$$

where

$$X: 0.62FD^{2/3}v^{-1/6}\omega^{1/2}$$

$$\gamma_j: [CuCl_j^{(j-1)-}]/[Cu^+][Cl^-]^j$$

$K_1$ : stability constant of CuCl

D: average diffusion coefficient of all species involved

$\omega$ : electrode rotating speed

$v$ : kinematic viscosity

This expression describes dissolution of metal with the formation of complex species (such as CuCl, CuCl<sub>2</sub><sup>-</sup>, and CuCl<sub>3</sub><sup>=</sup>). When the solubility product of CuCl is satisfied by anodic high over potential, then the anodic current becomes independent of potential and shows an anodic limiting current density (i.e.,  $i_L$ , anodic).

$$i_{L, \text{ anodic}} = X [CuCl]_s \sum_{j=1}^n \frac{\gamma_j}{K_1} [Cl^-]^{j-1} \quad (3)$$

where  $[CuCl]_s$  is the cuprous chloride saturation concentration

From these experiments and other literature (7-11), it can be concluded that at somewhat low overvoltages the anodic dissolution of pure Cu is controlled by the diffusion of cuprous chloride complex ions from the electrode surface toward the bulk solution.

In contrast to the dissolution of pure metal, when a single-phase binary alloy is anodically dissolved in an aqueous solution, the mode of dissolution may be:

- (a) simultaneous dissolution of both constituent metals,
- (b) preferential dissolution of the less noble metal of the alloy with the more noble metal accumulating in the surface layers (7,11-13).

For the latter mode, it is necessary that the difference between the single electrode potentials of the two constituent metals be sufficiently large, e.g., Cu-Au (12) and Cu-Zn (13) alloys.

Occurrences of preferential dissolution in the Cu-Ni alloy system can be seen under special conditions. The preferential dissolution of Ni from the Cu-Ni alloy (up to 90 at. % Cu) in an electrolyte ( $\text{H}_2\text{SO}_4\text{-H}_3\text{PO}_4\text{-H}_2\text{O}$ ) under high anodic overvoltages (2000 mV), resulting in Cu enrichment of the alloy surface, can be detected by AES and XPS analyses (14). However, in hydrochloric acid at somewhat lower anodic overvoltages (100-500 mV), it may be possible to form areas of pure Ni rather than Cu on the surface of alloys containing more than 55 at. % and less than 90 at. % of Cu. This was observed by differential polarographic techniques (7) and rotating disc electrode polarization measurements (11).

Occurrence of preferential dissolution depends on the electrolyte, the composition of the alloy (activity of each component in the alloys), the exchange current density of each component, and the electrode potential. It is still unknown whether the Cu-Ni alloys undergo preferential dissolution in sea water under freely corroding conditions.

### 2.3. Formation of Corrosion Product Layers on Cu and Cu-Ni Alloys

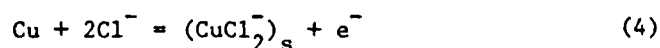
When a piece of Cu or its alloy is exposed to air, it is possible to develop a thin layer of oxide on the surface. Castle (15) observed a thin Ni oxide layer on a Cu-rich Cu-Ni alloy after exposing it to air. If these pure Cu or Cu alloys with the air-formed oxide are immersed in an aqueous environment formation of a much thicker corrosion product layer can be expected. It is important to discuss the mechanism of this layer formation since protective layer formation is generally believed to be responsible for the low corrosion rate of Cu and Cu alloys in sea water.

When pure Cu is immersed in distilled water, corrosion product layers will develop on the Cu surface at the free corrosion potential. Kruger (16,17) studied the formation of the corrosion product layers on Cu in distilled water by ellipsometry. When water was saturated with a helium-1% oxygen mixture, only a  $\text{Cu}_2\text{O}$  layer grew with parabolic kinetics. However, when the dissolved  $\text{O}_2$  content was increased, a  $\text{CuO}$  layer grew on the  $\text{Cu}_2\text{O}$  layer. It was speculated that the formation of the  $\text{CuO}$  film may retard the  $\text{Cu}_2\text{O}$  layer growth rate, but unfortunately the growth rates of the  $\text{Cu}_2\text{O}$  and  $\text{CuO}$  layers were not measured.

It is known that light has a marked influence on the oxidation and layer growth process in water. Investigations (16) have been conducted comparing the layer growth rates on illuminated and unilluminated surfaces of Cu single crystals. After  $1.04 \times 10^4$  seconds Cu had a layer thickness of roughly 12 nm, while the unilluminated surface had an average thickness of 50 nm. On the basis of Mott's theory (18), illumination would cause a flow of electrons from

the semiconductor ( $\text{Cu}_2\text{O}$ ) layer into the metal. A flow of electrons in this direction when the film is growing would inhibit growth.

The formation of a  $\text{Cu}_2\text{O}$  film on pure Cu has also been reported in NaCl solution. North and Pryor (20) exposed Cu specimens to boiling 0.5 M NaCl solution and the developed corrosion products were determined to be mainly  $\text{Cu}_2\text{O}$  by X-ray diffraction. The dissolution behavior of pure Cu in NaCl solution is similar to that in HCl solution (7,8, 10,11), exhibiting concentration polarization (Tafel slope of  $2.3RT/F$ ) and a chloride concentration dependence (21). Since concentration polarization is observed, pure Cu dissolves only by the generation of soluble cuprous ions. Thus a direct formation of  $\text{Cu}_2\text{O}$  corrosion product can not be expected (22). The reason for the formation of  $\text{Cu}_2\text{O}$  on the freely corroding Cu surface may be explained by hydrolysis of  $\text{CuCl}_2^-$  within the diffusion layer (21,6). The important reactions preceding hydrolysis are



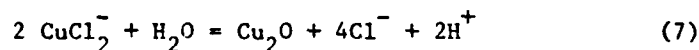
and



where the subscripts s and b refer to the species at the Cu/solution interface and bulk solution, respectively. The rate determining step (rds) (5) is the diffusive transport of  $\text{CuCl}_2^-$  from the interface to the bulk solution. By using Fick's first law,  $i$  (corrosion current) can be expressed as:

$$i = \frac{zFD[\text{CuCl}_2^-]_s}{\delta} \quad (6)$$

where [species] is a concentration of the species at the metal surface. The accumulated  $\text{CuCl}_2^-$  tends to react in the diffusion layer as follows:



If the solubility product of  $\text{Cu}_2\text{O}$  ( $1.25 \times 10^{-15}$  at room temperature) is exceeded,  $\text{Cu}_2\text{O}$  should begin to precipitate. According to calculations by Bacarell and Griess (21), the  $\text{Cu}_2\text{O}$  film would be formed if the corrosion rate is higher than  $1.61 \times 10^{-5} \text{ } \mu\text{m-sec}^{-1}$  (20 mpy) at room temperature under suitable assumptions of  $D$  and  $\delta$ .

The accumulation of  $\text{CuCl}_2^-$ , thus formation of  $\text{Cu}_2\text{O}$ , can also be expected by looking at the concentration gradients of the various ionic species in the diffusion layer. By modifying the models and assumptions proposed by Ateya and Pickering (23), concentrations of  $\text{Cl}^-$ ,  $\text{Na}^+$ , and  $\text{CuCl}_2^-$  at the metal surface as a function of the thickness of the diffusion layer,  $\delta$ , can be expressed as follows (the derivations of the following equations are seen in Appendix A):

$$[\text{Cl}^-]_s = [\text{Cl}^-]_b - \frac{2i}{D_{\text{Cl}^-}F} \left[ \frac{[\text{Cl}^-]_b \delta - \frac{Y\delta^2}{4}}{[\text{Cl}^-]_b - \frac{Y\delta}{2}} \right] \quad (8)$$

$$[\text{Na}^+]_s = [\text{Na}^+] - \frac{1}{2} Y\delta \quad (9)$$

$$[\text{Cu}_2^-]_s = \frac{1}{D_{\text{CuCl}_2^-}F} \left[ \frac{[\text{Cl}^-]_b \delta - \frac{Y\delta^2}{4}}{[\text{Cl}^-]_b - \frac{Y\delta}{2}} \right] \quad (10)$$



where

$$Y = \frac{1}{F} \left( \frac{2}{D_{Cl^-}} - \frac{1}{D_{CuCl_2^-}} \right)$$

If a copper disc is rotating at a certain rotation speed, the diffusion layer thickness,  $\delta$ , can be calculated by utilizing the Levich equation (24):

$$\delta = 0.643 \omega^{-1/2} \nu^{1/6} D_{CuCl_2^-}^{1/3} \quad (11)$$

where

$\omega$ : rotation speed in Hz

$\nu$ : kinematic viscosity

Using typical values of  $\omega$ ,  $\nu$ , and  $D_{CuCl_2^-}$  (16.67 Hz,  $0.01 \text{ cm}^2\text{-sec}^{-1}$ , and  $0.6 \times 10^{-5} \text{ cm}^2\text{-sec}^{-1}$  (25)), one obtains the diffusion layer thickness of  $1.3 \times 10^{-3} \text{ cm}$  (13  $\mu\text{m}$ ). Utilizing Equation (10) and approximate value of  $\delta$ ,  $i$ ,  $D_{Cl^-}$ , and  $D_{CuCl_2^-}$  ( $1.5 \times 10^{-3} \text{ cm}$ ,  $20 \mu\text{A-cm}^{-2}$ ,  $2.03 \times 10^{-5} \text{ cm}^2\text{-sec}^{-1}$  (25), and  $0.6 \times 10^{-5} \text{ cm}^2\text{-sec}^{-1}$ ) one has  $[CuCl_2^-]_s \sim 4.5 \times 10^{-5} \text{ mol-l}^{-1}$ .

Similarly, the concentration of  $Cl^-$  can be calculated; however, due to the small value of  $Y$  and corrosion current density ( $20 \mu\text{A-cm}^{-2}$ ) the concentration of  $Cl^-$  at the metal surface is approximately the same as the value of the bulk solution ( $0.6 \text{ mol-l}^{-1}$ ). By knowing the values of  $[Cl^-]$  and  $[CuCl_2^-]$  one can obtain  $[Cu^+]$  from the equilibrium constant,  $2.8 \times 10^{-6}$  (21) for the reaction  $CuCl_2^- = Cu^+ + 2Cl^-$ . Since the obtained value of  $[Cu^+]$  ( $\sim 3.5 \times 10^{-12} \text{ mole-l}^{-1}$ ) exceeds the solubility products

---

\*The corrosion current of the freshly prepared Cu-Ni alloy is determined to be about  $20 \mu\text{A-cm}^{-2}$  in Chapter 4, and the corrosion current of the pure Cu is probably close to  $20 \mu\text{A-cm}^{-2}$ .

of  $\text{Cu}_2\text{O}$  ( $1.25 \times 10^{-15} \text{ mole-l}^{-1}$  (21)), the formation of  $\text{Cu}_2\text{O}$  can be occurred.

It was mentioned earlier that the  $\text{CuO}$  layer is produced on top of the  $\text{Cu}_2\text{O}$  layer if pure  $\text{Cu}$  is immersed in a solution containing  $\text{O}_2$  (16). However, when additional environmental factors, such as  $\text{CO}_2$  gas and/or  $\text{NaCl}$  solution, are introduced, formation of  $\text{Cu}(\text{HCO}_3)_2$  (1,19) and/or  $\text{Cu}_2(\text{OH})_3\text{Cl}$  (1) layers on the  $\text{Cu}_2\text{O}$  layer become possible. The mechanism for the formation of cuprous compounds is not well-understood (22).

Similar to pure  $\text{Cu}$ ,  $\text{Cu}_2\text{O}$  and  $\text{Cu}_2(\text{OH})_3\text{Cl}$  are developed on the  $\text{Cu-10 Ni}$  alloy in actual or simulated sea water (26-28). In addition, at elevated temperature in sea water, it is possible to find  $\text{Mg}$ ,  $\text{Al}$ , and  $\text{Si}$  compounds which are deposited from sea water (28).

The  $\text{Cu}_2\text{O}$  and  $\text{Cu}_2(\text{OH})_3\text{Cl}$  corrosion products consist of at least two layers (26,28). The inner layer is relatively thin and dense and adheres to the alloy surface. The outer layer has a porous appearance and is extremely flaky. One investigator (27) reported that the corrosion products consist of four layers and each layer has its own composition. Although some  $\text{Cu-Ni}$  alloys contain up to 30 wt. %  $\text{Ni}$ , the existence of any  $\text{Ni}$  oxide has rarely been reported. Chemical analyses (ESCA (26), Auger (26), and cross-sectional X-ray fluorescence studies (27)) of the corrosion products developed in simulated sea water show that the total concentration of  $\text{Fe}$  and  $\text{Ni}$  is at its highest in the interface region between the inner and outer layer.

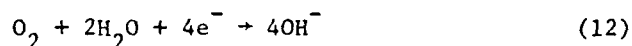
In order to discuss the preferential dissolution of Ni from the alloy, it is necessary to measure the Ni concentration in the electrolyte solution as well as in the corrosion products. Popplewell et al. (28) measured the Ni concentration in the corrosion product using atomic absorption by etching off a series of corrosion product layers. They found that as much as 30 at. % Ni and 10 at. % Fe of total cations were dissolved in the  $\text{Cu}_2\text{O}$  lattice produced on the Cu-10 Ni-1.5 Fe alloy. Also Ni and Fe contents in the solution were always less than the contents in the bulk alloy. The combined concentrations of Ni and of Fe in both the solid corrosion products and the solution appeared to be around 10% Ni and 1.5% Fe, which matches very closely the alloy composition.

From these observations, it can be suggested that the Cu, Ni, and Fe atoms leave the alloy simultaneously with a rate proportional to the composition of the bulk alloy; however, the alloying elements (Ni and Fe) have a higher tendency to stay in the solid corrosion products than does Cu, resulting in preferential dissolution of Cu ions from the corrosion products.

#### 2.4. Corrosion Mechanism of Cu-Ni Alloy in Simulated or Actual Sea Water

When the Cu-Ni alloy is immersed in sea water, the Cu and Ni atoms become ions in the liquid phase and/or produce solid corrosion products on the alloy surface. Under this condition, cathodic reactions must accompany the anodic reactions to obtain electrical neutrality of the system. Typical anodic reactions are Reactions (4)

and (7). The only cathodic reaction<sup>\*</sup> is:



The electrons released at the anodic site move through the metal to the cathodic site where they are consumed by the cathodic reaction. After the surface of the alloy is covered with a well-developed corrosion product,  $\text{Cu}^+$ ,  $\text{Ni}^{++}$  and  $\text{Fe}^{++}$  ions and electrons which form at the alloy/oxide interface must migrate through the oxide layer toward the oxide/solution interface. Otherwise anions ( $\text{O}^{--}$ ) move from the solution side to the alloy/oxide interface to proceed the alloy corrosion.

For the discussion of the aqueous corrosion mechanism, it must be determined first whether the corrosion process is governed by the anodic or cathodic reactions, and second if a mass (or  $\text{e}^-$ ) transfer step or the electrochemical reaction controls the corrosion process. In addition, it may be necessary to investigate the role of alloying elements, since lower corrosion rates of Cu-Ni alloy than of pure Cu have been observed in sea water (30,31). This may lead to consideration of the preferential dissolution mechanism (12,13).

Weight loss measurement is one of the most comprehensive techniques of studying the corrosion mechanism, since the weight loss with time relationship gives a corrosion rate which may provide some information on the rate-controlling-process. However, the available data

---

<sup>\*</sup>  $2\text{H}^+ + 2\text{e}^- \rightarrow \text{H}_2$  occurs at a potential lower than -700 mV (SCE) at pH=8. The corrosion potential of the Cu-Ni alloy lies about -300 to -200 mV (SCE) in NaCl solution at room temperature (6,27,29).

on the corrosion rate of the Cu-Ni alloy is limited. This may be due to poor reproducibility (32) and time-consuming experiments.

Kato et al. (29) measured the weight loss of the Cu-10 Ni-1.7 Fe alloy in stagnant 3.4 wt. % NaCl solution. They showed the corrosion rate of the alloy decreases with time of immersion, while the film weight increases according to the parabolic rate law. This parabolic relation suggests that the growth of the film follows a transport-limited mechanism.

The corrosion rate can be measured by techniques other than weight loss. Macdonald et al. (33) obtained the corrosion rate in sea water by noting polarization resistance variation with time. They found a strong dependence of the corrosion rate on oxygen concentrations, suggesting a cathodic control process at low oxygen concentrations (lower than the air-saturated concentration, 6.6 mg/l). However, at high oxygen concentrations the corrosion process is controlled by the anodic reaction.

Polarization resistance measurements were also conducted by several investigators (20,28,32), and the results provide insight into the defect structure of the corrosion product layer, such as why the  $\text{Cu}_2\text{O}$  film which forms on the Cu-Ni-Fe alloy is more protective than that formed on pure Cu. It is reported that the crystal structure of  $\text{Cu}_2\text{O}$  is cubic and is a highly defective p-type semiconductor (34). This structure may be described as being one in which some  $\text{Cu}^+$  ions are missing from the cation lattice sites and in which the otherwise deficient positive charge is balanced by a single positive charge in the vicinity of each cation vacancy. This positive charge can be

associated with one of the neighboring cations, i.e., one  $\text{Cu}^+$  in the vicinity of the cation vacancy is written as  $\text{Cu}^{2+}$ . This kind of defect structure has low ionic resistance, because of a significant number of cation vacancies, and also because the positive hole concentration and mobility is high, i.e., the electron exchange between  $\text{Cu}^+$  and  $\text{Cu}^{2+}$  ions requires very little energy. The electronic resistance is also low. Both the ionic and electric resistivities of the films are increased by alloying elements of Ni and Fe. The alloying elements enter the sites of cation vacancies as  $\text{Ni}^{2+}$  and  $\text{Fe}^{3+}$  and reduce the number of cation vacancies and the positive hole concentrations. According to Pryor and North (32), the higher the Ni concentration in the film, the higher the resistivity of the films. Through simultaneous measurement of the resistivities and of the Ni concentrations in the films, these investigators proved the Ni concentration dependence of the film resistivities.

This defect structural model is now one of the most useful explanations for the low corrosion rate of the Cu-Ni alloys. According to this model, alloying elements such as  $\text{Ni}^{++}$  and  $\text{Fe}^{++}$  remain in the  $\text{Cu}_2\text{O}$  layer. However, Auger (26), ESCA (26), and X-ray fluorescence studies (27) showed high concentrations of the alloying elements in the  $\text{Cu}_2(\text{OH})_3\text{Cl}$  layer, thus disagreeing with the defect structural model. Moreover, the linear relationship of current vs. potential, essential to the defect structural model, has not always been found by other investigators (27,29).

Kato et al. (29) and Ijsseling (27) measured polarization curves on the fresh Cu-Ni alloy surface, as well as on the corroded

alloy surface (prior to the polarization measurements the alloy is corroded at the free corrosion condition). They found that both the anodic (metal dissolution) and the cathodic (oxygen reduction) curves were more polarized with increasing corrosion time. Since, in the presence of the layers the cathodic half-cell reaction is more polarized than the anodic reaction, the rate controlling process is suggested to be the cathodic reaction (29). Kato et al. (29) further studied the importance of the inner adherent and the outer flaky parts of the corrosion products.

## 2.5. Influence of Sulfide on the Corrosion Mechanism of Cu and Cu-Ni Alloys

### 2.5.1. Addition of Sulfide to Simulated or Natural Sea Water

It has been observed that Cu and Cu-Ni alloys may undergo severe corrosion attack by the sulfide pollution of sea water (33,35-39). In spite of the considerable amount of work in this area, no satisfactory corrosion mechanism has been proposed. This is probably due to experimental difficulties in controlling the electrochemical parameters (e.g., pH, sulfide concentration, oxygen concentration). The addition of sulfide to oxygen-saturated sea water causes an oxidation of dissolved sulfide, resulting in a decrease in the concentration of oxygen that is available for reaction and a change in the pH of the sea water. In natural sea water, levels of total sulfide range from <1 to 30 ppm (40,41). The pH of sea water is normally in the range of 8.2 to 7.5. As a rare extreme, the pH in polluted waters

may approach 7.0 (40). This pH variation will, in turn, affect the ratio  $\text{H}_2\text{S}:\text{HS}^-:\text{S}^{--}$ . At pH 7.0 and 313 K, in 3.4 wt. % NaCl solution a typical mole ratio  $\text{H}_2\text{S}:\text{HS}^-:\text{S}^{--}$  is calculated to be  $1:2:10^{-9}$  under suitable assumptions (38).

In order to obtain experimental conditions close to those of polluted sea water, several methods of sulfide addition into simulated sea water have been conducted. One of these methods is an addition of  $\text{Na}_2\text{S}$  into NaCl solution. In an experiment by Bates and Popplewell (38), 10 ppm of total sulfide was added each working day for  $1.44 \times 10^4$  seconds to the deaerated pH 7.3 solution. The level of total sulfide was determined by intermittent manual potential measurements with glass and sulfide electrodes. Typically, the concentration of sulfide would fall to 5 ppm within  $1.08 \times 10^4$  seconds.

A second method used to supply sulfide to the NaCl solution is an application of an  $\text{H}_2\text{S}/\text{H}_2$  gas mixture (37). The hydrogen sulfide gas is absorbed by the water as  $\text{H}_2\text{S}$ ,  $\text{HS}^-$ , and  $\text{S}^{--}$  in a proportion determined by the water's pH; but for a given partial pressure of  $\text{H}_2\text{S}$  the total sulfide concentration remains constant.

A third method involves a contamination with colloidal sulfur and polysulfides. Since natural sea water contains both dissolved oxygen and sulfide, the sulfide oxidation reaction is possible and produces polysulfides ( $\text{H}_2\text{S}$ ,  $\text{HS}_n^-$ ,  $\text{S}_n^{--}$ , where  $n \geq 2$ ), elemental sulfur, and other even more highly oxidized species, such as sulfurous acid. Syrett et al. (33) investigated the corrosion of the Cu-Ni alloys by the sulfide oxidation products.



### 2.5.2. Thermodynamics of Cu and Cu-Ni Alloys in Sulfide-Contaminated Sea Water

Potential-pH diagrams for Cu in 4 mg/l sulfide-contaminated sea water at 25°C has been derived by Verink (2) and is shown in Figure 2. At pH 7 to 8 and a corrosion potential between -500 and -800 mV (SCE),  $\text{Cu}_2\text{S}$  is the thermodynamically stable phase. At about the same pH, if the corrosion potential increases to -300 mV (SCE),  $\text{Cu}_2\text{O}$  becomes stable.  $\text{CuS}$  can also be formed if the pH of the solution decreases to less than 7 and the potential is above -600 mV (SCE). The corrosion potential of Cu and Cu-Ni alloys in sulfide-contaminated sea water (pH 7-8), measured by various investigators, ranges from -800 to -500 mV (SCE) (2,36) and, thus, is in the stable  $\text{Cu}_2\text{S}$  phase region; however, these investigators found  $\text{Cu}_2\text{O}$  and  $\text{CuS}$ , as well as  $\text{Cu}_2\text{S}$ , by X-ray diffraction analysis. Moreover, Mor and Beccaria (35,36) identified using chemical separation techniques  $\text{Cu}_{1.8}\text{S}$ ,  $\text{Cu}_7\text{S}_4$ , and  $\text{Cu}_3(\text{OH})_2(\text{CO}_3)_2$  in addition to  $\text{Cu}_2\text{S}$ ,  $\text{CuS}$ , and  $\text{Cu}_2\text{O}$ . The discrepancy between the stable corrosion compounds obtained from the theoretical pH-potential diagrams and the experimental findings is probably due to local potential and pH changes, the method of sulfide addition, and the formation kinetics of oxide-sulfide corrosion products.

### 2.5.3. Corrosion Mechanisms of Cu and Cu-Ni Alloys in Sulfide-Contaminated Sea Water

It has been reported by several investigators (37,38,42) that Cu and Cu-Ni alloys corrode more rapidly in the presence of sulfide and air, than in the presence of air or sulfide alone. There are a couple of proposed explanations for this behavior. Bates and

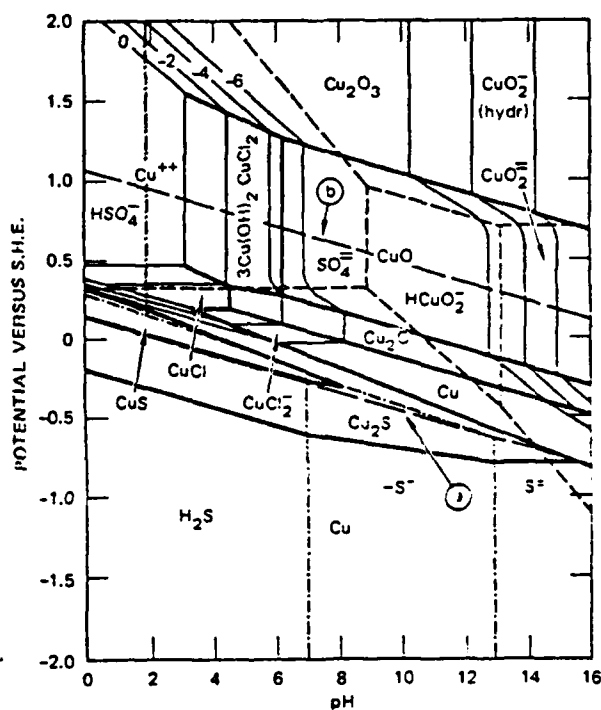
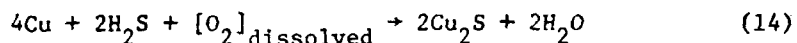


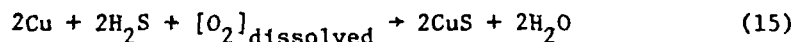
Figure 2. Potential pH diagram (2) for the Cu-Cl<sup>-</sup>-H<sub>2</sub>O system at 298 K with 4 mg l<sup>-1</sup> total dissolved sulfide and 0.56 mol/liter of Cl<sup>-</sup> concentration (the equilibrium line for hydrogen evolution (line a) and oxygen evolution (line b) have been drawn for gas partial pressure of 10<sup>-5</sup> atm.).

Popplewell (38) observed  $\text{Cu}_2\text{O}$  formation on the Cu-Ni alloys in aerated NaCl solution, and  $\text{Cu}_2\text{S}$  formation in deaerated sulfide-contaminated solution. Ionic diffusivities and electrical conductivity are high for  $\text{Cu}_2\text{S}$  compared with  $\text{Cu}_2\text{O}$ . Thus, the corrosion rate in deaerated sulfide solution is higher than in aerated solution. The corrosion products developed in sulfide- and oxygen-contaminated solution are a mixture of  $\text{Cu}_2\text{O}$ ,  $\text{Cu}_2\text{S}$ , and  $\text{CuS}$ . Since  $\text{Cu}_2\text{O}$  and  $\text{Cu}_2\text{S}$  have different crystal structures, the resultant mixed crystals would have mismatches at the crystal interfaces that could result in structural defects large enough to permit mass transport of moisture with dissolved molecular and ionic species. Thus, the corrosion rate in the presence of sulfide and oxygen is much higher than in sulfide or oxygen alone (38).

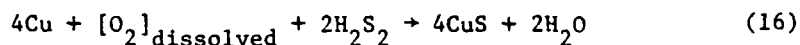
Another explanation was made by Syrett (37). In the presence of  $\text{H}_2\text{S}$  or  $\text{HS}^-$ , Cu probably suffers some attack by the reaction:



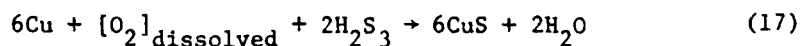
and/or



may occur. When relatively large amounts of both oxygen and sulfide are present, a loosely adherent  $\text{CuS}$  layer is predominately found on the alloy surface.  $\text{CuS}$  flakes are also found on the bottom of the test chamber, showing the nonprotecting nature of the corrosion products. This corrosion product may also be expected to form by the reactions,



and/or



The species  $\text{H}_2\text{S}_2$  and  $\text{H}_2\text{S}_3$  are products of sulfide oxidation reactions, and are well-known to be aggressive to Cu (37). Syrett (37) also predicted from Reactions (14) and (15) that when Cu is corroding at low sulfide levels, the oxygen content is in excess of that needed for Reactions (14) and (15), and corrosion is controlled by the supply of sulfides or sulfide oxidation products to the metal surface. At high sulfide levels (>250 ppb S), the corrosion reactions are controlled by the supply of oxygen.

Syrett et al. (43) also investigated the corrosion of Cu-Ni alloy in sulfide-polluted sea water. They measured the corrosion rates and corrosion potentials and showed that the accelerated corrosion of the Cu-Ni alloy in sulfide-polluted sea water appeared to arise from a shift of the corrosion potential to values active enough so that hydrogen evolution became a cathodic process. In deaerated sea water without sulfide addition (dissolved oxygen content  $0.045 \text{ mg/dm}^3$ ), the corrosion potential is always more noble than  $-0.3 \text{ V (SCE)}$ . Oxygen reduction is the only possible cathodic reaction, and therefore, the corrosion rates are low. On the other hand, in deaerated water containing as little as  $0.85 \text{ mg/dm}^3$  sulfide, the corrosion potential drops to values in the range  $-0.45$  to  $-0.72 \text{ V (SCE)}$  for which hydrogen ion reduction is possible, and the corrosion rate increases by about one order of magnitude. The overall anodic reaction changes from cuprous oxide formation in the

sulfide-free system to cuprous sulfide formation in the sulfide-polluted system. In effect, sulfide ion converts the Cu-Ni alloy from an essentially passive state (protective corrosion product) into an active state (nonprotective corrosion product) that also introduces an additional cathodic process (hydrogen evolution).

### 3. EXPERIMENTAL

#### 3.1. Material

The Cu-Ni alloy sample was obtained from the Hussey Metal Company in Pittsburgh, Pennsylvania, in the form of a sheet with a thickness of 0.17 cm. The compositional analysis and mechanical properties of this alloy, as determined by the Hussey Metal Company and The Mineral Constitution Lab\*, are listed in Tables 1 and 2. The Hussey Metal Company conducted a final heat treatment of this alloy solutionized at 850°C for 30 minutes followed by quenching and in this investigation the sample was used as received. In most field processes this alloy is utilized in the solutionized condition without additional heat treatments.

#### 3.2. Surface Preparations

In order to obtain reproducible data the surface preparation procedures are important. Therefore, in this investigation the following procedures were employed:

- (1) Cutting of the 0.95 cm disc specimens from the alloy sheet, and mounted into a plexiglass sample holder.
- (2) Abrading the sample surface with SiC emery papers successively through 600 grit.
- (3) Chemically dissolving the air-formed oxide in a deaerated 10 volume percent  $H_2SO_4$  solution.

---

\* Located at The Pennsylvania State University.

Table 1  
Composition of the Cu-Ni Alloy

Elements	Weight % (by Hussey)	Weight % (by M.C.L.)
Cu	Balance	
Ni	9.40	9.41
Fe	1.70	1.93
Mn	0.32	
Zn	0.15	
Pb	0.02	
P	0.02	
S	0.02	
Ag	N.D. *	
O	N.D. *	

\* None detected.

Table 2  
Mechanical Properties of the Cu-Ni Alloy (as supplied  
by Hussey Metal Company)

Tensile Strength	$2.90-2.97 \times 10^8$ (Pa)
0.5% Extension Yield Point	$5.07-5.52 \times 10^7$ (Pa)
Elongation in 5.08 cm	39.0-42.5 (%)
Hardness (Rockwell)	20 (B Scale)
Bend	180 (degree with- out fracture)

- (4) Degreasing in acetone for 600 seconds. This was followed by rinsing in a methanol solution and drying in a desiccator for a  $9.0 \times 10^4$  second period.

This surface preparation procedure was initially employed by North and Pryor (20) and Popplewell et al. (28) and was reported to give relatively good reproducibility.

### 3.3. Immersion of Cu-Ni Alloy into Simulated Sea Water

A polished Cu-Ni alloy disc mounted into a plexiglass sample holder (Figure 3 and Figure 4, parts 4, 11, and 12) was immersed into a corrosion vessel which contained 1 liter of 3.5 wt. % NaCl solution at pH of 7.5 (adjusted with diluted NaOH) at room temperature ( $298 \pm 3K$ ). Schematic of the vessel is shown in Figure 3. During the immersion the disc specimen was rotated at 14.17 r.p.s. with an electrical motor and belt. There were two conditions under which the formation of corrosion product layers was conducted.



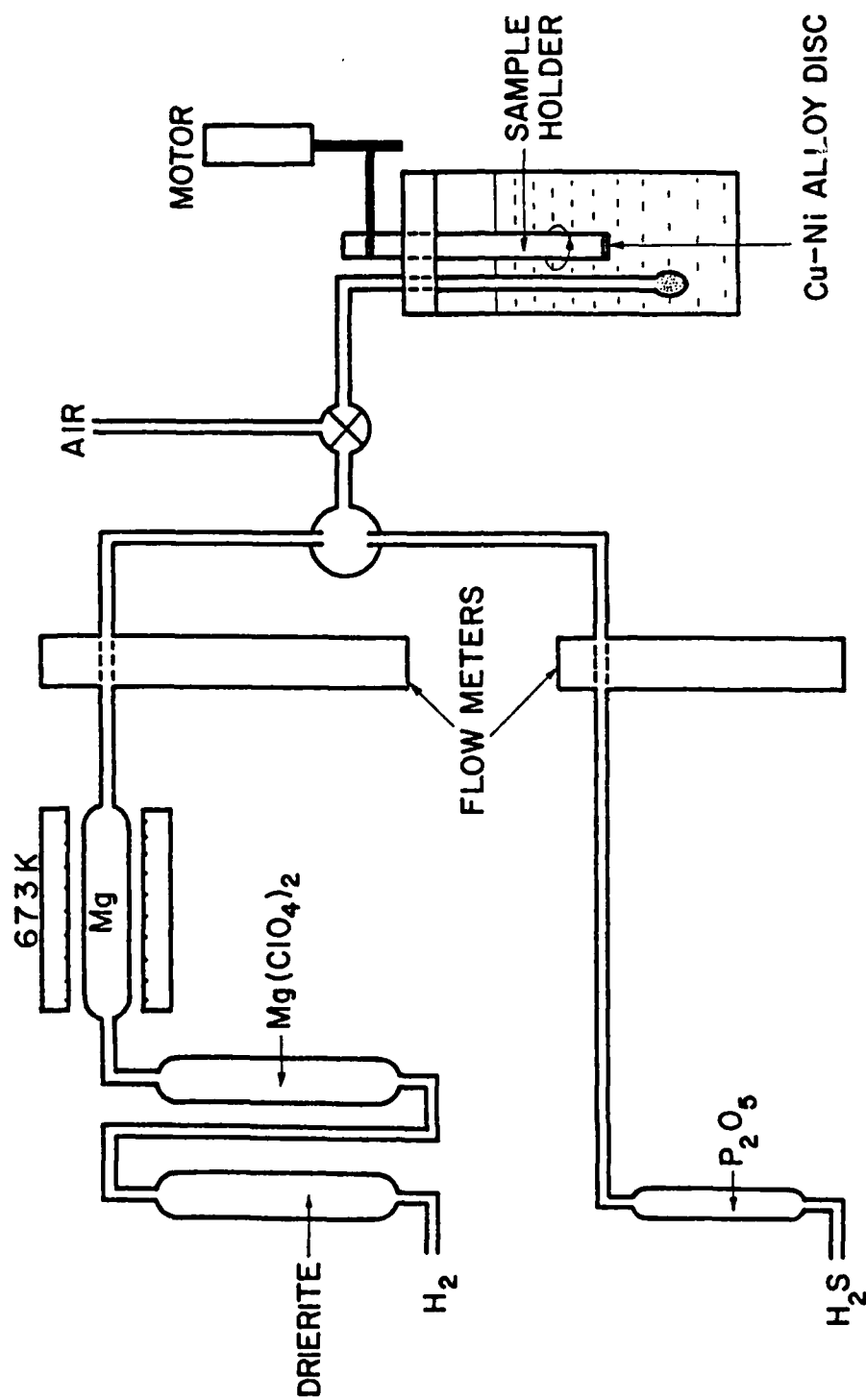
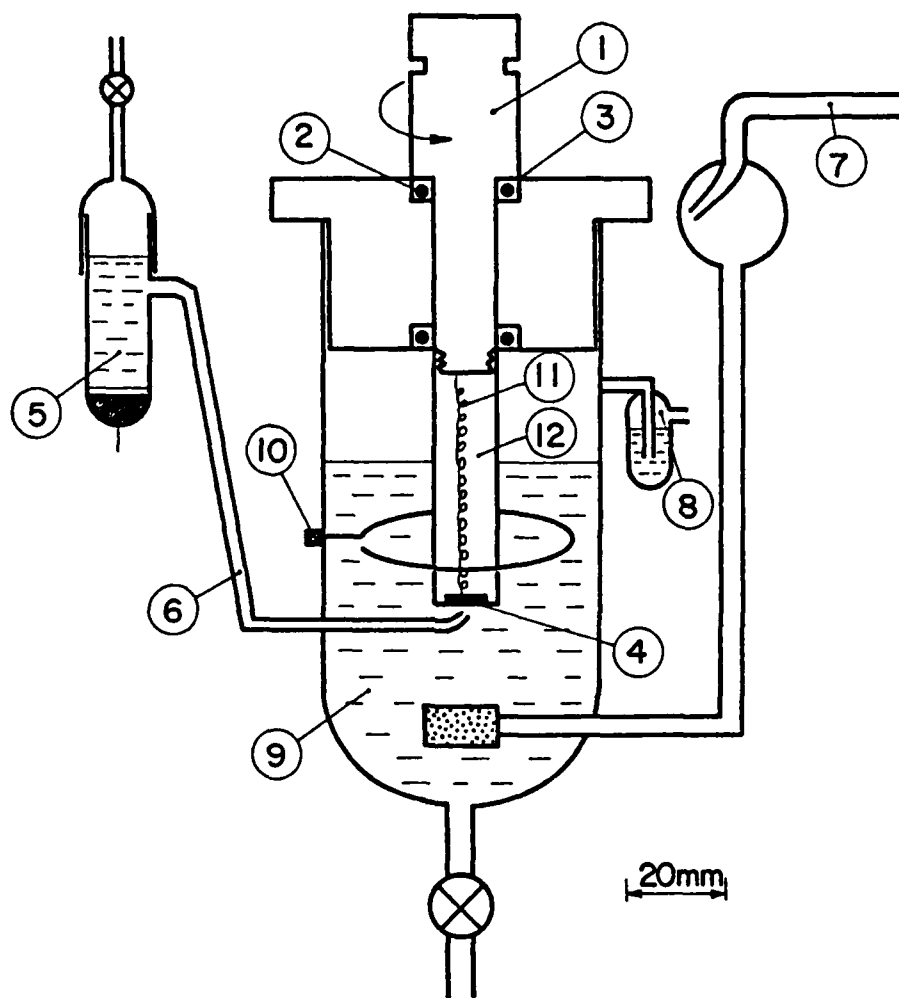


Figure 3. Corrosion vessel and gas application system.

Figure 4. Schematic of the electrochemical cell and the rotating disc electrode.

1. Stainless steel shaft
2. Carbon bearing
3. Working electrode terminal
4. Cu-Ni disc sample
4. Saturated Calomel electrode (S.C.E.)
6. Agar salt bridge
7. Gas (purified  $N_2$  or air)
8. Gas outlet
9. Electrolyte solution (3.4 wt. % NaCl solution)
10. Pt counter electrode
11. Cu lead wire for working electrode
12. Plexiglass sample holder



(1) Formation of layers in aerated NaCl solution (clean corrosion); the aeration was conducted by applying water-saturated compressed air to the corrosion vessels throughout the immersion period (see Figure 3). The solution was changed every  $6.05 \times 10^5$  seconds (7 days) in order to avoid an accumulation of Cu and Ni ions in the solution. In the following text this process is called clean corrosion.

(2) Formation of layers in sulfide-contaminated solution (sulfide corrosion); the sulfide contamination was conducted with the insertion of a  $H_2/H_2S$  gas mixture into the corrosion vessel shown in Figure 4. The purification of  $H_2S$  gas involved drying with phosphorus pentoxide. Silicon oil was used as a pressure head in the  $H_2S$  flow meter. The  $H_2$  gas was dried by Drierite (anhydrous calcium sulfate) and magnesium perchlorate followed by a magnesium trap heated to 673 K to remove oxygen. In the  $H_2$  flow meter, dibutyl phthalate was used as a pressure head.

The formation of corrosion product layers was conducted by a cycle of air saturation and sulfide contamination. Initially, the Cu-Ni alloy sample was immersed in aerated solution for  $8.28 \times 10^4$  seconds (23 hours). After that the sample was removed from the vessel and the solution was changed to deaerated (the deaeration was conducted with purified  $N_2$  gas for  $1.8 \times 10^3$  seconds) 3.4 wt. % NaCl solution of pH 7.5. Then, a gas mixture of the purified  $H_2S$  and  $H_2$  was applied to the solution for  $1.2 \times 10^3$  seconds to get saturation of sulfide ions followed by immersion of the samples for  $3.6 \times 10^3$  seconds. During immersion sufficient flow rates of the gases were maintained to keep

the sulfide concentration constant in the deaerated solution. A determination of flow rates of  $H_2$  and  $H_2S$  gas was conducted by measuring the concentration of sulfide and pH for various flow rates of the gases. Details of the determination of the flow rates and sulfide concentration measurements are described in Appendices B and C. The flow rates were adjusted so that the concentration of sulfide was always in the range of 5 to 8 ppm and pH was between 7.0 and 7.5. Typical time variations of pH and sulfide concentration in the 3.4 wt. % NaCl solution bubbled with the  $H_2/H_2S$  gas mixture at the adjusted flow rates are shown in Table 3. In the beginning of the  $H_2/H_2S$  application the pH decreases, while the sulfide concentration increases; however, after 900 seconds these values become stable.

Table 3  
Time Variation of pH and Sulfide Concentration

Time (sec)	pH	$[S]^*$ mol/l	ppm
0	7.50	0	0
900	7.10	$4.3 \times 10^{-5}$	1.40
1800	7.05	$2.2 \times 10^{-4}$	7.04
3600	7.05	$1.9 \times 10^{-4}$	6.00
5400	7.00	$2.3 \times 10^{-4}$	7.36

\* Total sulfide, including  $H_2S$ ,  $HS^-$ , and  $S^{--}$ .

The cycle of aerated NaCl solution for  $8.28 \times 10^4$  seconds and deaerated NaCl solution with  $H_2/H_2S$  gas for  $3.6 \times 10^3$  seconds was repeated for various periods up to  $8.64 \times 10^5$  seconds (10 days). In the following content this process is called sulfide corrosion.

#### 3.4. Rotating Disc Electrode and Electrochemical Cell

To study the polarization behavior of the Cu-Ni alloy, a rotating disc electrode and a three electrode cell were employed. A schematic of the cell and the rotating disc electrode assembly is shown in Figure 4. The Cu-Ni specimen was placed into a plexiglass holder and electrical contact was made between the specimen and a stainless steel shaft by a Cu lead wire. The shaft was supported by two frictionless carbon bearings\* mounted into a plexiglass to complete the circuit. The stainless steel shaft was rotated by an electrical motor and a belt. This arrangement allows only the Cu-Ni alloy contact with the solution. The rotation speed was checked periodically with a Photo Tachometer\*\* to maintain constant speed. The other elements of the cell were a saturated calomel electrode, a platinum counter electrode, and a gas bubbling system.

The saturated calomel electrode consists of a well of mercury with a platinum wire protruding through the bottom of the tube and making electrical contact with the mercury.  $HgCl$  is added on top of the mercury and the cell is filled with saturated KCl solution. A small glass arm of the cell is connected to an agar salt bridge constructed of

---

\* Obtained from Metallized Carbon Corporation, Ossining, New York.

\*\* Model 36, Pioneer Electric & Research Corporation, Forest Park, Ill.

one-quarter inch Tygon tubing at the end of which is a glass Luggin capillary. The salt bridge contains the saturated KCl solution containing 3 weight percent of agar. The long-term stability of the reference electrode potential was checked periodically by a glass electrode in a buffered solution.

For the polarization measurements 3.4 wt. % NaCl solution (double distilled water) was employed throughout the investigation. The pH of the solution was adjusted to 7.5 by adding a dilute NaOH solution at 298 K. Water-saturated air or  $N_2$  gas was bubbled into the cell throughout the tests to insure oxygen saturation or deaeration. The  $N_2$  gas was purified in the following way:

- (1) Removal of moisture by drierite.
- (2) Removal of  $O_2$  by Cu shavings at 573 K.

In order to determine the polarization curves, an Aardvark potentiostat (Model V) was used. This potentiostat can apply a constant potential between the surface of the Cu-Ni alloy and the saturated calomel electrode, and measure current flow between the Cu-Ni alloy and the platinum counter electrode. The method used in this investigation is called "Potentistatic polarization" in which the potential was changed and the corresponding current was measured. An Aardvark potential scanning unit was used to vary the potential at a constant rate.

### 3.5. Experimental Procedure

After the formation of the corrosion product layers under various conditions, the Cu-Ni specimens and adherent corrosion products were characterized and analyzed by several techniques.

### 3.5.1. Polarization Measurements

The polarization curves were measured on 0<sup>\*</sup>, 3,5, and 10 day corroded specimens under both the clean and sulfide-contaminated conditions. Immediately after the end of the immersion, the Cu-Ni specimen with the plexiglass holder was rinsed with pure water and placed in either a deaerated<sup>†</sup> or an aerated 3.4 wt. % NaCl solution of the electrochemical cell (Figure 4). Transfer of the sample was quick enough so that the surface of the specimen remained wet,<sup>††</sup> thereby avoiding crack formation in the corrosion products (44). Then, a potential of -350 mV (SCE) was applied by potentiostat. At this potential only oxygen reduction was expected to occur. A current transient lasted 10<sup>3</sup> seconds prior to reaching a quasi-steady state value. A true steady state was not reached in 8.64x10<sup>4</sup> seconds (24 hours). Figures 5 and 6 show the behavior of the current vs. time at -350 mV on various samples. After getting a quasi-steady state cathodic current, the potential scanning unit was used to shift the potential at the rate of 0.03 mV-sec<sup>-1</sup> to -150 mV (SCE). Kato et al. (44) showed an effect of potential scanning rate on the anodic polarization curves. Within a small overvoltage region (-200 mV to -100 mV (SCE)) the anodic polarization curve was independent of the potential scanning rate. Similar experiments were conducted in aerated and deaerated solution using a

---

\* These specimens were not subjected to open-circuit immersion, i.e., they are fresh (as polished) specimens.

† Deaeration was conducted before the polarization measurements for 1800 seconds by purging with purified N<sub>2</sub> gas.

†† Except for the 0-day samples, which were directly placed in the cell after the surface cleaning process.



Figure 5. Current density versus time behavior in deaerated solution at  $-350$  mV (SCE).

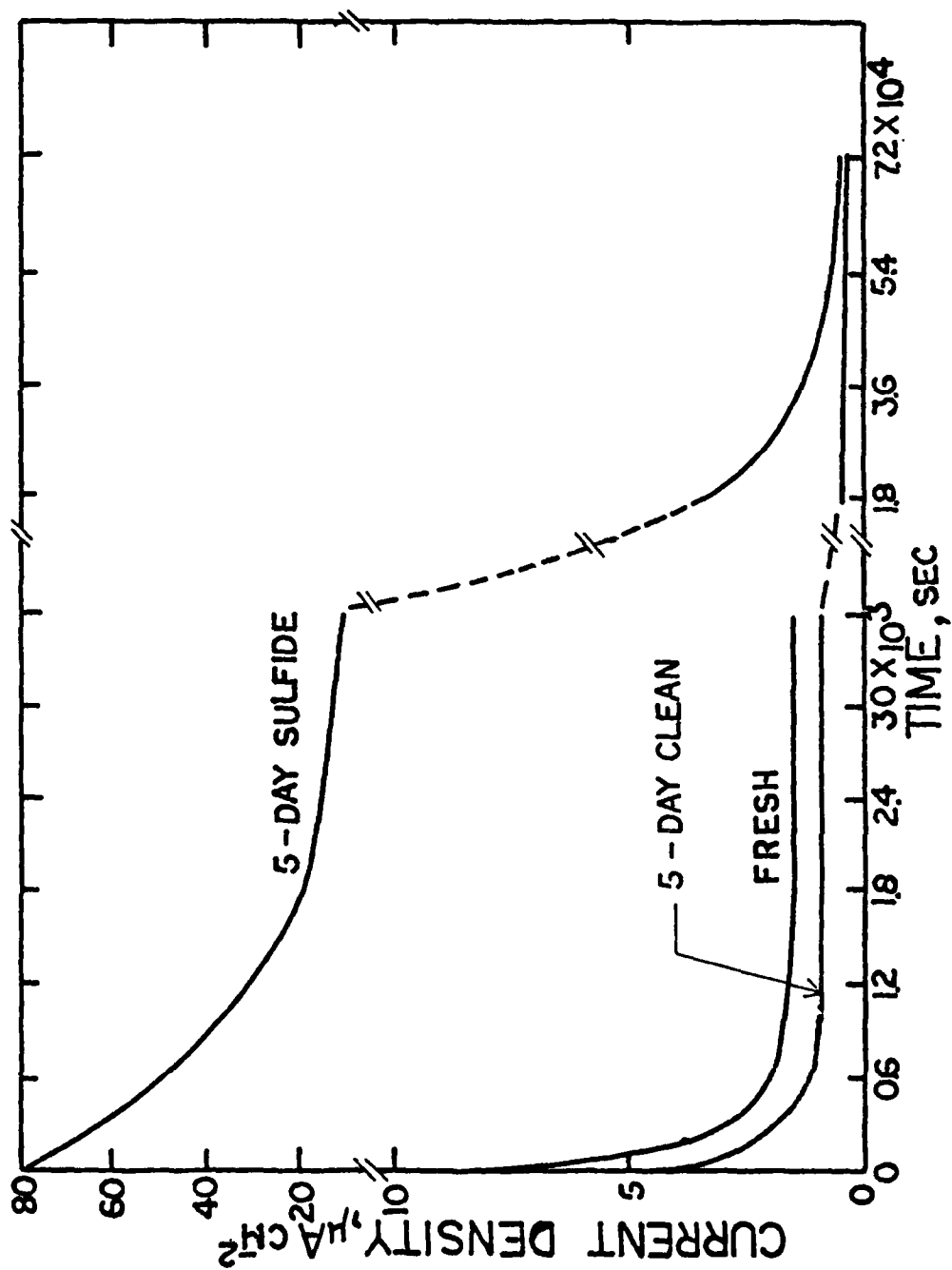
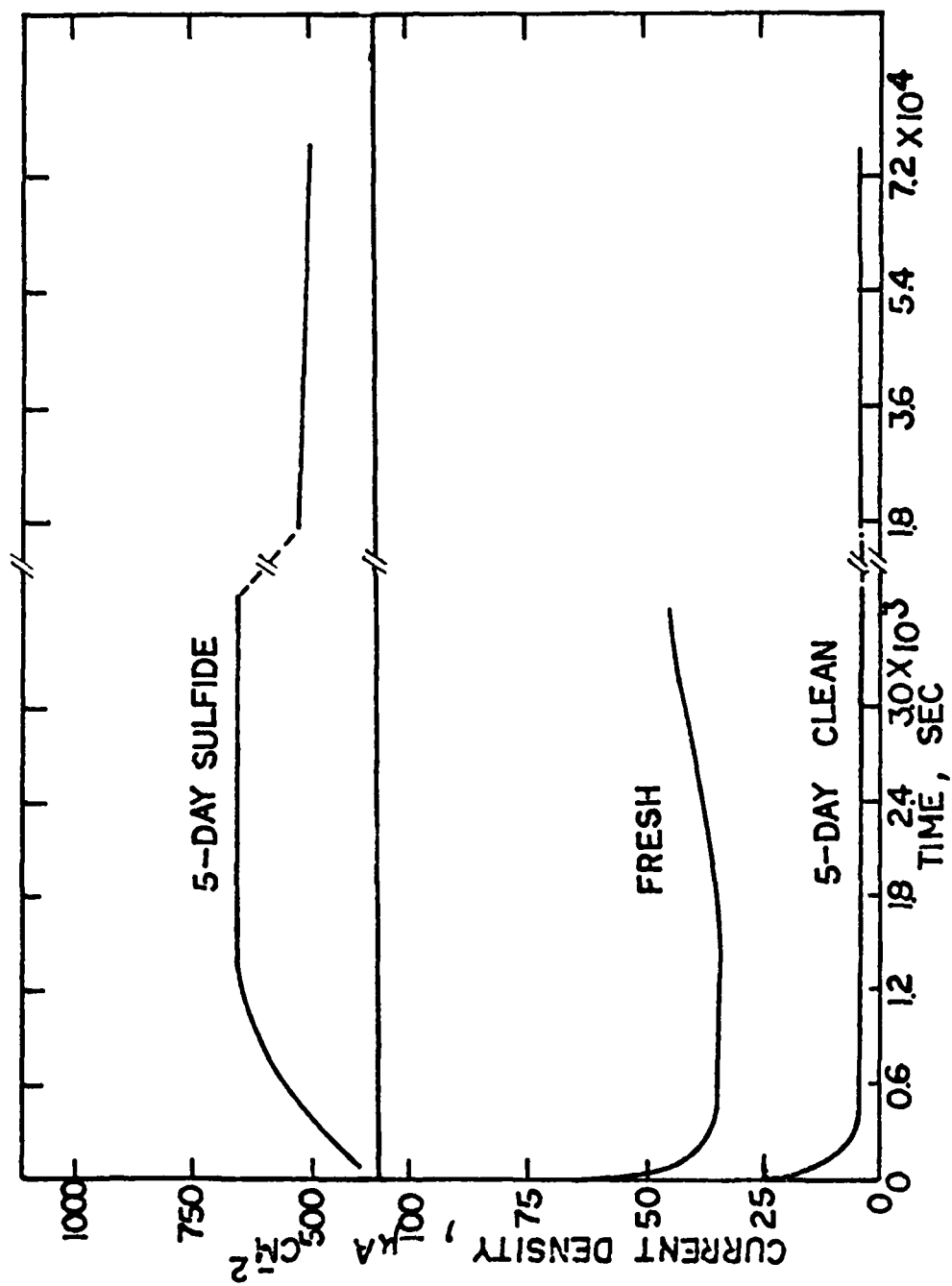


Figure 6. Current density versus time behavior in aerated solution at  $-350$  mV (SCE).



"steady state" method\* and scanning rates of  $0.03 \text{ mV-sec}^{-1}$  and  $0.3 \text{ mV-sec}^{-1}$ . These runs showed that identical results are obtained for the steady state and the  $0.03 \text{ mV-sec}^{-1}$  scanning rate measurements in both the aerated and deaerated solutions (Figure 7). The higher scanning rate,  $0.3 \text{ mV-sec}^{-1}$  showed also identical behavior in the deaerated solution; however, greater polarization occurs in the aerated solution. Thus, the polarization curves were henceforth made with the potential scanning rate of  $0.3 \text{ mV-sec}^{-1}$ . The rotation speed employed during polarization curve measurements was 8.33 r.p.s.<sup>†</sup> However, in some measurements various speeds up to 33.3 r.p.s. were used to investigate the rotation speed dependence of the polarization curve. The rotation speeds were periodically checked with a photo tachometer.

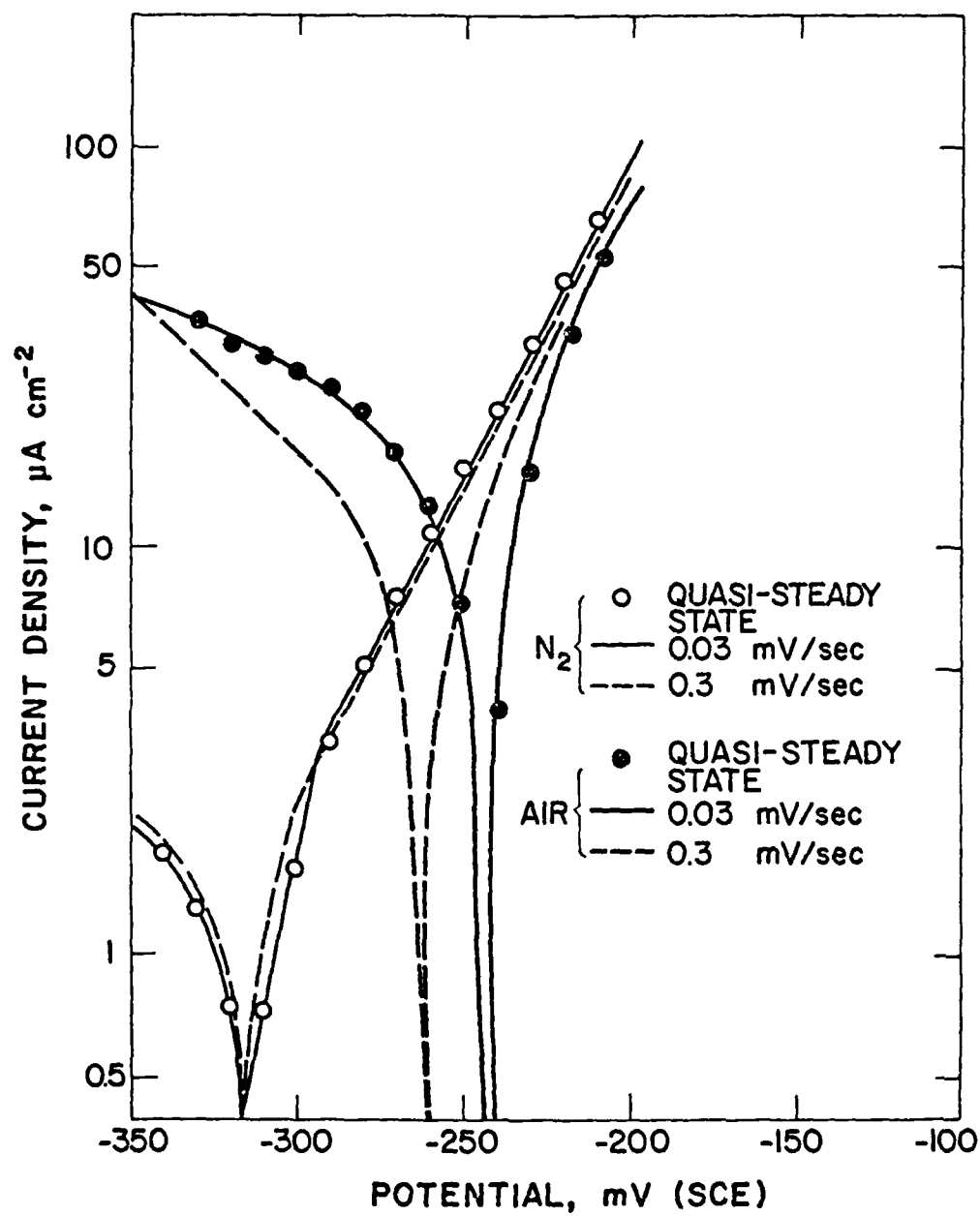
Another set of experiments was conducted to study the roles of the outer and inner parts of the adherent corrosion product in the corrosion processes. To do that the specimens corroded in the corrosion vessels with and without sulfide contamination were dried overnight in a desiccator and the outer part (which is loosely adherent to the alloy) of the corrosion products was removed with poly-tapes. Then, polarization curve measurements in both aerated and deaerated electrolyte solution were conducted on the adherent inner layer. Furthermore on some specimens Palladium was coated on the inner layer surface. Since Pd is well-known to be a good catalyst, the coating on the specimens

---

\* Potential was shifted manually every 10 mV, and at each potential a quasi-steady state current was observed before changing the potentials.

† Rotation speeds up to 66.7 r.p.s. produce laminar, rather than turbulent, flow for the size of the disc electrode,  $r = 0.5 \text{ cm}$ .

Figure 7. Effect of potential scanning rate on polarization curves.



would promote the oxygen reduction reaction. The specimens were coated in the following manner:

- (i) Specimen surface (corroded or fresh) was dried thoroughly.
- (ii) The outer portion of the corrosion products was removed by poly-tapes.
- (iii) A few drops of Pd<sup>\*</sup> was placed on the whole area of the specimen surface.
- (iv) After 5 minutes the excess of the Pd was removed with tissue paper and air.

After application of the palladium the specimen was placed in the electrochemical cell and the polarization curve was measured in de-aerated solution.

### 3.5.2. X-ray Diffraction Analysis

To study the structures of the 5-day corrosion product layers developed on the alloy in clean and sulfide-polluted 3.4 wt. % NaCl solution two methods of the X-ray diffraction analysis were conducted. The flaky part (outer layers) of the corrosion products were stripped with double-phase tape and placed onto a slide-glass. Then, the products on the glass slide were analyzed with an X-ray diffractometer. Another method involved scraping off the total corrosion products (including the adherent inner layer) with a knife and analyzing the resultant corrosion product powder with the Debye-Scherrer X-ray diffraction method.

---

\* Pallamarse, 37.75 g/l, Technic Inc., Chicago, Ill.



### 3.5.3. ESCA Study of the Corrosion Products

The ESCA (Electron Spectroscopy for Chemical Analysis) examination was conducted at the University of Surrey in the laboratory of Dr. J. Castle by ESCA 3, type 2, V. G. Scientific Ltd. The disc samples were cut from the plexiglass sample holder and mounted in batches of five on the probe of the spectrometer and examined with Al K $\alpha$  radiation. The heights and areas of the principal peaks of the elements Cl, C, S, O, Cu, and Ni were obtained using a computer-based data acquisition system.\* In addition, survey scans covering the binding energy range 0-1000 eV were taken from each sample. Individual peaks could be obtained to an accuracy of  $\pm 0.2$  eV from the computer display. Analyses in all cases were corrected, using relative sensitivity factors based on those published by Jorgenson and Berthou (45) and normalized to 100 atom percent excluding carbon which in most cases was merely present as a surface contaminant.

ESCA studies were conducted on the following samples:

- A. 3-day corroded, clean.
- B. 3-day corroded, sulfide-contaminated.
- C. 5-day corroded, sulfide-contaminated.

For each sample the studies were conducted on the top surface of the corrosion product, followed by removal of the outer portion of the corrosion product with adhesive tape and analyses on the fractured material remaining on the metal substrate and that adhering to the tape.

---

\* V. G. DataSystems Limited, England.

Three different time periods, 0, 15, and 60 seconds of ion sputtering (Ar ion operating at 10  $\mu$ A, 5 keV), were utilized on each analysis to study the concentration gradients of the elements.

#### 3.5.4. SEM Study of the Corrosion Products

SEM (Scanning Electron Microscope) investigation was conducted on the 5-day clean and sulfide corrosion product layers. Photomicrographs were taken on the surfaces of the outer layer of corrosion products and the inner layer after stripping the outer layer with polytapes. For cross-sectional investigation of the corrosion product layers the samples were prepared by bonding the corroded surface to a clean metal surface (supporting metal) with EPOXY (Conap, Inc., Olean, N.Y.), securing the corrosion products between the alloy and the supporting metal. Then, the sample in this form was mounted in Koldmount and polished. On some samples X-ray fluorescence chemical analysis was conducted on the SEM samples, and the presence of elements, such as Cu, Ni, Fe, Cl, and S, was determined at different layers throughout the thickness of the corrosion product.

## 4. RESULTS

### 4.1. X-ray Examination of the Corrosion Product Layers

The corrosion product layers developed during the 5-day clean corrosion showed a dull tan color. The outer part of the corrosion products stripped with poly-tape was green and the adherent inner layer surface was dull reddish brown. The X-ray powder diffraction analysis on the total corrosion products (powder obtained from the entire corrosion product) showed mainly  $\text{Cu}_2(\text{OH})_3\text{Cl}$  and much less  $\text{Cu}_2\text{O}$ . The outer part of the corrosion products which was stripped with double-phase tape was identified as  $\text{Cu}_2(\text{OH})_3\text{Cl}$  by the X-ray diffractometer. The measured d-spacings are compared with tabulated d-spacings in Table 4.

The corrosion product layers developed during the 5-day sulfide corrosion had a black outer layer and a dull reddish brown inner layer. The X-ray analyses conducted on the corrosion products of the outer part and the total parts show  $\text{Cu}_2\text{S}$  and  $\text{Cu}_2(\text{OH})_3\text{Cl}$  (Table 5). The presence of  $\text{Cu}_2\text{O}$  is not clear, since  $\text{Cu}_2\text{O}$  peaks are overlapped by the  $\text{Cu}_2\text{S}$  and  $\text{Cu}_2(\text{OH})_3\text{Cl}$  peaks. There are some peaks which appeared in the outer part of the corrosion products and did not appear in the total products. These peaks are very small and are hard to distinguish from the background noise.

Table 4

X-ray Diffraction Analysis of the Total and Outer  
Part of the Corrosion Products Developed During  
the 5-day Clean Corrosion Run

Compound	d-Spacings (nm) on File*	Measured d-Spacing (nm)**	
		Total	Outer
$\text{Cu}_2(\text{OH})_3\text{Cl}$	0.548	0.545	0.545
$\text{Cu}_2(\text{OH})_3\text{Cl}$	0.470	0.472	
$\text{Cu}_2(\text{OH})_3\text{Cl}$	0.455	0.455	
$\text{Cu}_2(\text{OH})_3\text{Cl}$	0.341	0.344	0.342
$\text{Cu}_2\text{O}$	0.302	0.301	
$\text{Cu}_2(\text{OH})_3\text{Cl}$	0.290	0.289	0.289
$\text{Cu}_2(\text{OH})_3\text{Cl}$	0.275	0.276	0.275
$\text{Cu}_2\text{O}$	0.247	0.248	
$\text{Cu}_2(\text{OH})_3\text{Cl}$	0.233	0.234	0.233
$\text{Cu}_2(\text{OH})_3\text{Cl}$	0.226	0.227	0.227
Cu-Ni	0.209 <sup>+</sup>	0.207	
Cu-Ni	0.194 <sup>+</sup>	0.198	
Cu-Ni & $\text{Cu}_2(\text{OH})_3\text{Cl}$	1.82 <sup>+</sup>	0.179	
$\text{Cu}_2(\text{OH})_3\text{Cl}$	1.170	0.172	0.171
$\text{Cu}_2\text{O}$ & $\text{Cu}_2(\text{OH})_3\text{Cl}$	0.151	0.151	

\* Joint Committee for Powder Diffraction File (JCPDE).

\*\* These were the only peaks that were observed.

<sup>+</sup> The average d-spacings of Cu-9.4Ni-1.7Fe.

Table 5

X-Ray Diffraction Analysis of the Total and Outer Part  
of the Corrosion Products Developed During the 5-day  
Sulfide Corrosion Run

Compound	d-Spacings (nm) on File*	Measured d-Spacing (nm)**	
		Total	Outer
$\text{Cu}_2(\text{OH})_3\text{Cl}$	0.548	0.550	0.547
$\text{Cu}_2(\text{OH})_3\text{Cl}$	0.469	0.467	
$\text{Cu}_2\text{S}$	0.340		0.339
$\text{Cu}_2\text{O}$	0.302	0.302	
$\text{Cu}_2\text{S}$	0.301	0.302	
$\text{Cu}_2(\text{OH})_3\text{Cl}$	0.298	0.299	
$\text{Cu}_2(\text{OH})_3\text{Cl}$	0.290	0.290	0.289
$\text{Cu}_2(\text{OH})_3\text{Cl}$	0.288	0.290	0.289
$\text{Cu}_2(\text{OH})_3\text{Cl}$	0.281	0.281	
$\text{Cu}_2\text{S}$	0.276	0.275	0.276
$\text{Cu}_2(\text{OH})_3\text{Cl}$	0.276	0.275	0.276
$\text{Cu}_2\text{S}$	0.272	0.271	
$\text{Cu}_2(\text{OH})_3\text{Cl}$	0.271	0.271	
$\text{Cu}_2\text{O}$	0.274	0.246	0.247
$\text{Cu}_2\text{S}$	0.247	0.246	0.247
$\text{Cu}_2(\text{OH})_3\text{Cl}$	0.228	0.229	
$\text{Cu}_2(\text{OH})_3\text{Cl}$	0.226	0.225	0.226
$\text{Cu}_2\text{S}$	0.224	0.225	0.226
$\text{Cu}_2\text{O}$	0.214	0.213	0.213
$\text{Cu}_2\text{S}$	0.214	0.213	0.213
$\text{Cu-Ni}$	0.209 <sup>+</sup>	0.209	
$\text{Cu}_2\text{S}$	0.197	0.199	

\* Joint Committee for Powder Diffraction File (JCPDE).

\*\* These were the only peaks that were observed.

<sup>+</sup> The average d-spacings of Cu-9.4Ni-1.7Fe.

Table 5 (Continued)

Compound	d-Spacings (nm) on File*	Measured d-Spacing (nm)**	
		Total	Outer
$\text{Cu}_2\text{S}$	0.197	0.199	0.196
$\text{Cu}_2(\text{OH})_3\text{Cl}$	0.196	0.199	0.196
$\text{Cu}_2\text{S}$	0.188		0.188
$\text{Cu}_2\text{S}$	0.187		0.187
$\text{Cu}_2\text{S}$	0.180	0.179	
$\text{Cu}_2(\text{OH})_3\text{Cl}$	0.179	0.179	
$\text{Cu}_2\text{S}$	0.171	0.170	0.171
$\text{Cu}_2(\text{OH})_3\text{Cl}$	0.171	0.170	0.171
$\text{Cu}_2\text{S}$	0.151	0.151	0.150
$\text{Cu}_2\text{O}$	0.151	0.151	0.150
$\text{Cu}_2(\text{OH})_3\text{Cl}$	0.151	0.151	0.150

#### 4.2. ESCA Examination of the Corrosion Product Layers

The results obtained by the ESCA studies are shown in Table 6. The "sulfide" and "clean" corrosion products have some common features, such that the positions A and C have Cu-to-Ni ratios of 2 to 1 or less, and the position B has a 1 to 1 ratio (refer to sketch in Table 6). In the sulfide corrosion products the peak of S was identified to be sulfide ( $S^{--}$ ), and the amount of  $S^{--}$  decreases from the position of A to C. On the other hand the concentration of chloride increases from A to C.

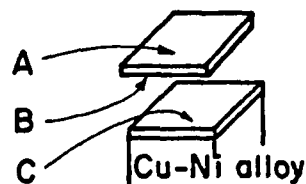
#### 4.3. SEM Examination of the Corrosion Product Layers

SEM examinations of the top surface and the cross-section of the corrosion products developed during a 5-day clean corrosion are shown in Figures 8 and 9, respectively. The cross-section shows two well-defined layers on the top of the Cu-Ni alloy. Another set of SEM examinations was conducted on the cross-section of the corrosion products after stripping the flaky part of the corrosion products. However, the adherent (inner) layer could not be seen due to its small thickness. Thus, metallography (Figure 9) can show the outer porous layer (thickness of 2.5-5  $\mu m$ ) and the relatively dense middle layer (thickness of 5  $\mu m$ ), but not the thin inner layer. The SEM micrographs of the top surface (Figure 8) were taken near the edge of a stripped region, and show the outer porous (Figure 8(a)) and the inner dense surface ringed with the remaining adherent outer layer (Figure 8(b)).

SEM examination of the top surface and the cross-section of the corrosion products developed during the 5-day sulfide corrosion are

Table 6

ESCA Semi-quantitative Analysis of Corrosion Products  
Developed During the 3-day Clean, 3-day Sulfide, and  
5-day Sulfide Corrosion Runs (Relative at. %)



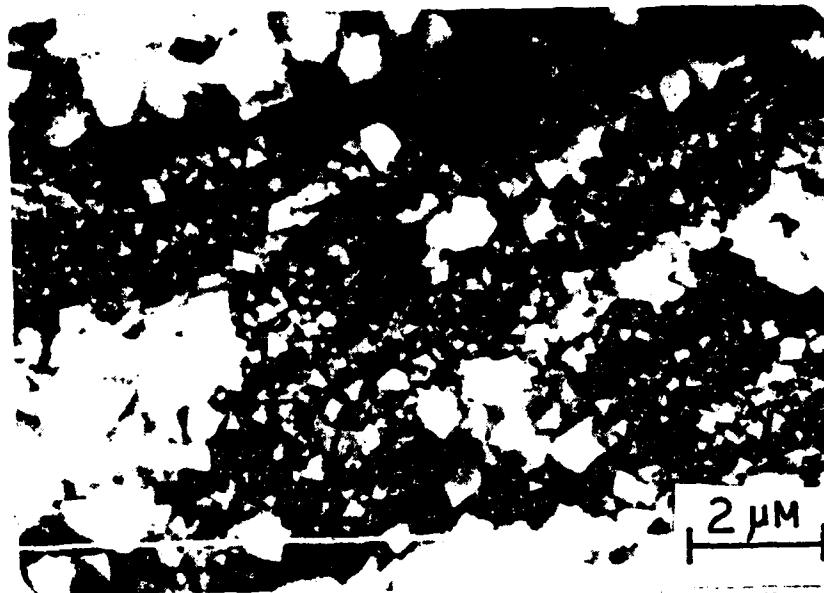
Location		A			B			C		
Sample I.D.	Element	Etching Time Seconds*			Etching Time Seconds*			Etching Time Seconds*		
		0	15	60	0	15	60	0	15	60
3-day clean	Cu	14.2	18.6	31.8	45.6	7.4	55.6	20.3	20.6	26.5
	Ni	N.D.	N.D.	N.D.	55.4	19.1	44.4	10.4	12.8	13.0
	O	62.3	48.5	49.5	**	50.0	**	61.6	56.4	49.2
	Cl	23.5	32.9	18.7	**	20.5	**	7.7	10.3	11.2
3-day sulfide	Cu	**	27.4	34.0	18.3	15.8	11.3	22.7	25.9	29.1
	Ni	**	4.7	2.9	24.0	21.6	11.3	3.8	4.5	5.0
	S	**	6.1	9.9	7.4	5.8	1.5	0.3	0.1	0.4
	O	**	52.0	41.0	42.0	49.4	67.0	55.2	50.5	45.9
	Cl	**	9.8	11.8	8.4	7.4	7.0	18.0	19.0	19.6
5-day sulfide	Cu	13.8	16.1	24.9	13.7	12.8	5.9	16.4	17.8	20.4
	Ni	11.6	6.2	6.9	26.4	21.2	13.2	7.5	9.0	10.7
	S	5.7	5.9	7.9	3.6	2.5	3.6	1.7	2.0	2.4
	O	56.3	55.0	43.4	46.1	51.4	64.1	53.0	45.3	41.0
	Cl	12.7	16.9	16.9	10.1	12.1	13.3	21.5	25.8	25.5

\* Approximate etching speed of 5 nm/min.

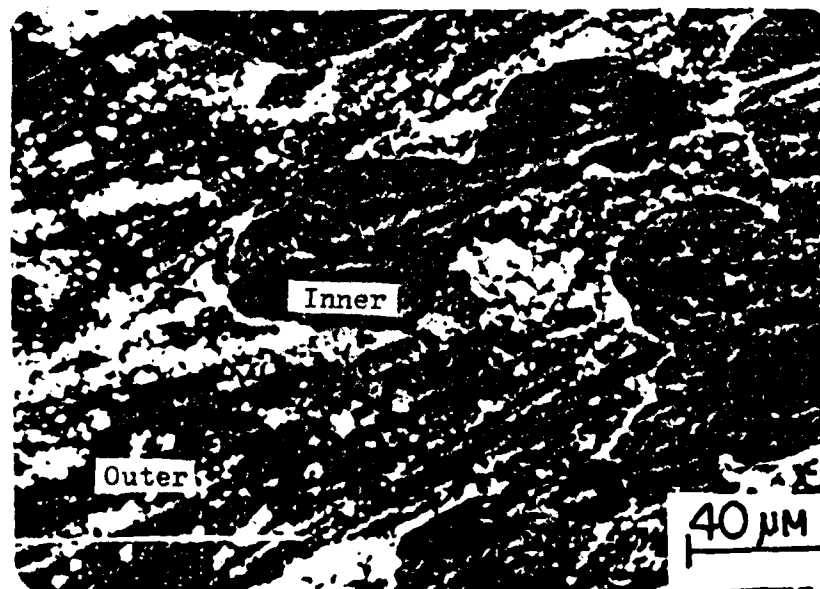
\*\* Data is not available due to experimental failure.

N.D. None detectable.





(a)



(b)

Figure 8. SEM photomicrographs of the top surfaces of the corrosion products after the 5-day clean corrosion: (a) outer surface, (b) outer and inner surfaces.

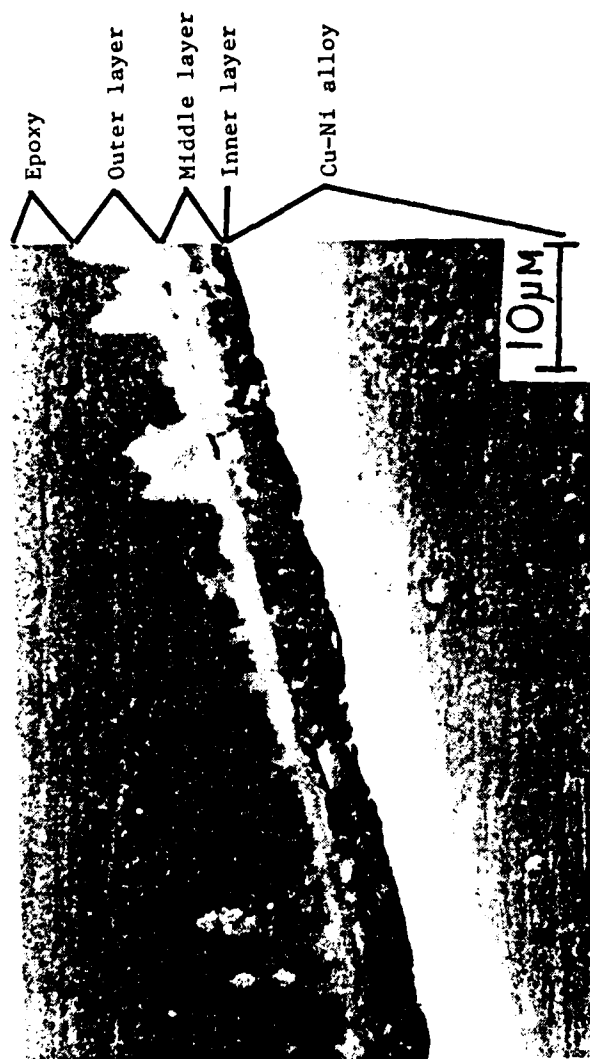
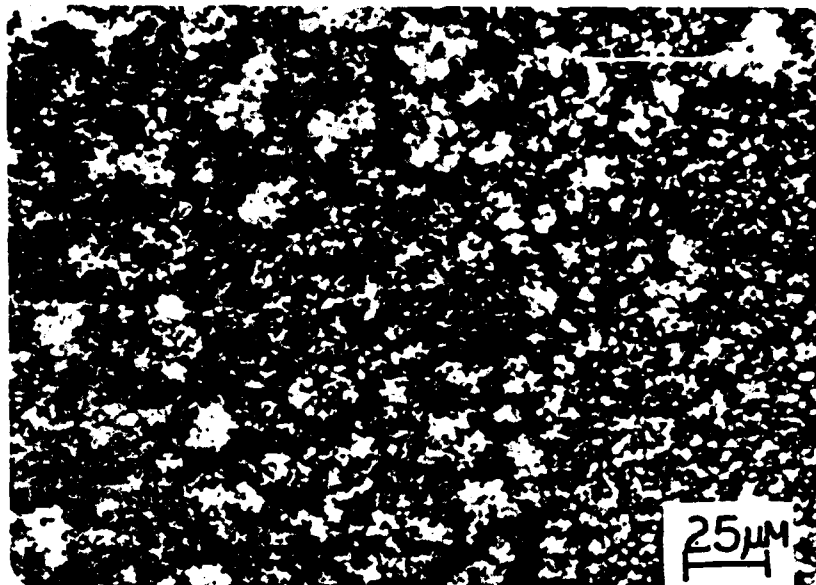
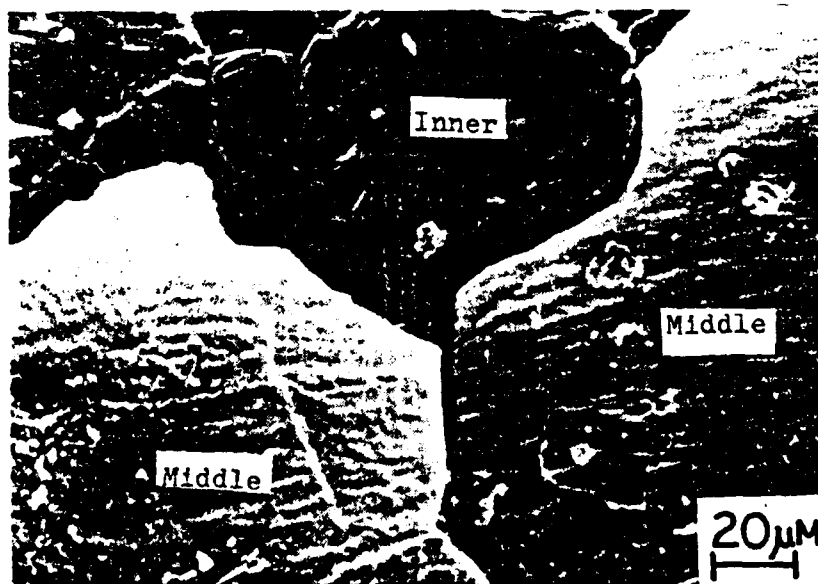


Figure 9. SEM photomicrograph of the cross section of the corrosion products after the 5-day clean corrosion.



(a)



(b)

Figure 10-a. SEM photomicrographs of the top surfaces of the corrosion products after the 5-day sulfide corrosion; (a) outer layer, (b) middle and inner layers.



Figure 10-b. SEM photomicrograph of the top surfaces of the corrosion products after the 10-day sulfide corrosion.

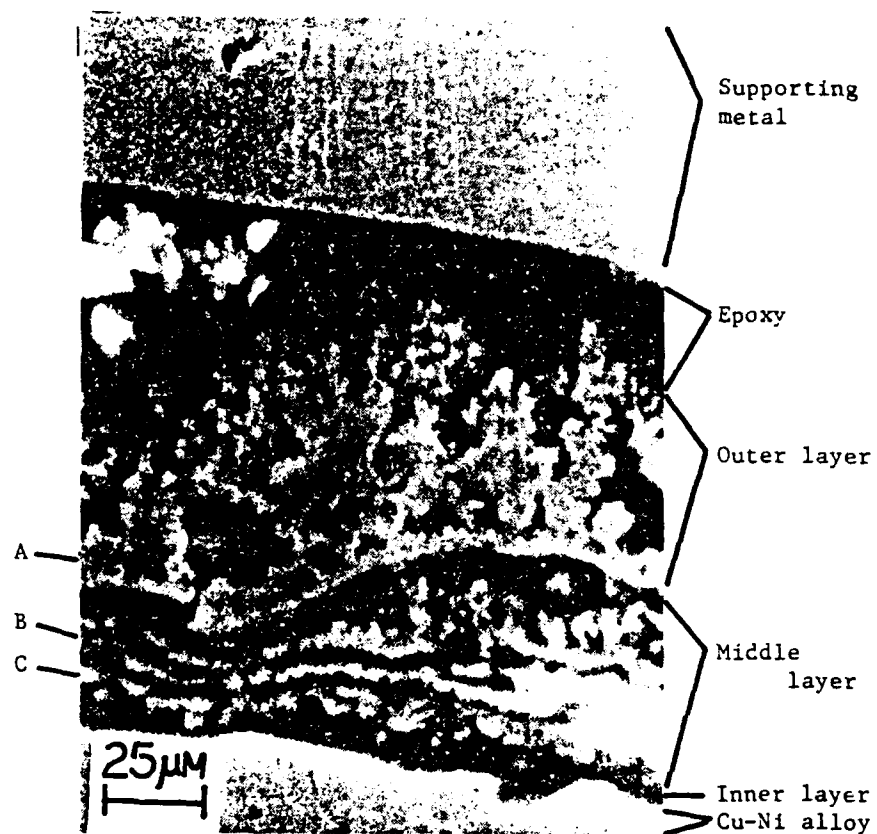


Figure 11. SEM photomicrograph of the cross section of the corrosion products after the 5-day sulfide corrosion (A, B, and C are positions where X-ray fluorescence chemical analyses are made).

shown in Figures 10 and 11, respectively. The corrosion products developed during the sulfide corrosion are relatively thick.\* As such the X-ray fluorescence chemical analysis was readily utilized to characterize the various layers of the corrosion products. The chemical spectra obtained at the positions of A, B, and C in the cross-section of the corrosion products (Figure 11) are shown in Figure 12. The cross-section of the corrosion product (Figure 11) shows several well-defined layers. However, similar to the corrosion product developed during the clean corrosion (Figure 9), the thin inner layer (adherent part of the corrosion products) is not seen in Figure 11. Thus, the cross-section shows only the flaky part of the corrosion products, and they are: (A) the outer layer rich in Cu and S, probably  $\text{Cu}_2\text{S}$ ; (B) the middle layer rich in Cu and Cl and containing a small amount of Fe, Ni, and S, probably  $\text{Cu}_2(\text{OH})_3\text{Cl}$ ; (C) the inner middle layer rich in Cu, Ni, and Fe, probably  $\text{Cu}_2\text{O}$ . The SEM micrographs on the top of the corrosion products show the very porous outer layer and relatively dense and smooth surface of the middle and inner layer (Figure 10-a). The micrograph (Figure 10-b) was taken along the boundary of the inner (after stripping) and the outer layers of a 10-day sulfide sample, and clearly shows the edge of the outer layer and the small piece of the exposed middle layer underlying the outer layer.

#### 4.4. Polarization Curve Measurements

##### 4.4.1. Corrosion Current and Potential Determinations

Polarization curves produced on fresh surfaces at a rotation speed of 8.3 r.p.s. are shown in Figure 13. The curves labelled B and B' were measured in the deaerated solution and the

---

\*The corrosion products developed during the clean corrosion are too thin for the X-ray fluorescence analysis.

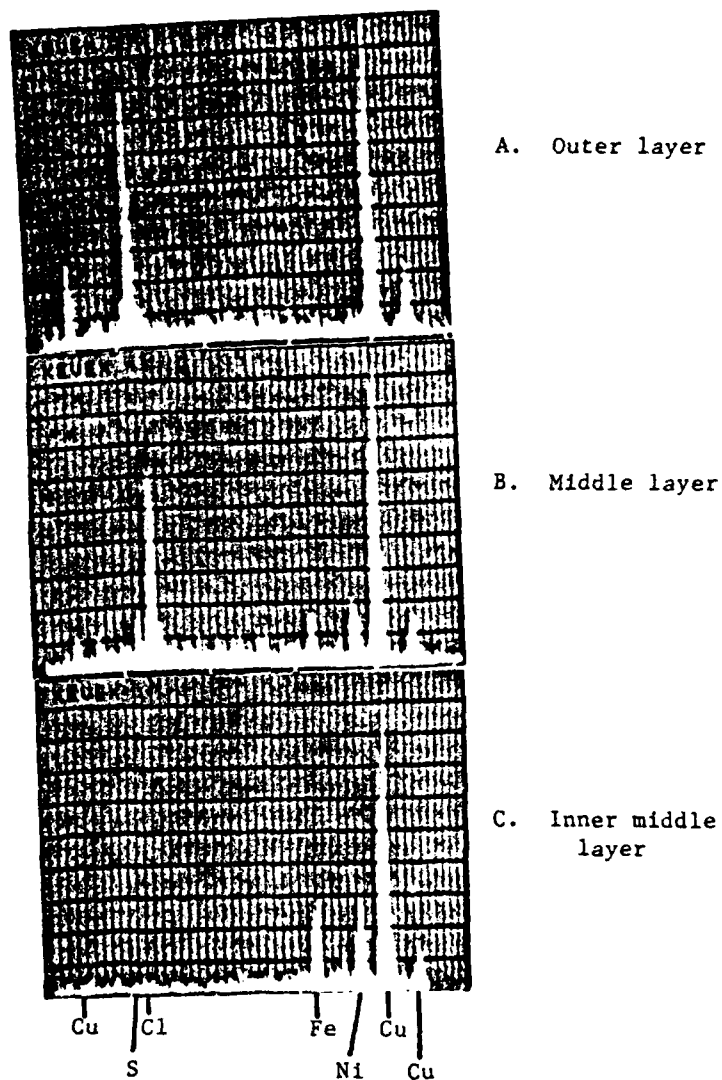


Figure 12. X-ray fluorescence chemical analyses of various portions (A, B, and C in Figure 11) of the corrosion products after 5-day sulfide corrosion.

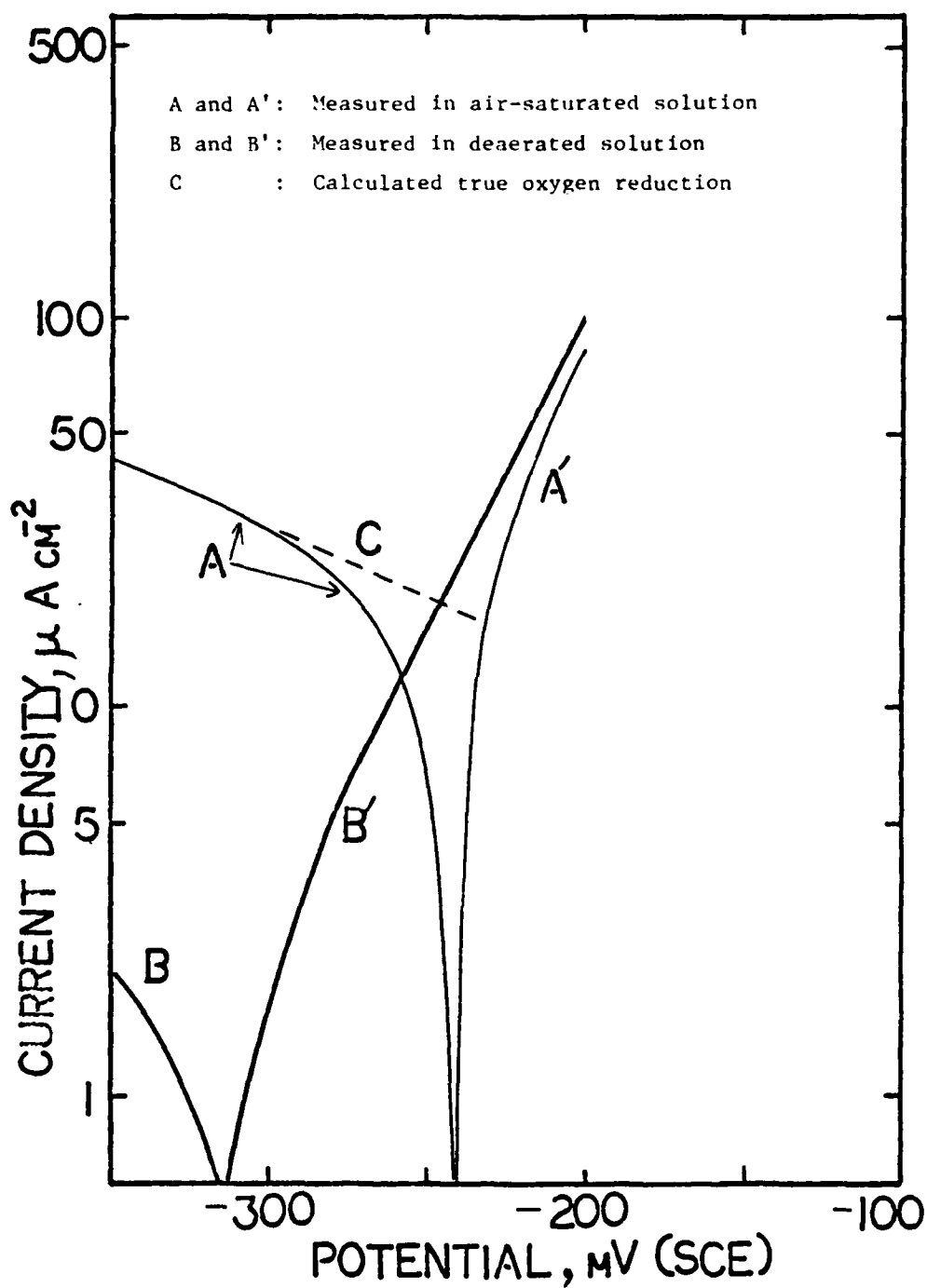


Figure 13. Polarization curves on the fresh surfaces at rotation speed of 8.33 r.p.s.



current was produced by reduction of impurities\* (curve B) and anodic metal dissolution (curve B'). The curves A and A' were measured in aerated solution and produced by a mixture of oxygen reduction and metal dissolution. Addition of curve B' to the curve A gives the dotted line, curve C, in the potential range -310 mV to -250 mV (SCE). Subtraction of curve A' from B' gives an extension of curve C at potentials above -240 mV (SCE). Curve C represents the "true oxygen reduction" kinetics. The intersection of curves B' and C, where the metal dissolution rate equals the true oxygen reduction rate, is the corrosion current ( $18 \mu\text{A}/\text{cm}^2$ ) and the corrosion potential (-245 mV).

Similarly, corrosion currents and potentials are determined on the corroded surface. However, during the polarization measurements on the corroded sample a part of the current produced can be due to reduction of the corrosion products in addition to oxygen reduction. To measure the amount of reduction of the corrosion products, the corroded samples were held at a constant potential of -350 mV (SCE) in the deaerated solution and the current was measured (Figure 5). The quasi-steady state on the 5-day clean corroded sample is  $0.9 \mu\text{A}/\text{cm}^2$  cathodic, which is lower than the current on the fresh surface ( $1.5 \mu\text{A}/\text{cm}^2$  cathodic), indicating no substantial reduction of the corrosion products, and that the impurity reduction rate is slower on

---

\* Around this potential region there is no species to be reduced except  $10^{-6} \text{ mol}/\text{cm}^3$  (46) of impurities ( $\text{H}_2$  evolution occurs  $< -700 \text{ mV}$  (SCE) at pH 7). A typical current density produced by the reduction of impurities in deaerated double distilled water is about  $4 \mu\text{A}/\text{cm}^2$  with a rotating disc electrode (46).

the corroded surface than on the fresh surface. On the other hand the quasi-steady state current produced on the sulfide corroded sample in deaerated solution is much higher ( $10 \mu\text{A}/\text{cm}^2$  cathodic) and continuously decreases with time. This shows that the current produced by the reduction of the sulfide corrosion products can be about  $10 \mu\text{A}/\text{cm}^2$  during the polarization measurements (for  $7.2 \times 10^3$  seconds). Nevertheless, this current is much lower than the (oxygen) reduction current produced in aerated solution ( $650 \mu\text{A}/\text{cm}^2$ , in Figure 6), so that it is reasonable to ignore the current due to the reduction of the corrosion products.

In the following text, anodic metal dissolution and cathodic true oxygen reduction are presented, and the reduction of the corrosion products is ignored.

#### 4.4.2. Polarization Curves on Fresh Surface

The anodic metal-dissolution polarization curves are shown in Figure 14. The current density increases with potential, ranging from  $-310 \text{ mV (SCE)}$  to  $-200 \text{ mV (SCE)}$ . Above the potential  $-280 \text{ mV (SCE)}$  a distinct Tafel line (exponential relation of the current density vs. potential) is observed. The polarization curve is shifted by the rotation speed (8.31, 20.0, 31.7 r.p.s.), being less polarized at a higher rotation speed, while the Tafel slope is constant (60-62 mV/decade). A plot of current density vs. square root of the rotation speed at constant potential (Figure 15) shows a linear relation, and an extrapolation of this linear region goes through the origin.

The cathodic oxygen reduction polarization curves are also shown in Figure 14. The current density decreases with increasing potential

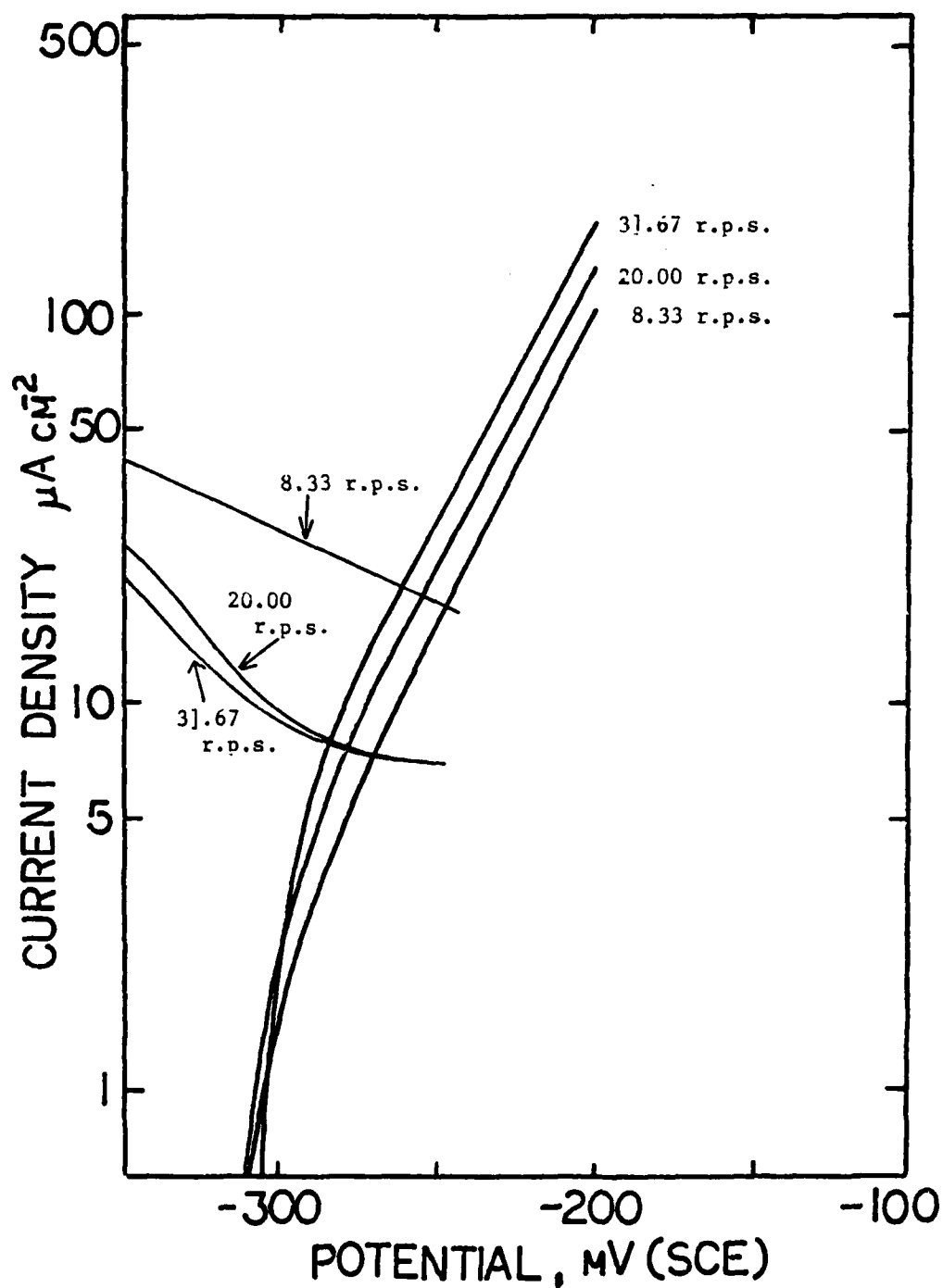


Figure 14. Rotation speed dependence of the polarization curves on the fresh surface.

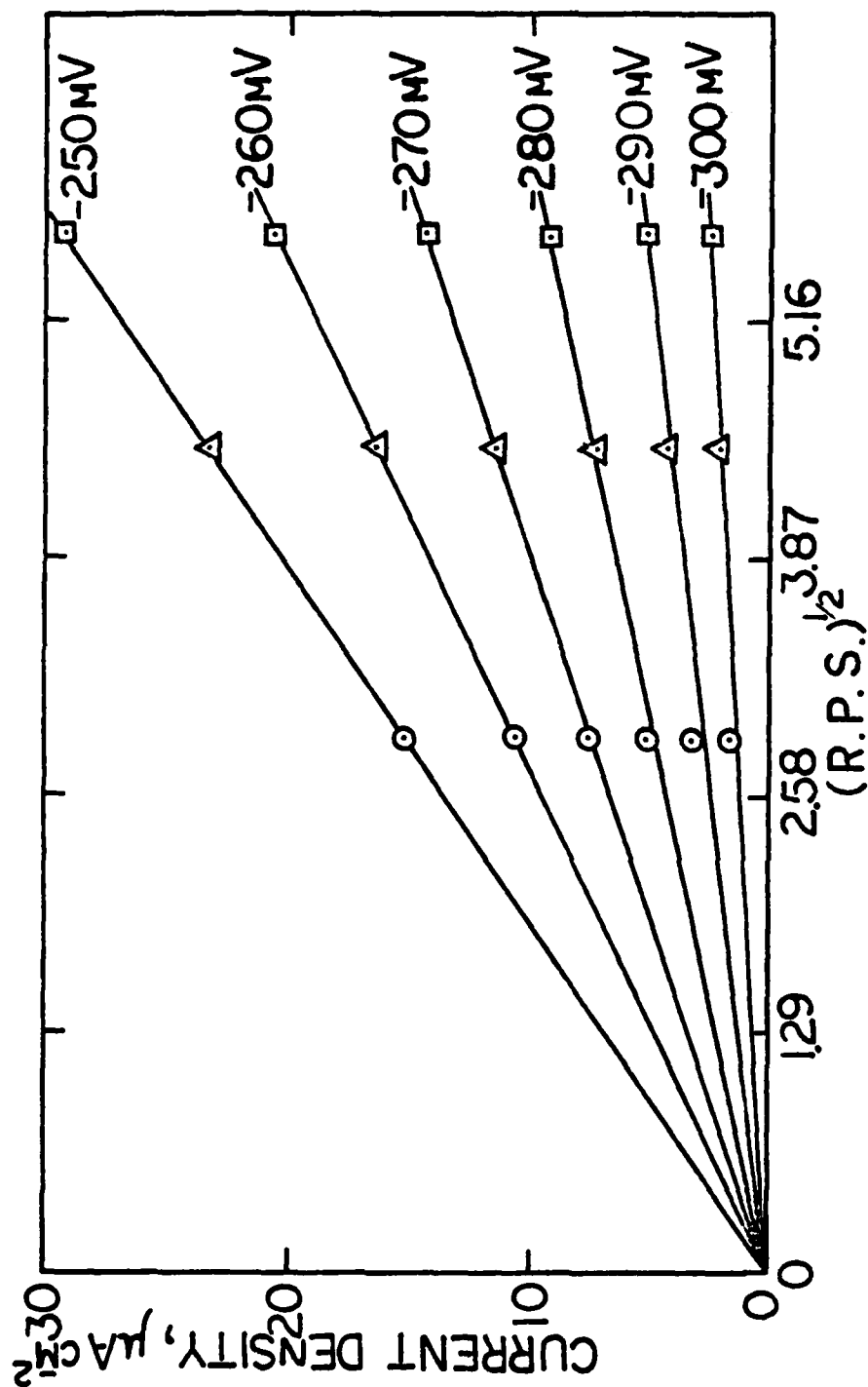


Figure 15. Anodic current density vs. square root of the rotation speeds on the fresh surface, in deaerated solution.

from -300 mV (SCE) to -200 mV (SCE), and also is dependent of the rotation speed. However, the current density decreases with increasing rotation speed, which is unlikely to occur if the rate-controlling process is a transport of reactants or products in the aqueous phase.

#### 4.4.3. Polarization Curves Measured After Various Periods of Clean Corrosion

It was found that both the anodic metal dissolution rate and cathodic oxygen reduction rate are reduced by the pre-corrosion period, i.e., corrosion products produced during the clean corrosion reduce the anodic and cathodic reaction rates and, hence, the corrosion rates (Figure 16). Near the corrosion potentials of various samples the anodic curves always exhibit the Tafel behavior (linear relation of log current density vs. potential) and their slopes are about 60 mV/decade. It was also found that both anodic and cathodic currents obtained by the R.D.E. after clean corrosion are independent of the rotating speed, even near the corrosion potential.

The corrosion rates (current) obtained from Figure 16 are plotted against the pre-corrosion period (Figure 17). The initial higher rate of corrosion decreases quickly with time. An average weight loss per time ( $\mu\text{g}/\text{cm}^2\text{-hour}$ ) can be obtained from the corrosion current with the use of Faraday's law\*, and is shown in the vertical axis of Figure 18. This rate of weight loss is again converted to total weight loss ( $\mu\text{g}/\text{cm}^2$ ) by integrating the area under the

---

\* Assuming the reaction  $\text{Cu} \rightarrow \text{Cu}^{++} + 2\text{e}^-$ .

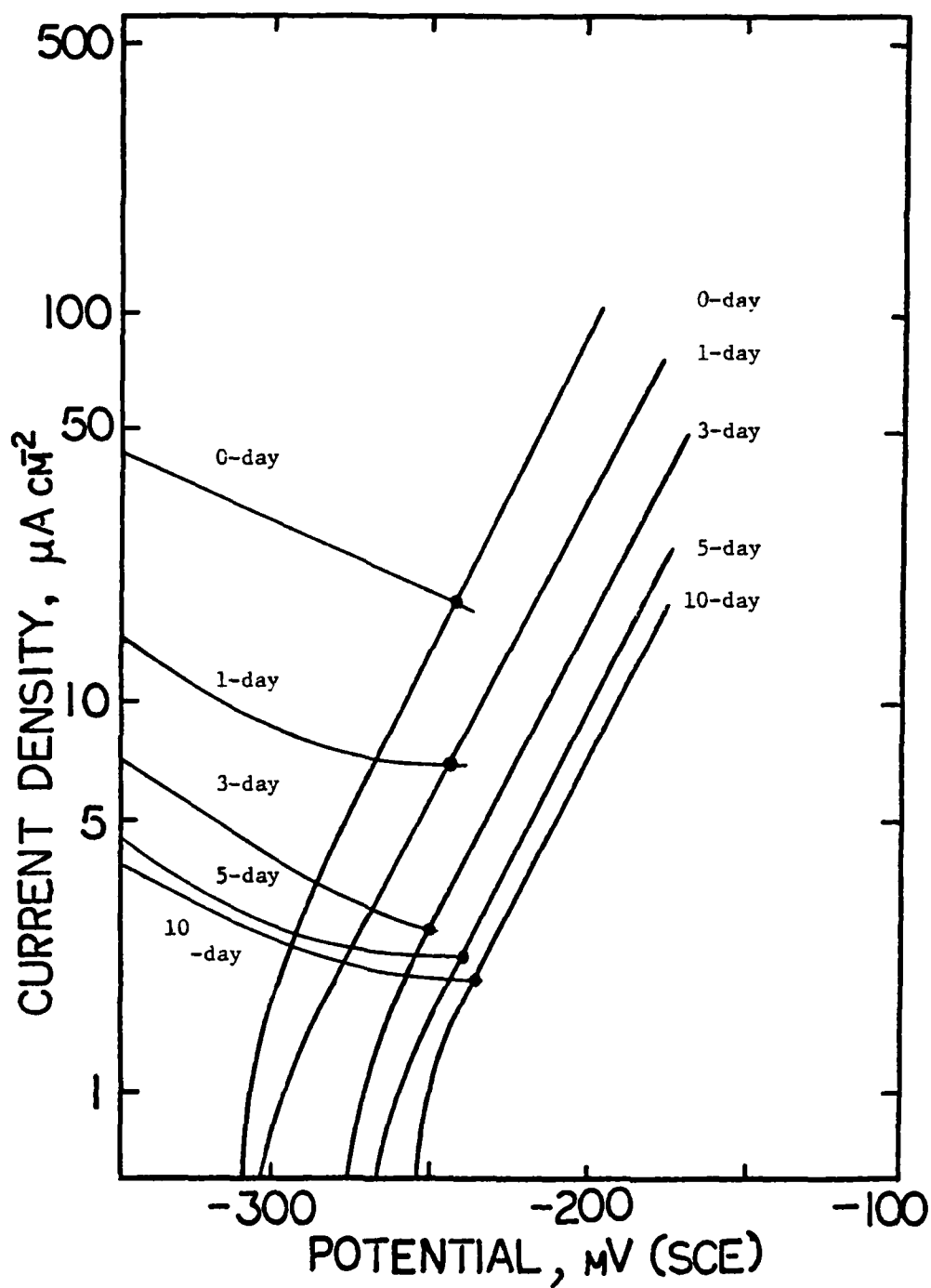


Figure 16. Polarization curves measured after various periods of the clean corrosion.

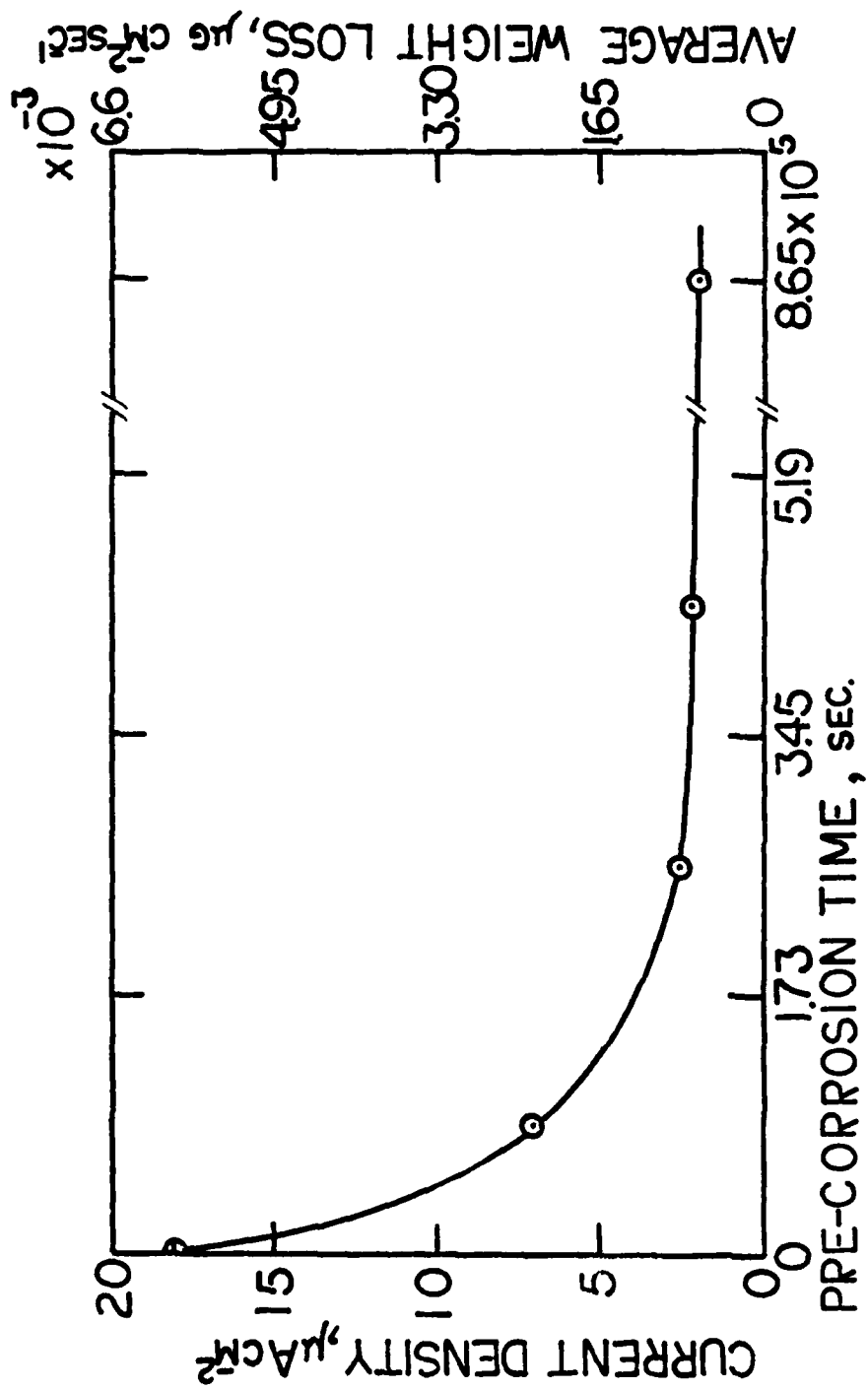


Figure 17. Corrosion current (average weight loss) as a function of the duration of pre-corrosion of the Cu-Ni alloy in 3.4 wt. % NaCl.

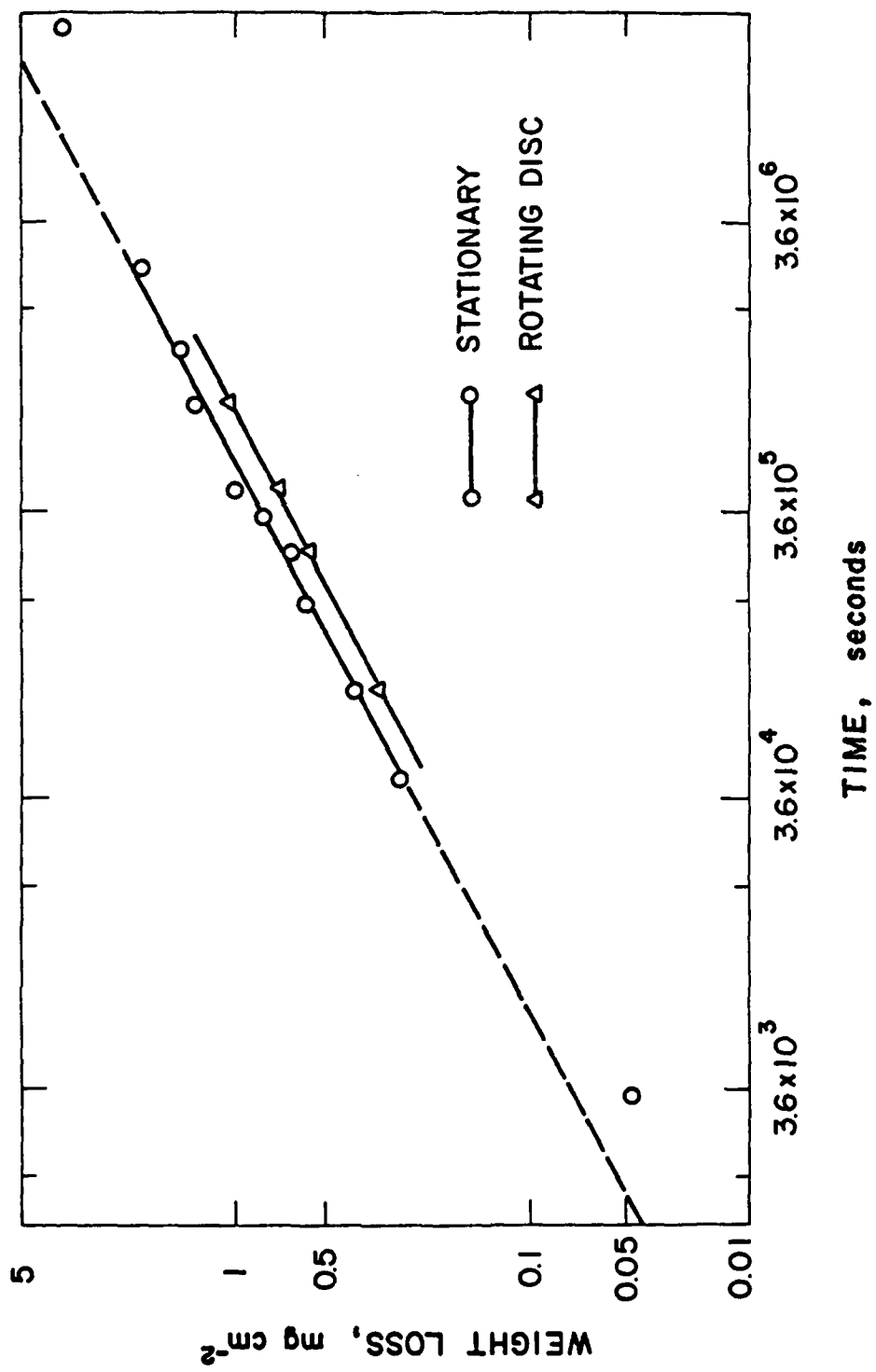


Figure 18. Time variation of weight loss at open circuit potential for the Cu-Ni alloy stationary electrode (29) and the rotating disc electrode.



curve<sup>†</sup> of Figure 17. Then, finally the weight loss ( $\mu\text{g}/\text{cm}^2$ ) is plotted vs. the corrosion time on a log-log scale (Figure 18), and compared with the results obtained with the stationary electrode (29).

The corrosion product developed on the rotating disc electrode after the 5-day clean corrosion can be separated into outer and inner layers by stripping the outer layer with poly-tape. The polarization curves produced on the inner layer are shown in Figure 19-a. Stripping of the outer layer causes an increase in reaction rate (curves B and B' in Figure 19-a) which lie close to the curves made on the fresh surface (curves C and C'), with keeping the Tafel slope of 60 mV/decade. A further increased cathodic current (curve D) can be produced by the Pd coating on the inner layer of the 5-day clean sample.

Among those polarization curves shown in Figure 19-a, the anodic curve B (on the inner layer) and the cathodic curve of D (on the Pd-coated inner layer) are rotation speed dependent, and the curves produced at 8.33 and 20.0 r.p.s. are compared and shown in Figure 19-b. The anodic curve C (on fresh surface) is also dependent on the rotation speed and is described in Figure 14.

#### 4.4.4. Polarization Curves Measured After Various Periods of Sulfide Corrosion

Polarization curves were measured after the 3, 5, and 10 day sulfide corrosion. Figure 20 shows the results, and on the same figure the curve of the 5-day clean is plotted for comparison. Table 7

---

<sup>†</sup>Integration was conducted by weighing the graph paper cut along the curve of Figure 17, knowing the weight of unit area of the paper.

Figure 19-a. Effect of the adherent (inner) layer and the detachable (outer) layer of the corrosion products after the 5-day clean corrosion on the polarization curves (A and A' for 5-day clean, B and B' for stripped 5-day clean, C and C' for fresh surface, and D for Pd-coated stripped 5-day clean).

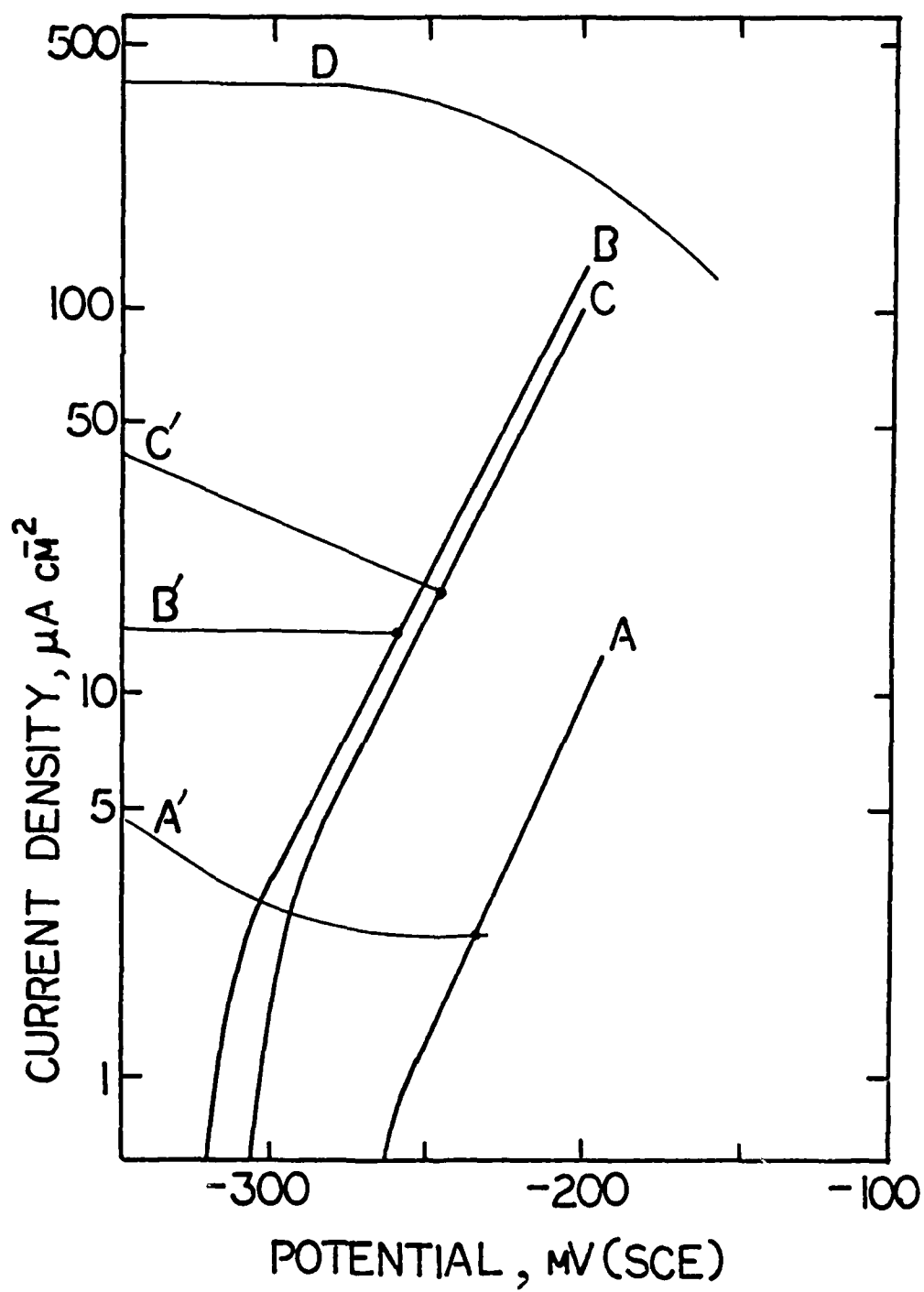
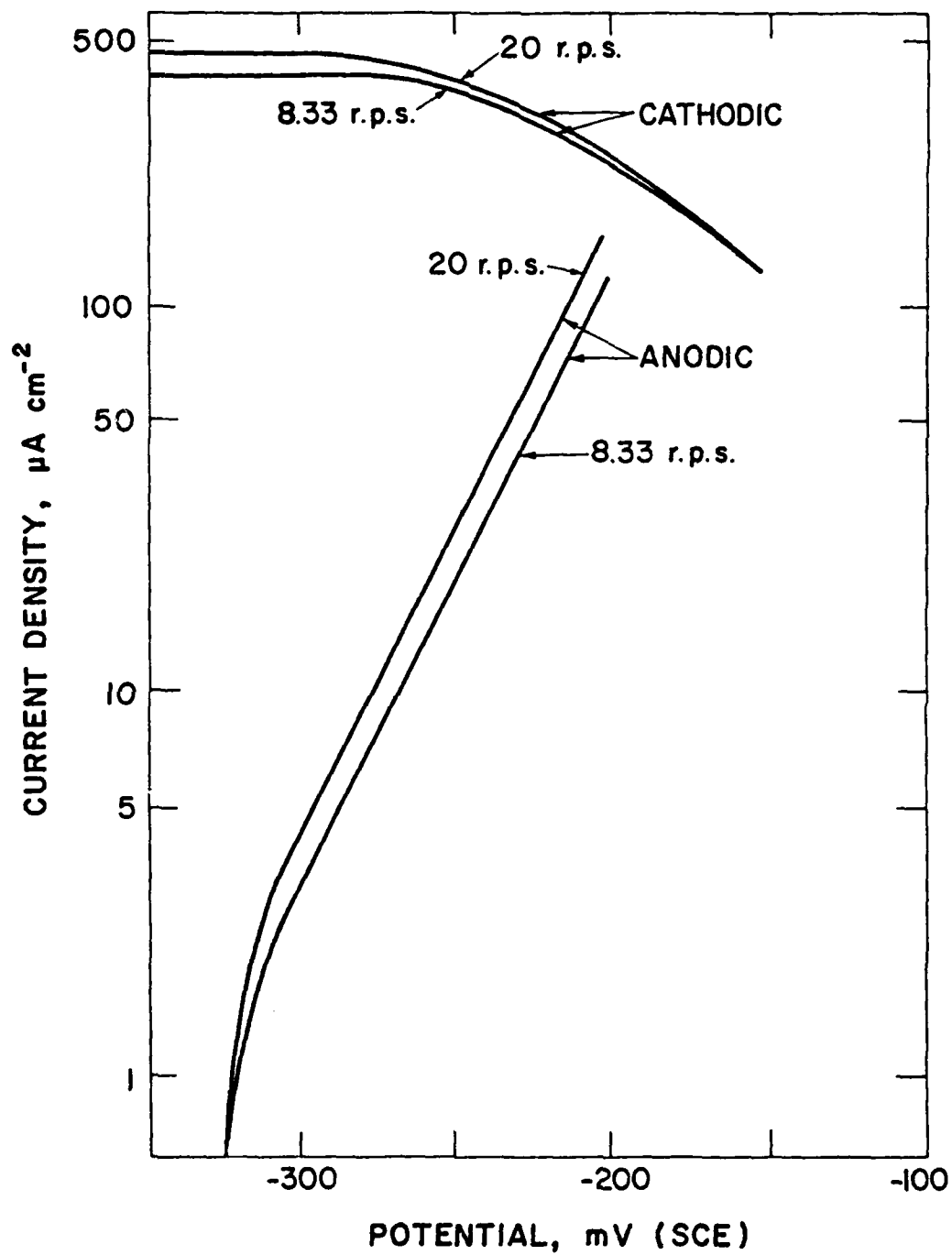


Figure 19-b. Rotation speed dependence of the anodic polarization curves measured on the inner layer of the 5-day clean corrosion and of the cathodic curves measured on Pd-coated inner layer of the 5-day clean corrosion.



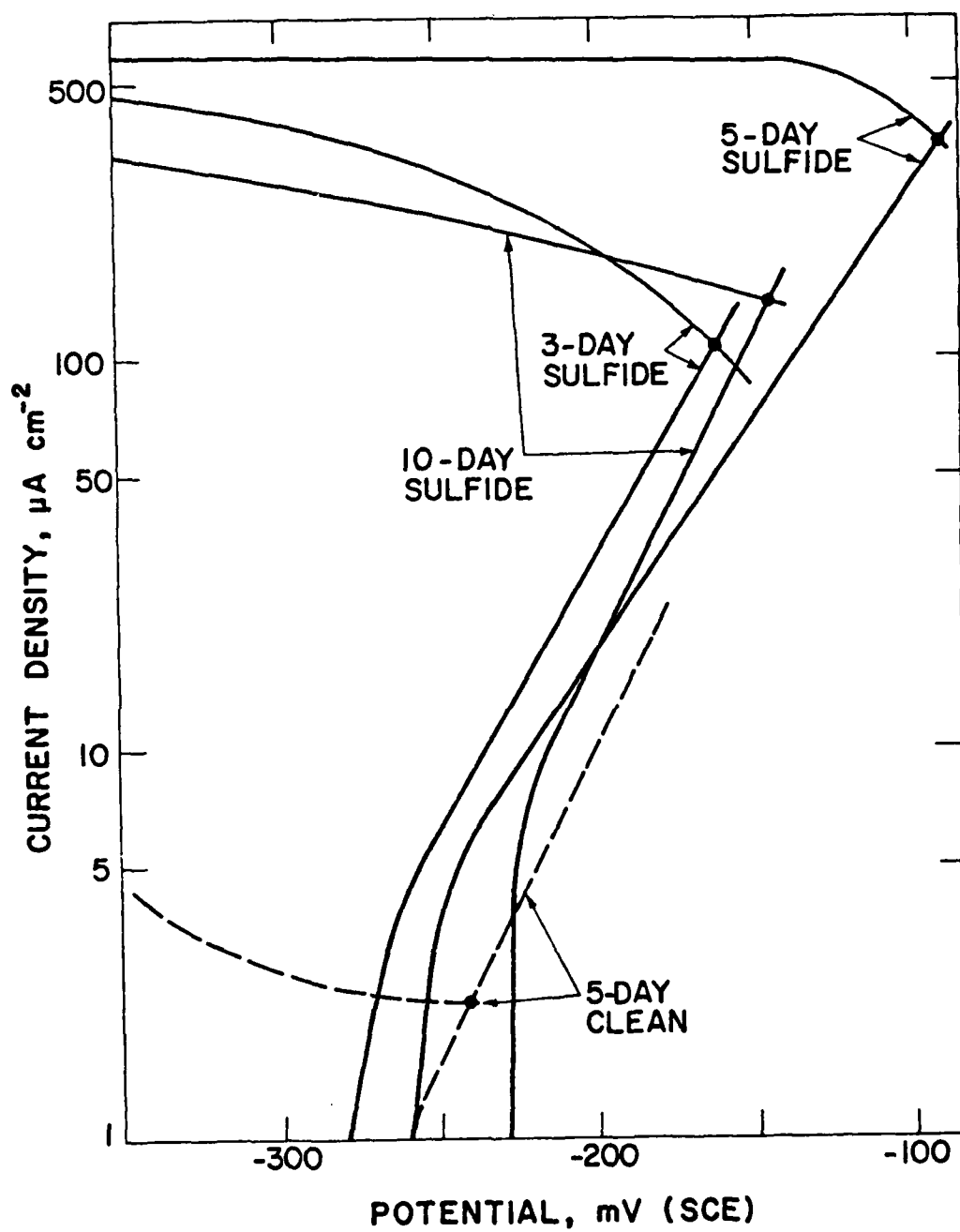


Figure 20. Polarization curves measured on the corrosion products after various periods of the sulfide corrosion.

Table 7  
Corrosion Currents and Potentials During the  
Clean and Sulfide Corrosion

	Sulfide		Clean	
	Potential* (mV)	Current ( $\mu$ A)	Potential* (mV)	Current ( $\mu$ A)
1 Hour	---	---	-245	18.0
1 Day	---	---	-245	7.0
3 Day	-160	120	-255	2.5
5 Day	- 60	400	-240	2.2
10 Day	-150	120	-240	2.0

\* Measured against SCE.

shows values of corrosion currents and potentials obtained from the polarization curves measured on the various clean and sulfide samples. These curves show that the addition of sulfide increases the corrosion current from 2.2  $\mu$ A after 5-day corrosion (in the absence of sulfide) to 400  $\mu$ A, and the sulfide shifts the corrosion potential to a more positive value (from -240 mV to -60 mV (SCE)). The anodic polarization curve is the same as that for corrosion in clean solution, however, the cathodic curve is shifted to currents which are about 100 times greater in the presence of sulfide.

From the obtained corrosion current, determination of the weight loss of the Cu-Ni alloy during the sulfide corrosion was attempted. However, the corrosion currents obtained on the sample corroded for more than 5 days are not reproducible, varying between 100-500  $\mu$ A/cm<sup>2</sup>;

thus the attempt was unsuccessful. This lack of reproducibility is probably due to detachment of corrosion products during the polarization measurements; some flakes of the corrosion product were found at the bottom of the cell.

The polarization curves were measured after stripping the outer flaky part of the corrosion products, Figure 21. The cathodic curve for the sulfide corrosion on the inner layer is more polarized than the curve produced on the outer layer, and is at almost the same position as the cathodic curve produced on the inner layer of the 5-day clean corroded sample. The anodic curve is shifted in the less noble direction and shows exactly the same behavior as the anodic curve produced on the inner layer of the 5-day clean corroded sample.



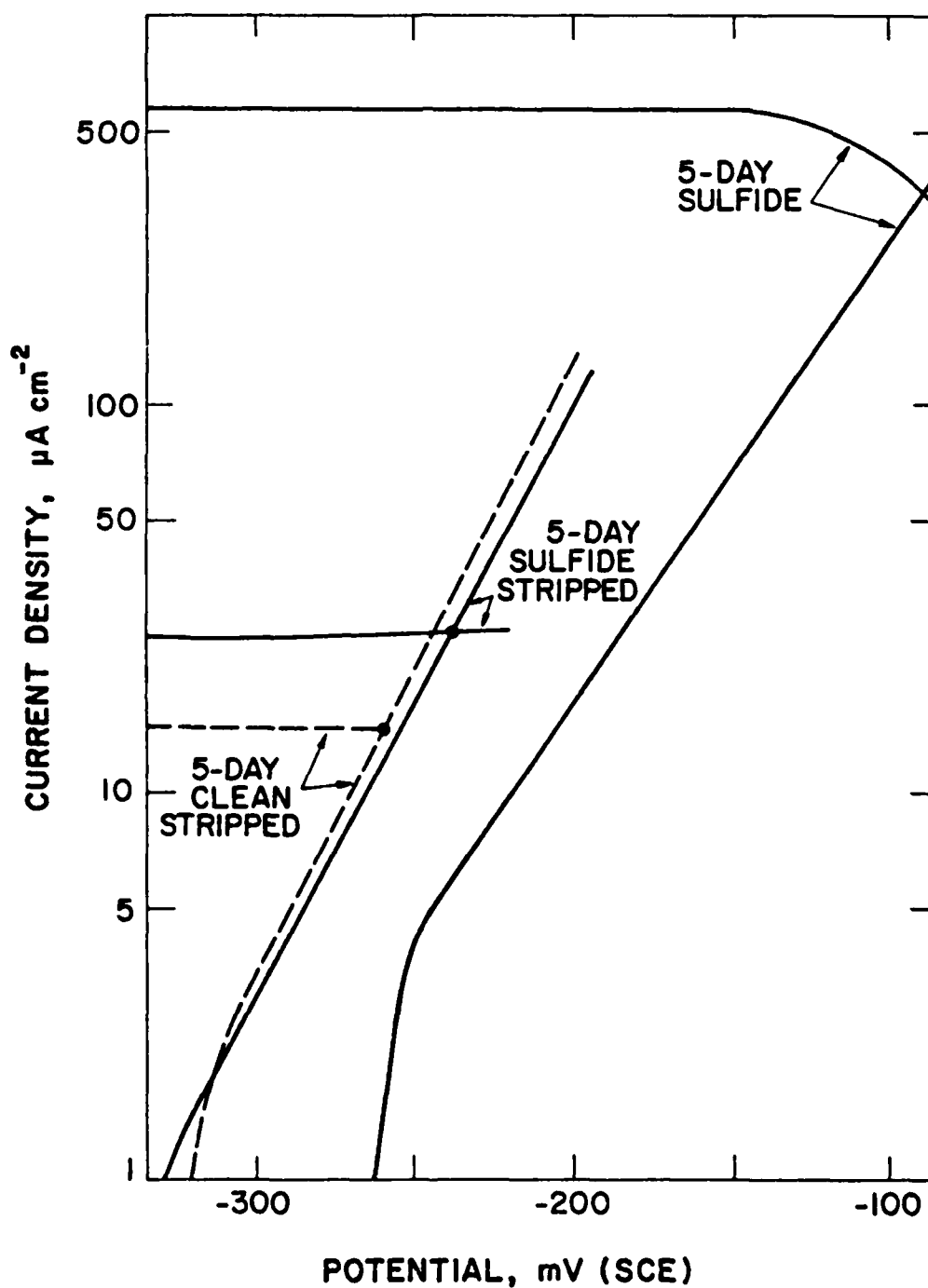


Figure 21. Effect of the adherent (inner) layer and of the detachable (outer) layer of the corrosion products after 5-day sulfide corrosion on the polarization curves.

## 5. DISCUSSION

### 5.1. Early State of Cu-Ni Alloy Corrosion in Clean 3.4 wt. % NaCl Solution

When Cu-9.4 Ni-1.7 Fe alloy is immersed in 3.4 wt. % NaCl solution, visible corrosion products start developing on the alloy surface within 8 minutes (29). This early stage of the corrosion mechanism was studied by making anodic and cathodic polarization curves on the fresh surface of the Cu-Ni alloy.

The anodic metal dissolution curves showed a rotation speed dependence and a Tafel slope of 60 mV per decade current decay (Figure 14). These two polarization behaviors are characteristic of the diffusion limited metal dissolution mechanism (7,8) and can be expressed by the modification of Equation (1), i.e., the following equations,

$$\ln i = \ln \left[ \frac{k_M^o}{k_{M^+}^o} \cdot C_M \cdot F \cdot \frac{D_{M^+}}{\delta} \right] + \frac{EF}{RT} \quad (18)$$

where  $\delta$  (diffusion thickness) can be expressed by the rotation speed of the disc sample and is

$$\delta = 0.643 \omega^{-1/2} \nu^{1/6} D_{M^+}^{1/3} \quad (19)$$

Combining Equations (18) and (19) gives

$$\ln i = \ln \left[ \frac{k_M^o}{k_{M^+}^o} \cdot C_M \cdot \frac{F D_{M^+}^{2/3}}{0.643 \nu^{1/6} \omega^{1/2}} \right] + \frac{FE}{RT} \quad (20)$$

Equation (11) shows the rotation speed dependent polarization curve. The Tafel of this curve ( $d \log i/dE$ ) is  $2.3 \frac{F}{RT} \sim 0.06$  V/decade at room temperature. Equation (11) explains the linear relationships of  $i$  vs.  $\omega^{1/2}$  that are shown in Figure 15. From these facts, it is reasoned that at the beginning of the alloy immersion the alloy dissolves probably as  $\text{CuCl}_2^*$  and the diffusion of  $\text{CuCl}_2^-$  from the electrode surface to the bulk solution is the rate determining step. Since the transfer of  $\text{CuCl}_2^-$  is slow, an accumulation of  $\text{CuCl}_2^-$  in the diffusion layer can be expected, thus the formation of  $\text{Cu}_2\text{O}$  by Reaction (y). According to this speculation,  $\text{Cu}_2\text{O}$  may be formed on the alloy surface; however, a major compound found in the corrosion product was  $\text{Cu}_2(\text{OH})_3\text{Cl}$  (Table 4), and its formation is explained in section 5.2.

The electrons produced by the anodic metal dissolution reaction are consumed by the cathodic reaction. The cathodic reaction in the potential range used in this experiment is identified as mainly oxygen reduction (Figure 13). The equilibrium potential of the oxygen reduction, Reaction (12), is expressed by the following equation:

$$E \text{ (SHE)} = 1.228 - 0.059 \text{ pH}^{**} \quad (21)$$

In solution of pH 7 to 8 the equilibrium potential is 0.7-0.8 V (SHE) (or 0.45-0.55 V (SHE)). Oxygen reduction on a Pt electrode is suggested to be expressed by the following reactions (46,47)

---

\* The Tafel slope of 60 mV/decade suggests that the diffusion of single charged species going away from the electrode surface is the rate-determining step.

\*\* Since the concentration of  $\text{H}^+$  is very small, unit activity coefficient is expected.



where M represents the Pt substrate. Considering pH dependence of the reaction rate and the Tafel slopes (110 mV/decade for oxygen reduction, 40 mV/decade for oxygen-evolution (46)), the second reaction (Reaction [11]) is suggested to be the rate-determining step.

Oxygen reduction on the fresh surface of the Cu-Ni alloy may have a different mechanism from that on the Pt electrode, since the Tafel slope found on the alloy surface is 260 mV/decade and on the Pt surface is 110 mV/decade (46). The potential range, where oxygen reduction has been studied (-350 mV to -150 mV (SCE)) is far from the equilibrium potential (+550 mV (SCE) at pH 8). In this high over-potential region a transport limited oxygen reduction rate may be expected. However, the polarization curves measured with various rotation speeds show a rotation speed independency. This cathodic oxygen reduction behavior may be explained on the basis of a thin anodic corrosion product (probably  $\text{Cu}_2\text{O}$ , as discussed above) which developed during the polarization measurements. It has been reported (46) that the polarization behavior is different on a bare platinum substrate compared with that on a substrate on which there is an oxide. The bare platinum is a better catalyst than the oxide-covered surface by about one-hundred times. Similarly, the thin corrosion product layer developed on the Cu-Ni surface may act as a bad catalyst for oxygen reduction, and as such this step determines the cathodic oxygen reduction rate. Another possible oxygen reduction reaction mechanism involves

electron transfer through the thin corrosion product layer. Anodically produced electrons must transfer through the layer to react with oxygen on the layer surface. The layer is possibly  $\text{Cu}_2\text{O}$  which is known to be a p-type semiconductor. According to a defect structure model (described in section 2.4), electronic resistance of the  $\text{Cu}_2\text{O}$  layer increases as proportionally larger amounts of Ni and Fe are oxidized and incorporated into the  $\text{Cu}_2\text{O}$  lattice. Thus, the slow movement of electrons in this layer may determine the oxygen reduction rate.

#### 5.2. Corrosion of Cu-Ni Alloy in Clean 3.4 wt. % NaCl Solution

The corrosion rate (weight loss) obtained from the polarization measurements on the rotating alloy disc are comparable to that from the weight loss data on the stationary electrode (29), Figure 18. These results show that during the "clean" corrosion, test weight loss increases with time by a parabolic rate law; this suggests that a diffusion step is rate determining.

After 5 days of immersion the corrosion product layers are well developed on the alloy surface. Based on the results obtained from the SEM, ESCA\*, and X-ray diffraction investigations, the corrosion product layer is reasoned to be constituted as shown in Figure 22. The corrosion products consist of three layers; a very porous outer layer

---

\* Although the ESCA investigation was conducted on the 3-day clean sample, a similar result should be obtained on the 5-day clean sample. The data obtained on the 3-day clean sample was consistent with that on the 3- and 4-day stationary sample (26).

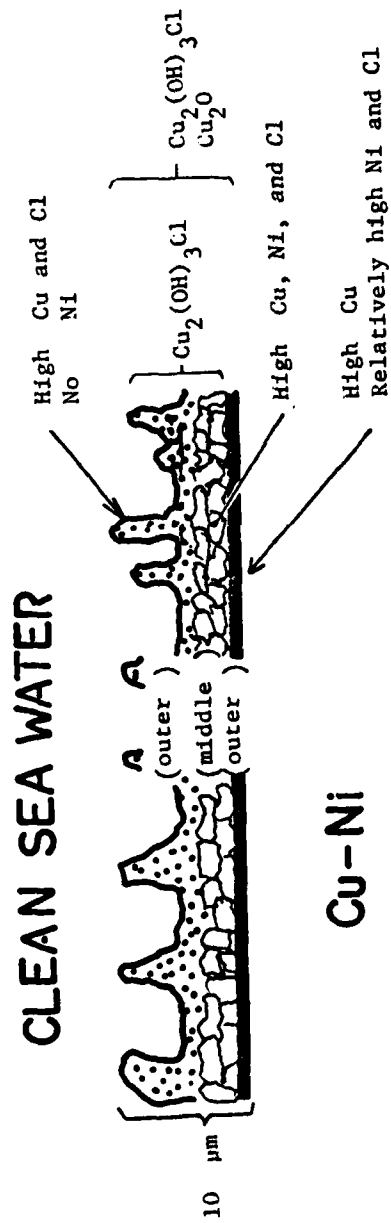


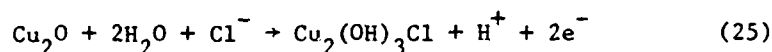
Figure 22. A schematic of the cross-section of the corrosion products on the Cu-Ni surface after the 5-day clean corrosion test.

with high concentrations of Cu and Cl, a relatively porous middle layer which contains a particularly high concentration of Ni, and a very thin inner layer which contains Cu and considerable amounts of Cl and Ni. By the physical stripping technique the outer and middle layers were detached from the inner layer. The inner layer is invisible on the photomicrograph of the cross-section (Figure 9); however, the ESCA examination shows the presence of Cl on the inner layer after stripping the outer and middle layers. This presence of the Cl is also confirmed after 60 seconds of ion sputtering on the inner layer surface, showing the area under examination is still within the corrosion products. The approximate thickness of the inner layer is between 5 nm and 500 nm. The lower limit is obtained from the ion sputtering (rate of  $0.02 \text{ nm-sec}^{-1}$  (26)) and the upper limit is from the resolution of the light microscope. The detachable outer and middle layers were identified to be  $\text{Cu}_2(\text{OH})_3\text{Cl}$  by the X-ray analysis. The thin inner layer was not identified directly, but is probably  $\text{Cu}_2\text{O}$ , since the X-ray analysis on the total corrosion layer showed  $\text{Cu}_2(\text{OH})_3\text{Cl}$  and  $\text{Cu}_2\text{O}$ .

The formation of  $\text{Cu}_2\text{O}$  is predicted for equilibrium conditions from the pH-potential diagrams (Figure 1), since the measured corrosion potential, -220 to -250 mV (SCE), in pH 7.5 solution (Table 7) suggests that the stable form of the corrosion product is  $\text{Cu}_2\text{O}$ . The mechanism of  $\text{Cu}_2\text{O}$  formation is suggested to involve the hydrolysis of  $\text{CuCl}_2^-$  within the diffusion layer (Reactions [1]-[3]). The formation of  $\text{Cu}_2(\text{OH})_3\text{Cl}$  at these potential/pH conditions is not possible (Figure 1), however, its formation has been observed by many investigators in actual and simulated sea water (26-28). The reason for the formation of  $\text{Cu}_2(\text{OH})_3\text{Cl}$  may

be obtained by considering localized concentration and electrode potential changes within the diffusion layer.

The reaction for the formation of  $\text{Cu}_2(\text{OH})_3\text{Cl}$  may be the following equation (22);



and the equilibrium potential of this reaction is:

$$E = 0.51 - 0.0296 \text{ pH} - 0.0296 \log (\text{activity of } \text{Cl}^-) \quad (26)$$

Inserting the values of pH (=7.5) and the activity of  $\text{Cl}^-$  ( $\sim 0.32$ ) (1) one obtains the equilibrium potential of 0.03 V (SCE), which is about 0.25 V higher than the measured corrosion potential; thus, the formation of  $\text{Cu}_2(\text{OH})_3\text{Cl}$  cannot be expected. However, the variables (pH and activity of  $\text{Cl}^-$  in Equation (13)) may vary within the diffusion layer and the actual values near the sample surface where the reaction occurs may be different from the values used (23,24).

The potential difference,  $\phi$ , in the diffusion layer can be expressed by the following equation (the derivation is in Appendix A):

$$\phi = \frac{RT}{F} \ln \frac{C_o}{C_o - \frac{1}{2} Yx} \quad (27)$$

where

$$Y = \frac{1}{F} \left( \frac{2}{D_{\text{Cl}^-}} - \frac{1}{D_{\text{CuCl}_2^-}} \right)$$

Since  $D_{\text{Cl}^-}$  is larger than  $D_{\text{CuCl}_2^-}$  (see section 2.3), the calculated value of Y is always negative. Therefore,  $\phi$  is negative and decreases as x



increases. This indicates that the potential at the metal/solution interface is lower than the measured potential and does not support the formation of  $\text{Cu}_2(\text{OH})_3\text{Cl}$  which requires a high potential at the metal/solution interface. Moreover, the value of  $Y$  is so small (see section 2.3) that  $\phi$  is eventually 0, thus, the measured potential and the potential at the metal/solution are about the same.

The activity, thus, the concentration of  $\text{Cl}^-$  near the alloy surface is determined by Equation (8). By putting suitable values into the equation, one can obtain the concentration of  $\text{Cl}^-$  at the metal surface which is approximately the same as the value of the bulk. Thus, potential shifts due to the  $\text{Cl}^-$  activity changes cannot be expected.

The explanation for the formation of  $\text{Cu}_2(\text{OH})_3\text{Cl}$  may be the changes of pH near the sample surface. In the calculation of the various ionic species concentrations (section 2.3), the concentrations of  $\text{H}^+$  and  $\text{OH}^-$  are ignored because of their small values. If  $\text{H}^+$  and  $\text{OH}^-$  ions are considered in the calculations,  $\text{H}^+$  and  $\text{Na}^+$  ions probably show similar behavior due to their positive charges. The concentration of  $\text{Na}^+$  is higher at the metal/solution interface than at the bulk solution (see Equation (9) and the value of  $Y$  in section 2.3), thus one can expect lower pH at the metal/solution interface than in the bulk solution. This does not help the formation of  $\text{Cu}_2(\text{OH})_3\text{Cl}$  at the alloy surface, since the potential in Equation (26) increases as pH decreases.

The pH changes near the alloy surface can be caused by the cathodic oxygen reduction. Oxygen reduction is found to be independent of the rotation speed (Figure 14, 19). Thus, pH changes in the diffusion layer cannot be expected. However, in the oxygen reduction

reaction (may be similar to Reactions (22)-(24)) it is possible to have a high concentration of  $\text{OH}^-$  as adsorbed ions on the alloy surface. If this is true, then the adsorbed  $\text{OH}^-$  ions may bring the pH up, thus, the equilibrium potential of the Equation (26) can be brought into the corrosion potential, and the formation of  $\text{Cu}_2(\text{OH})_3\text{Cl}$  becomes possible.

With the presence of the corrosion products on the Cu-Ni alloy surface the following changes in the anodic polarization curves are observed: (i) the polarization curves shift their positions to more noble potentials while keeping the Tafel slope of 60 mV per decade current (Figure 16), and (ii) the polarization curves become independent of rotation speed. Another set of polarization measurements conducted on the inner layer of the corrosion products (after stripping the loosely adherent corrosion products) showed that the curve on the inner layer is identical to the curve on the fresh surface (curve B in Figure 19-a) and is rotation speed dependent. This indicates that the outer loosely adherent layer rather than the inner layer is responsible for the changes found in the anodic polarization curves. The Tafel slope of 60 mV per current decay indicates the mass transfer limited anodic reaction rate (7). Since the polarization curves on the outer layer are independent of the rotation speed, diffusion of the metal cation through the solution near the electrode surface<sup>\*</sup> can not be the rate determining step. Therefore, the diffusion of the metal cations through the loosely adherent corrosion products or through the solution inside the pores<sup>+</sup> of the corrosion products may be the rate

---

\* Which is the rate determining step on the fresh surface.

<sup>+</sup> The aqueous solution inside the pores should be stagnant in the porous middle and outer corrosion products.

AD-A107 393

PENNSYLVANIA STATE UNIV UNIVERSITY PARK APPLIED RESE--ETC F/8 7/4  
CORROSION MECHANISM OF CU-9.4 NI-1.7 FE ALLOY IN 3.4 WT.% NaCl --ETC(U)  
AUG 81 C KATO  
N00024-79-C-6043  
NL

UNCLASSIFIED

AKL/PSU/TM-81-181

2 # 2

24

24

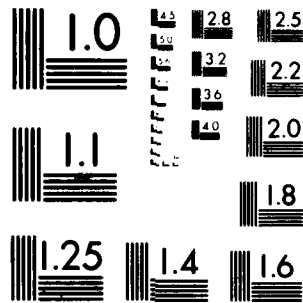
END

DATE

FORMED

12 R

OTIC



MICROCOPY RESOLUTION TEST CHART  
NATIONAL BUREAU OF STANDARDS 1963-A<sub>1</sub>

determining process. Since  $\delta$  (diffusion layer thickness in the stagnant solution inside of the pores) is independent of  $\omega$  (rotation speed) and increases with increasing time of immersion, the value  $\left(\frac{k_M^O}{k_M^{O+}} \cdot C_M \cdot F \cdot \frac{D_{M+}}{\delta}\right)$  decreases in Equation (18). This explains the shift of the anodic polarization curve due to the formation of the corrosion product layers (Figure 16).

The cathodic oxygen reduction curves were also more polarized following the formation of corrosion product layers during the alloy immersion. Oxygen reduction involves the oxygen molecule coming to the reaction site within the corrosion product layers where anodically produced electrons are available. Then, the reaction occurs and the products move to the bulk solution. The polarization measurements conducted on the outer layer surface and on the inner layer surface showed a rotation speed independency. This indicates that neither diffusion of the reactants nor of the products in the electrode surface boundary layer is the rate determining step. By stripping the loosely adherent corrosion products the oxygen reduction rate was increased. An increased reaction rate was also observed with a Pd coating on the inner layer surface (Figure 19-a) and the increased rate showed a rotation speed dependency. Since Pd is a well-known good catalyst\* for oxygen reduction, the increased rate on the Pd coating suggests that the inner layer surface is not a good catalyst for oxygen reduction. This suggestion is only valid if the Pd did not penetrate the inner layer and make direct contact with the alloy (which would allow

---

\*The exchange current density of oxygen reduction is about one order of magnitude greater on Pd than on Pt (48).

short circuiting of electrons through the inner layer). Thus, one of the following processes can be the rate determining step:

(1) The corrosion product layer is a poor catalyst for oxygen reduction and this poor catalytic capability degrades further with increasing immersion.

(2) Diffusion of  $e^-$  through the corrosion produce is slow and determines the oxygen reduction rate (which is suggested by other investigators (28,32)).

The corrosion potentials and currents are determined by the intersection of the anodic and cathodic polarization curves shown in Figure 13. At this intersection the anodic and cathodic reaction occur at the same rate. The corrosion rate (metal loss) is a direct product of the metal dissolution. Since the anodic metal dissolution rate is controlled by a diffusion limited process, the weight loss versus the immersion period relationship should show the parabolic rate behavior which is actually found, Figure 18.

### 5.3. Effect of Sulfide on Corrosion of the Cu-Ni Alloy

A model of the corrosion product layers developed after 5-days of the sulfide corrosion is suggested by the SEM, ESCA, and X-ray diffraction studies, and is shown in Figure 23. The layers consist of: (i) a very porous outer layer, containing high concentrations of Cu and S, (ii) lamellae of middle layers, and (iii) a very thin inner layer containing Cu, Ni, and a low concentration of S. The middle layers again consist of a few thin sub-layers and each sub-layer has a characteristic composition. The outer and middle layers are loosely

# SEA WATER WITH SULFIDE

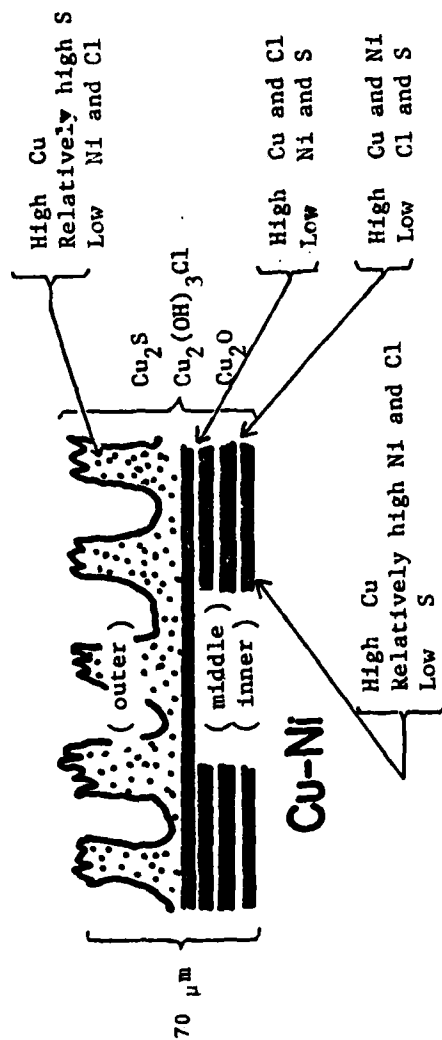


Figure 23. A schematic of the cross-section of the corrosion products on the Cu-Ni surface after the 5-day sulfide corrosion test.

adherent and can be stripped with polytape. Similar to the corrosion products developed after the 5-day clean corrosion, the middle layer facing the adherent inner layer contains high concentrations of the alloying elements and the Cu to Ni ratio is 1 to 1. The sulfide concentration decreases with the distance from the outer layer surface and the inner layer contains less than 2 at. % of sulfide. The X-ray diffraction analysis showed that the corrosion products are  $\text{Cu}_2\text{S}$  and  $\text{Cu}_2(\text{OH})_3\text{Cl}$  and may contain a small amount of  $\text{Cu}_2\text{O}$ .

The corrosion potentials found during the polarization measurements indicate a relatively noble potential, (Table 9) of -160 to -60 mV (SCE), and is more noble than those potentials of the Cu-Ni alloy corroded without sulfide contamination (-230 to -250 mV (SCE)). This noble corrosion potential does not agree with the corrosion potentials measured by other investigators (39,42), -500 to -800 mV (SCE). If the corrosion potential is lower than -700 mV (SCE) in pH 7.5 solution, hydrogen evolution is expected as the cathodic reaction in addition to the oxygen reduction reaction. This additional hydrogen ion reduction is one of the proposed mechanisms which explain the higher corrosion rate of Cu in sulfide-polluted solution (42). In this experiment a relatively noble corrosion potential is measured, a potential for which hydrogen evolution is impossible; however, the corrosion current was high enough to show the higher corrosion rate of the alloy in sulfide-polluted solution (Table 7).

The anodic curves on the alloy corroded in sulfide may shift their positions in the more noble direction in the presence of the outer layer while maintaining the linear relationship of the log



current density versus the potential (Figure 20). This potential shift can be seen for the alloy corroded under clean or sulfide conditions; furthermore, the magnitude of the potential shift is about the same for both conditions, and is explained in section 5.2.

The cathodic polarization curves of the oxygen reduction rate show a potential-independent behavior. The curve, however, is much higher on the sulfide corroded alloy than on the clean corroded alloy (Figure 20). This suggests that the increased corrosion current due to the sulfide addition is caused by the increased cathodic rather than the more polarized anodic reaction rate. This follows since only the cathodic curve is shifted to higher currents by the sulfide addition.

The polarization curves produced on the inner layer after stripping the loosely adherent layers showed a reduced oxygen reduction rate instead of the increased rate found on the inner layer developed in clean solution. Both of the curves produced on the inner layers of the clean and sulfide corrosion are almost identical. Furthermore, the ESCA semi-quantitative studies suggest that the inner layers of the clean and sulfide conditions are very similar and have the following properties:

- (i) they are brown in color, adherent to the alloy, and very thin (the X-ray diffraction analysis and SEM cross-sectional study cannot identify its presence due to its small thickness ( $>1 \mu\text{m}$ ), and
- (ii) they contain a relatively high concentration of  $\text{Cl}^-$  anions (10-20 at. %) and Cu and Ni cations (ratio of 2-5 to 1).

Upon comparing the polarization measurements on a Pd-coated inner layer (Figure 19-a) and on the 5-day sulfide corrosion product

layer (Figure 20), it can be recognized that the higher cathodic (oxygen reduction) rate ( $500 \mu\text{A}/\text{cm}^2$ ) can be obtained on both of these surfaces but not on the stripped (bare inner) surface. This high oxygen reduction rate is the diffusion limited value since the current increases with the rotation speed of the sample electrode (Figure 19-b), i.e., the reduction rate is controlled by the diffusion of the reactant (oxygen) or the product ( $\text{OH}^-$  ions) in the solution. To maintain this high rate of oxygen reduction, electron migration through the corrosion product is required, and must be intrinsically an easy (fast) process.

To continue the discussion on the rate determining step and the effect of the sulfide, let us assume that the inner layer is dense and continuous. Then, the electrons consumed by oxygen reduction must migrate through the inner layer from the alloy; thus, (in accord with the above mentioned data) the inner layer is a good electronic conductor. In this case the low oxygen reduction rate which occurs on the bare inner layer (Figure 21) is explained by a slow (rate determining) electrochemical reaction rate of the oxygen reduction reaction. It follows that the outer layer developed in the clean solution is not a good catalyst for oxygen reduction in accord with its relatively low current (Figure 19-a); whereas, the outer layer developed under the sulfide-contaminated condition has a good catalytic nature for  $\text{O}_2$  reduction, resulting in high currents (Figure 20).

On the other hand, if the assumption is made that the inner layer is continuous and a poor electron conductor, a high current could still be obtained if the electrons consumed by the oxygen reduction reaction could reach the layer/electrolyte reaction site

via a good electron-conducting path such as Pd (when vapor deposited on the layer) or sulfide-containing reaction product which penetrates the inner layer. Under this condition a low oxygen reduction rate on the bare inner layer (after removing the sulfide-containing outer layer) (Figure 21) can not be explained, since the heterogeneous inner layer should be able to maintain a relatively high current.

There may be another explanation for the obtained results. The surface oxide on a metal surface must be regarded as a semiconductor due to a loss of metallic character. It is known that in semiconducting materials the rate of the electrochemical reaction depends on the rate of supply of minority carriers between the metal/semiconductor and semiconductor/electrolyte interfaces, assuming that they are consumed in the reaction (49). If a cathodic reaction (in which the electrons are extracted from the semiconductor) occurs on a p-type semiconductor, electrons in the semiconductor are consumed in the reaction, resulting in a limiting current (potential independent current) in the polarization curve. This may explain the reduced oxygen reduction rate on the corrosion product layers which contain the p-type semiconductor  $\text{Cu}_2\text{O}$ . In this case the good conduction of the inner layer developed in the sulfide contaminated condition could be explained by the small concentration of sulfide (Table 6) in the inner layer which increases the number of charge carriers.

The correct explanation must take into account the observed poor catalytic nature of the inner layer developed under both the clean and sulfided conditions. An important feature of electrode kinetics associated with the presence of the semiconductive film is

that it lowers the exchange current density for oxygen reduction below that of the metal. It was shown that the bare platinum is a better catalyst than the oxide-covered surface by about one-hundred times (46). The explanation for this behavior is made by Vijn (49) and involves the states of electrons in metal and semiconductor. In semiconductors the Fermi level lies within the forbidden gap where there are no electrons available. However, for the metal case, there are always electrons available at the Fermi level. No further qualitative analyses of this behavior is made for the Cu-Ni alloys. However, this explanation can be applied to the system of Cu/Cu oxide/sea water (dissolved oxygen), to account for the poor catalytic nature of the Cu oxide surface for oxygen reduction.

The measured high oxygen reduction rate on the sulfide layer and on the Pd-coated inner layer can be explained in terms of unpaired d-electrons. The catalytic ability depends on the electronic structure, such as the presence of the unpaired d-electrons (50). The number of unpaired d-electrons per atom changes from about 0.6 for Pd to 0 for a Pd-60 at. % Au. The exchange current density measured on Pd-Au alloy shows that it decreases as Au content in the alloy increases (51). This indicates that the exchange current density increases with the number of unpaired d-electrons per atom. This is because the unpaired d-electrons may be engaged in bonding with oxygen or oxygen-containing species at the surface, thus increasing the exchange current density. The unpaired d-electrons affect the catalytic capability of transition metal compounds as well as transition metals. Ahmed (52,53) studied oxygen reduction on  $\text{Co}_3\text{S}_4$ ,  $\text{FeS}_2$  and  $\text{PbS}$ . He found that the oxygen

reduction rate varies as  $\text{Co}_3\text{S}_4 > \text{FeS}_2 \gg \text{PbS}$ , and suggested that this variation is due to the number of unpaired d-electrons per atom.

It is also interesting to note that the oxygen reduction rate of the transition metal-sulfide compounds ( $\text{FeS}_2$ ) does not depend on semiconducting type, however, it is very sensitive to doping with another transition metal (54). It was shown that a sulfide of composition  $\text{Fe}_{0.5}\text{Ni}_{0.5}\text{S}_2$  is 40 times more active than  $\text{FeS}_2$  for oxygen reduction (54). This is probably due to the improvement of the adsorbability of reactants or intermediate products on the surface of the sulfide compound, although, the actual mechanisms of this process is not well understood (54,55).

In the present work transition metals of Ni and Fe are alloyed with Cu. The ESCA examination revealed that these alloying elements coexist with sulfide in the middle layers with a relatively high concentration. Therefore, the good adsorbability of the reactants on the transition metal-sulfide compound can be expected in our system. Further understanding of the oxygen reaction mechanism on metal oxide and sulfide will be very important for future investigation of the Cu-Ni alloy corrosion.

## 6. CONCLUSIONS

The following conclusions can be drawn from data discussed:

1. The weight loss of the alloy, immersing into the clean 3.4 wt. % NaCl solution, increases with the time according to a parabolic rate law. This is due to the diffusion limited anodic metal dissolution rate. The cathodic oxygen reduction reaction is probably controlled by the poor catalytic nature of the oxygen reduction on the corrosion product which covers the alloy surface.

2. The corrosion product developed in the clean solution is relatively thin (about 10  $\mu\text{m}$  for the 5-day immersion) and consists of  $\text{Cu}_2(\text{OH})_3\text{Cl}$  and  $\text{Cu}_2\text{O}$ . The corrosion products in sulfide-contaminated solution are thick (about 70  $\mu\text{m}$  for the 5-day immersion) and consist of  $\text{Cu}_2\text{S}$ ,  $\text{Cu}_2(\text{OH})_3\text{Cl}$ , and probably  $\text{Cu}_2\text{O}$ . These corrosion products developed under both the clean and sulfide-contaminated solutions have a multi-layer arrangement. The outer and middle layers are porous and brittle and can be stripped with poly-tape. The inner layers developed under both the clean and sulfide conditions are thin and adherent to the alloy surfaces, and they show similar results in the ESCA semi-quantitative and the polarization studies.

3. The corrosion current obtained in sulfide-contaminated solution is  $400 \mu\text{A}/\text{cm}^2$  at the 5-day immersion time, and is much higher than the clean condition ( $2.2 \mu\text{A}/\text{cm}^2$ ). This high corrosion rate is attributed to the increased cathodic oxygen reduction rate which is obtained by the better oxygen reduction catalyst on the sulfide corrosion products.

#### REFERENCES

1. Bianchi, G. and P. Longhi, Corrosion Sci., 13, 853 (1973).
2. Verink, E. D., "Electrochemical Techniques for Corrosion," R. Baboian, Editor, NACE, Houston, Texas (1977).
3. Morr, E. D. and A. M. Beccaria, Proc. 3rd. Int. Congr. Mar. Corr. Fouling, 2-6 Oct., Gaithersburg, Maryland (1972).
4. Verink, E. D., Jr., Corrosion, 23, 371 (1967).
5. Pourbaix, M., Corrosion, 26, 431 (1970).
6. Efird, K. D., Corrosion, 31, 77 (1975).
7. Bockris, J. O'M., B. T. Rubin, A. Despic and B. Lorreck, Electrochimica Acta, 17, 973 (1972).
8. Bonfiglio, C. H., H. C. Albaya and O. A. Cobo, Corrosion Sci., 13, 717 (1973).
9. Stephenson, L. S. and J. H. Bartlett, J. Electrochem. Soc., 101, 571 (1954).
10. Bacarella, A. L. and J. C. Griess Jr., J. Electrochem. Soc., 120, 461 (1973).
11. Walton, M. E. and P. A. Brook, Corrosion Sci., 17, 317 (1977).
12. Pickering, H. W. and C. Wagner, J. Electrochem. Soc., 114, 698 (1967).
13. Pickering, H. W. and P. J. Byrne, J. Electrochem. Soc., 116, 1492 (1969).
14. Takasu, Y., H. Shimizu, S. Maru, M. Tomori and Y. Matsuda, Corrosion Sci., 16, 159 (1976).
15. Castle, J. E., Nature Physical Science, 234, 93 (1971).
16. Kruger, J., Corrosion, 22, 88 (1966).
17. Kruger, J., J. Electrochem. Soc., 106, 847 (1959).
18. Kruger, J., J. Electrochem. Soc., 108, 503 (1961).
19. Ives, D. J. G. and A. E. Rawson, J. Electrochem. Soc., 109, 447 (1962).

20. North, R. F. and M. J. Pryor, Corrosion Sci., 11, 353 (1971).
21. Bacarell, A. L. and J. C. Griess, Jr., J. Electrochem. Soc., 120, 459 (1973).
22. Taylor, H. J., J. Electrochem. Soc., 118, 854 (1971).
23. Ateya, B. G. and H. W. Pickering, Accepted for Publication in J. Applied Electrochem.
24. Albery, J., "Electrode Kinetics," Clarendon Press, Oxford (1975).
25. White, R., J. A. Trainham and J. Newman, J. Electrochem. Soc., 124, 669 (1977).
26. Kato, C., B. G. Ateya, J. E. Castle, and H. W. Pickering, J. Electrochem. Soc., 127, 1897 (1980).
27. Ijesseling, F. P. and J. M. Kroughman, Proceedings of 6th European Congress of Metallic Corrosion, p. 181, Society of Chemical Industry, London (1977).
28. Popplewell, J. J., R. J. Hart, and J. A. Ford, Corrosion Sci., 13, 295 (1973).
29. Kato, C., B. G. Ateya, J. E. Castle and H. W. Pickering, J. Electrochem. Soc., 127, 1890 (1980).
30. Bailey, G. L., J. Inst. Metals, 77, 243 (1951).
31. Stewart, W. C. and F. L. Lague, Corrosion, 8, 259 (1952).
32. North, R. F. and M. J. Pryor, Corrosion Sci., 10, 297 (1970).
33. Macdonald, D. D., B. C. Syrett and S. S. Wing, Annual Report of SRI International "A study to determine the mechanisms of corrosion of copper-nickel alloys in sulfide-polluted seawater" (1978).
34. Kubschewski, O. and B. Hopkins, "Oxidation of Metals and Alloys," Butterworths, London, p. 21 (1967).
35. Mor, E. D. and A. M. Beccaria, Br. Corros. J., 10, 33 (1975).
36. Mor, E. D. and A. M. Beccaria, Corrosion, 10, 354 (1974).
37. Syrett, B. C., Corrosion, 33, 257 (1977).
38. Bates, J. F. and J. M. Popplewell, Corrosion, 31, 269 (1975).



39. Syrett, B. C., S. S. Wing and D. D. Macdonald, Annual Report of SRI International "A study to determine the mechanisms of corrosion of copper-nickel alloys in sulfide-polluted seawater" (1979).
40. Redfied, A. C. and H. H. Uhlig, "Corrosion Handbook," Wiley and Sons, New York, p. 1118 (1948).
41. Butler, G. and H. K. C. Ison, "Corrosion and Its Prevention in Waters," Reinhold, New York, p. 25 (1966).
42. Syrett, B. C., D. D. Macdonald, and S. S. Wing, Corrosion, 35, 409 (1979).
43. Macdonald, D. D., B. C. Syrett and S. S. Wing, Corrosion, 34, 289 (1978).
44. Kato, C., M. S. Thesis, "Mechanism of Protective Layer Formation on Copper-Nickel Alloy in Simulated Sea Water," The Pennsylvania State University (1978).
45. Jorgensen, C. K. and H. Berthou, Discuss. Faraday Soc., 54, 269 (1972).
46. Bockris, J. O'M. and A. K. N. Reddy, "Modern Electrochemistry," Vol. 2, Plenum Press, New York, p. 1251 (1970).
47. Bockris, J. O'M. and B. Conway, "Modern Aspects of Electrochemistry," Vol. 5, Plenum Press, New York, p. 369 (1969).
48. Hoar, J., "Encyclopedia of Electrochemistry of the Elements," Vol. 2, A. J. Bard, Editor, p. 209, Marcel Dekker, New York (1974).
49. Vijh, A., "Electrochemistry of Metals and Semiconductors," Marcel Dekker, New York (1973).
50. Bockris, J. O'M. and B. E. Conway, "Modern Aspects of Electrochemistry," No. 5, Plenum Press, New York, pp. 350-479 (1969).
51. Damjanovic, A. and V. Brusic, Electrochim. Acta, 12, 1171 (1967).
52. Ahmed, S. M., International Journal of Mineral Processing, 5, 163 (1978).
53. Ahmed, S. M., International Journal of Mineral Processing, 5, 175 (1978).
54. Biegler, T., J. Electroanal. Chem., 70, 265 (1976).

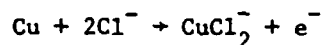
- 55. Bockris, J. O'M. and B. E. Conway, "Modern Aspect of Electro-chemistry," No. 9, Plenum Press, New York, pp. 369-478 (1974).

## APPENDIX A

### MATHEMATICAL INVESTIGATION OF Cu DISSOLUTION VIA $\text{CuCl}_2^-$ IONS IN 3.4 wt. % NaCl SOLUTION

Consider a planar surface of Cu schematically shown in Figure

24. Anodic dissolution of Cu,



takes place on the Cu surface of  $x = \delta$ .  $\delta$  is the thickness of the diffusion layer and  $x < 0$  is bulk solution where constant concentrations of  $\text{Cl}^-$  and  $\text{Na}^+$  and absence of  $\text{CuCl}_2^-$  are assumed. The ionic species  $\text{H}^+$  and  $\text{OH}^-$  are ignored due to the small concentration of  $[\text{H}^+] = [\text{OH}^-] \approx 10^{-7} \text{ mol-l}^{-1}$  in the almost neutral 3.4 wt. % NaCl solution ( $[\text{Na}^+] = [\text{Cl}^-] = 0.6 \text{ mol-l}^{-1}$ ).

For the sake of an approximation the transport equations for dilute solutions without regard to ionic interaction will be used.\* Then the Nernst-Einstein equation interrelating diffusivity and electrochemical mobility holds. Thus, the equations for the fluxes of the various ionic species for steady-state conditions in accord with the electrode processes are:

$$j_1 = -D_1 \left( \frac{dC_1}{dx} - C_1 \frac{F}{RT} \frac{d\phi}{dx} \right) = \frac{2i}{F} \quad (1)$$

---

\* Since the corrosion current of the Cu-Ni alloy in sea water is very low ( $\approx 20 \mu\text{A-cm}^{-2}$ ) and the concentrations of the ionic species in the electrolyte are relatively low, it is not necessary to consider the ionic interaction (24).

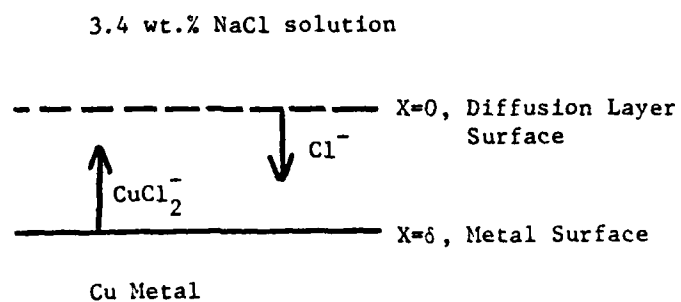


Figure 24. A schematic model of Cu dissolution in 3.4 wt. % NaCl solution.

$$j_2 = -D_2 \left( \frac{dC_2}{dx} + C_2 \frac{F}{RT} \frac{d\phi}{dx} \right) = 0 \quad (2)$$

$$j_3 = -D_3 \left( \frac{dC_3}{dx} - C_3 \frac{F}{RT} \frac{d\phi}{dx} \right) = -\frac{i}{F} \quad (3)$$

where

subscript 1, 2 and 3:  $\text{Cl}^-$ ,  $\text{Na}^+$ , and  $\text{CuCl}_2^-$ , respectively,

$j_i$ : flux of ionic species  $i$ ,

$D_i$ : diffusivity of ionic species  $i$ ,

$C_i$ : concentration of ionic species  $i$ ,

$\delta$ : distance from the diffusion layer surface to the metal surface

$\phi$ : electrical potential in the solution (with  $\phi = 0$  at  $x = 0$ ).

The flux of  $\text{Na}^+$  (species 2) vanishes according to Equation (2) since  $\text{Na}^+$  is neither formed nor consumed by the electrode reactions stated in Reaction [1]. The right-hand member of Equation (1) has a positive sign since  $\text{Cl}^-$  is consumed by the anodic process stated in Reaction [1] and, therefore,  $\text{Cl}^-$  must move to the metal surface. The righthand member of Equation (3) has a negative sign since complex Cu ions are formed anodically and, these species move outward in the negative direction of the  $x$ -coordinate.

The concentrations of the ionic species must conform to the law of electrical neutrality. Thus,

$$C_2 = C_1 + C_3 \quad (4)$$

The boundary conditions pertaining to the differential Equations (5) to (7) are:

$$C_1 = C_2 = C_0 \quad \text{at } x = 0 \quad (5)$$

$$C_3 = 0 \quad \text{at } x = 0 \quad (6)$$

$$\phi = 0 \quad \text{at } x = 0 \quad (7)$$

Equations (1) to (7) are sufficient in order to calculate the unknowns  $C_1$ ,  $C_2$ ,  $C_3$ ,  $C_4$ , and  $\phi$  as functions of distance  $x$ . Dividing Equations (1) and (3) by  $D_1$  and  $D_3$ , respectively, adding corresponding sides, and substituting Equation (2), one has

$$-\frac{dC_2}{dx} + C_2 \frac{F}{RT} \frac{d\phi}{dx} = Y \quad (8)$$

where

$$Y = \frac{1}{F} \left( \frac{2}{D_1} - \frac{1}{D_3} \right) \quad (9)$$

From Equations (2) and (9) it follows that

$$\frac{dC_2}{dx} = \frac{1}{2F} \left( \frac{2}{D_1} - \frac{1}{D_3} \right) = -\frac{1}{2} Y \quad (10)$$

$$\frac{Fd\phi}{RTdx} = \frac{1}{2FC_2} \left( \frac{2}{D_1} - \frac{1}{D_3} \right) = \frac{1}{2} \frac{Y}{C_2} \quad (11)$$

Integrating Equation (10) and using the boundary condition in Equation (5), one has

$$C_2 = C_0 - \frac{1}{2} Yx \quad (12)$$

Substituting Equation (12) into (11), integrating, using the boundary condition in Equation (7), and introducing the symbol  $\psi = F\phi/RT$ , one has

$$\psi = \frac{F\phi}{RT} = \ln \frac{C_o}{C_o - \frac{1}{2} Yx} \quad (13)$$

Integrating (1) and (3) and using the corresponding boundary conditions, one obtains

$$C_1 = e^{\psi(x)} \cdot \frac{2i}{D_1 F} \int_0^x e^{-\psi(x)} dx \quad (14)$$

$$C_3 = \frac{1}{D_3 F} e^{\psi(x)} \int_0^x e^{-\psi(x)} dx \quad (15)$$

where  $\psi = (F\phi/RT)$  as a function of  $x$  is given by Equation (13). Substituting Equation (13) into Equations (14) and (15), and integrating, one obtains

$$C_1 = C_o - \frac{2i}{D_1 F} \left[ \frac{C_o x - \frac{Yx^2}{4}}{C_o - \frac{Yx}{2}} \right] \quad (16)$$

$$C_3 = \frac{1}{D_3 F} \left[ \frac{C_o x - \frac{Yx^2}{4}}{C_o - \frac{Yx}{2}} \right] \quad (17)$$

Equations (16), (12), and (17) show the concentrations of species 1, 2, and 3, at a distance  $x$ . Equation (13) shows the potential at a distance  $x$  when  $\phi = 0$  at  $x = 0$ .

## APPENDIX B

### DETERMINATION OF FLOW RATES OF $H_2$ AND $H_2S$ GASES

A gas mixture of  $H_2S$  and  $H_2$  was used as a source of sulfide in the simulation of the polluted sea water. Considering the actual polluted sea water, a combination of sulfide concentration from 5 to 10 ppm and pH of 7.0 to 7.5 was thought to be a severe corrosive environment for the Cu-Ni alloys. In order to obtain and keep these sulfide concentrations and pH, a certain flow rate ratio of  $H_2S/H_2$  gas mixture bubbled through the deaerated 3.4 wt. % NaCl solution (initially pH-adjusted to 7.5) had to be determined. Therefore, the sulfide concentration and pH measurements (shown in Appendix C) were conducted for different ratios of flow rates of the gases.

The flow rates of the gases were controlled by a manometric flowmeter. The flow rates were obtained from the difference between the levels of the liquid (Di-butyl phthalate for  $H_2$  and silicon oil for  $H_2S$  gas) in the two arms of the manometer. For the different range of flow rates, different capillary tubes were attached to the flowmeters. The flowmeters were calibrated by time and gas volume measurements. This was done by a simple bubble meter that included a flask and a graduated tube of known volume. The bubble was created by mixing detergent and water. The time necessary for a soap film to pass through a known volume was measured ten times and averages were computed for each pressure. Figures 25 and 26 show the flow rate vs. pressure head difference for  $H_2$  gas and  $H_2S$  gas, respectively.



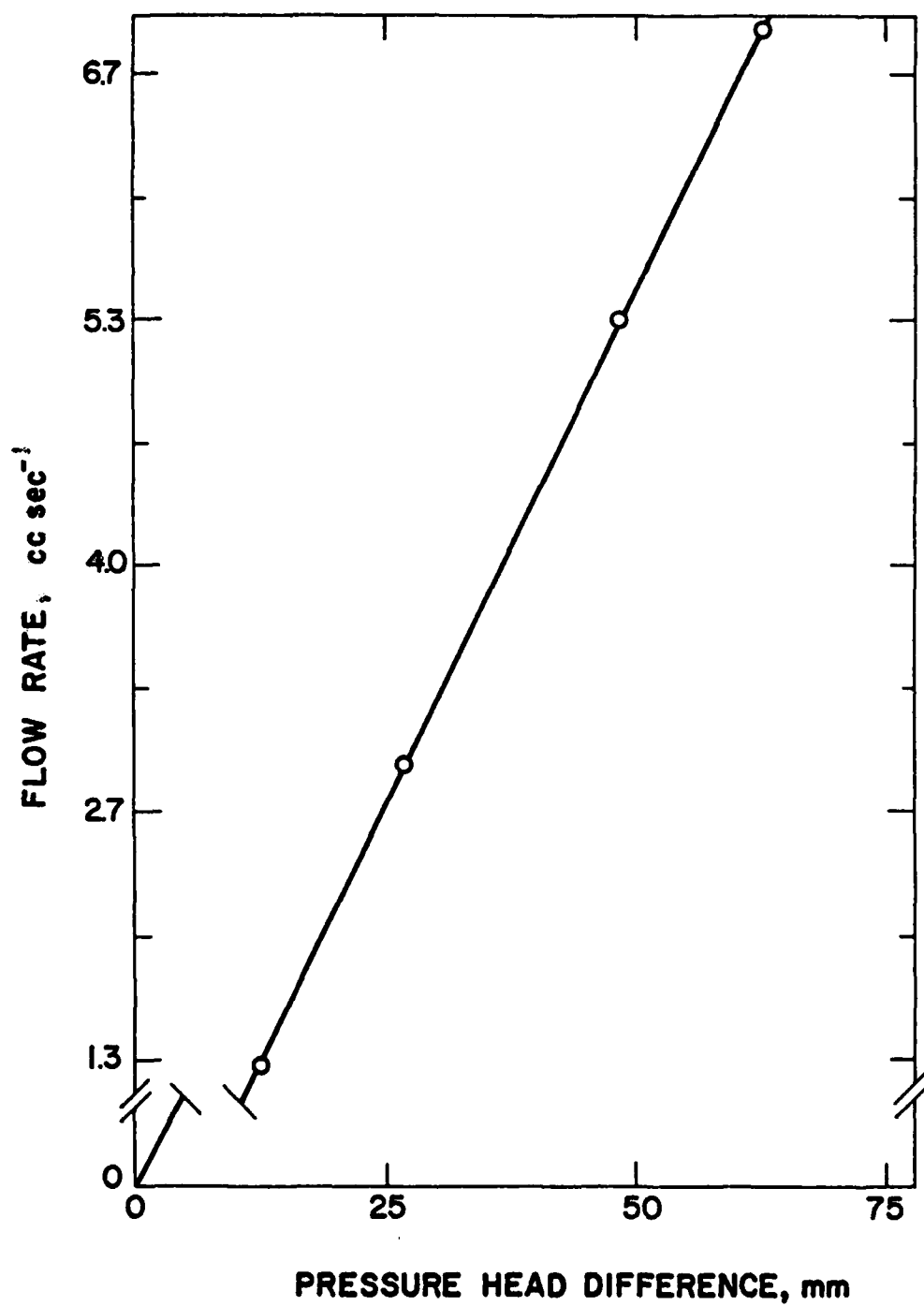


Figure 25. Flow rate versus pressure head difference for H<sub>2</sub> gas.

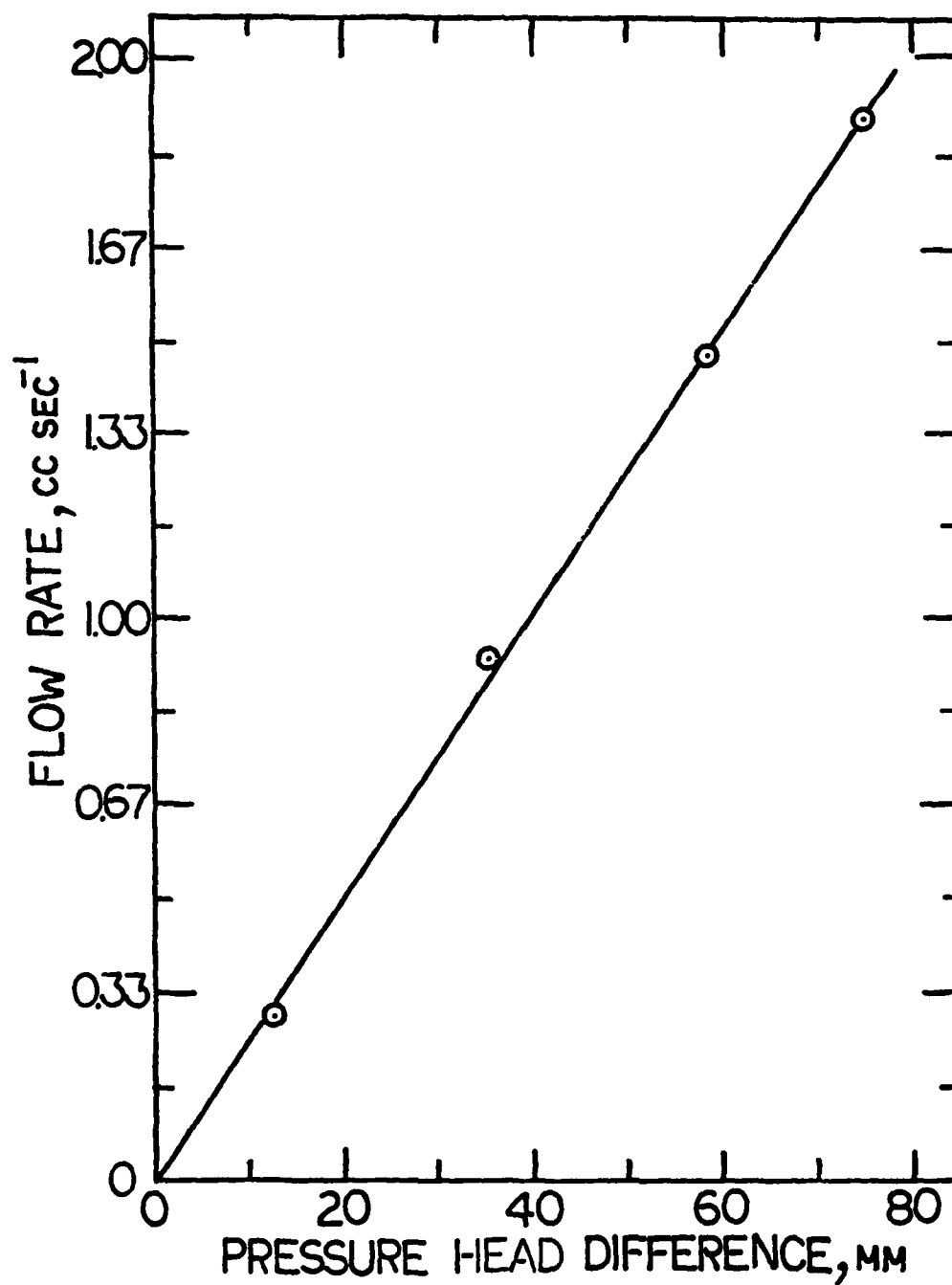


Figure 26. Flow rate versus pressure head difference for H<sub>2</sub>S gas.

In order to vary the concentration of sulfide, the flow rate of  $H_2S$  was changed (several times) from 0.06 cc/sec to 0.857 cc/sec while the flow rate of  $H_2$  gas was kept at 6 cc/sec. At each gas flow rate ratio the gas mixture was bubbled through the 300 cc of deaerated 3.4 wt. % NaCl solution with pH of 7.5 for more than 3600 sec.\* Then, pH and sulfide concentration of the solution were measured. The measured sulfide concentrations are plotted against the partial pressure of  $H_2S$  calculated from the equation,

$$\frac{[\text{Flow Rate of } H_2S]}{[\text{Flow Rate of } H_2S] + [\text{Flow Rate of } H_2]} \times 760 = \left[ \begin{array}{c} \text{Partial Pressure} \\ \text{of } H_2S \end{array} \right]$$

assuming atmospheric pressure of 760 mm Hg (Figure 27). One may obtain the sulfide concentration of about 5 to 10 ppm by applying the partial pressure of  $H_2S$  gas at 10 mm Hg.

---

\* It usually takes 1200 seconds to get saturation of sulfide and stability of pH (shown in Table 3).

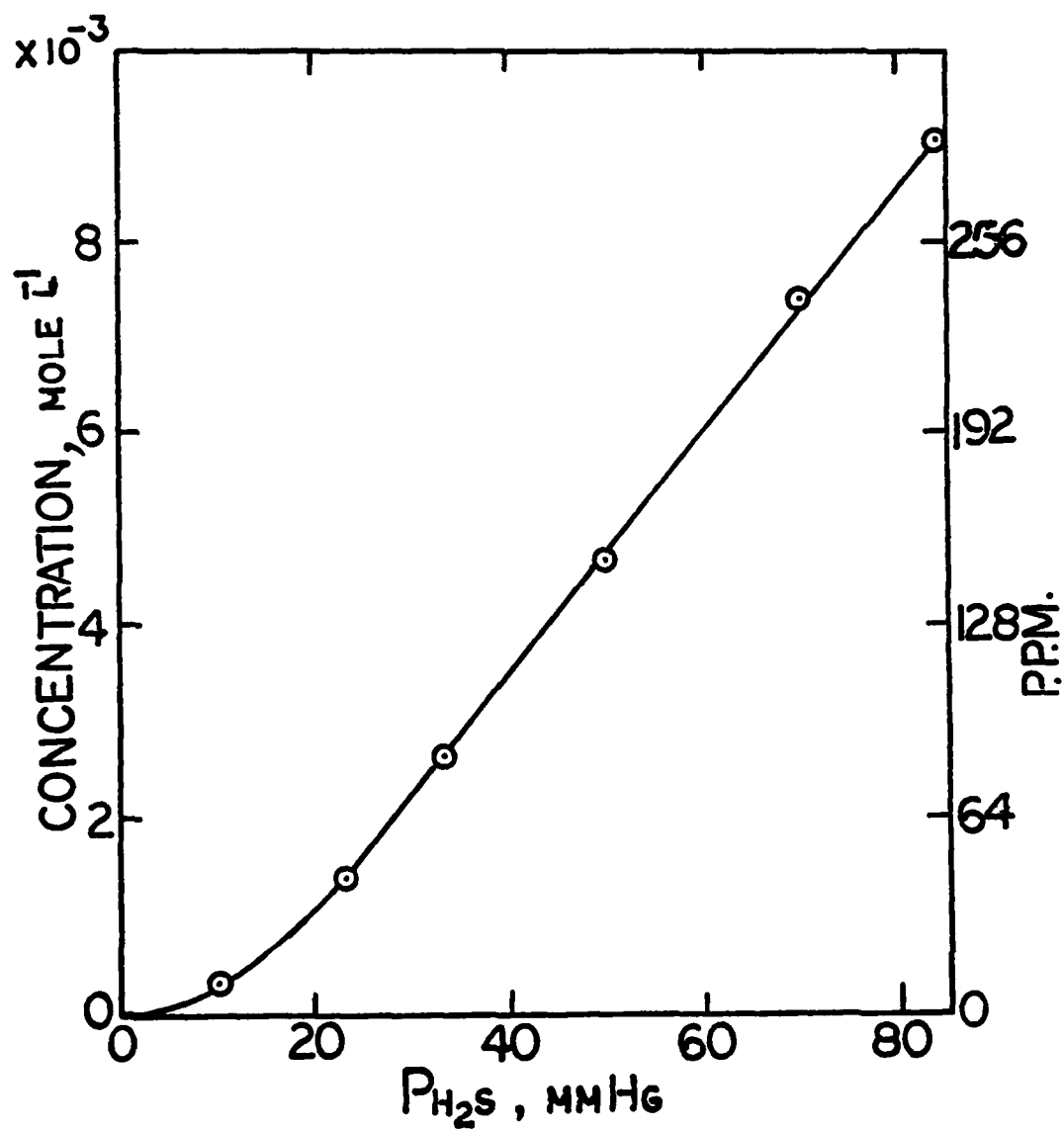


Figure 27. Sulfide concentration versus partial pressure of  $H_2S$  gas ( $P_{H_2S}$ ).

## APPENDIX C

### SULFIDE CONCENTRATION AND pH MEASUREMENTS

In the sulfide concentration measurements a sulfide ion electrode (model 94-16, Orion Research Incorporated, Cambridge, Mass.) was used with a saturated calomel reference electrode (Fisher Electrode, Fisher Scientific Company) and Beckman digital pH and mV meter (model 4500). In order to measure the sulfide concentration with the sulfide ion electrode, a calibration curve of electrode potential vs. concentration of sulfide had to be constructed.

The calibration curve was obtained by measuring the electrode potential of the sulfide ion electrode against the reference electrode in the standard solutions which contain different amounts of sulfide (prepared by dissolving  $\text{Na}_2\text{S} \cdot 9\text{H}_2\text{O}$  into deaerated water and its ten-fold dilutions). The high pH of the sulfide anti-oxidant buffer (SAOB, 200 ml of 10 M NaOH, 35 g ascorbic acid, 67 g disodium EDTA, and about 800 ml distilled water) was always added to the sulfide standard and ensured that the sulfide was present as  $\text{S}^{--}$ . The exact concentrations of these standard solutions were determined by titration with lead perchlorate ( $\text{Pb}(\text{ClO}_4)_2$ ) 0.1 M solution and by electrode potential. The end point was determined by the abrupt electrode potential change. Then, the exact concentration of sulfide was calculated with the following equation,

$$C_s = (C_t/V_s)C_t$$

where

$C_s$ : concentration of sulfide (mol/l)

$V_t$ : amount of lead perchlorate used (ml)

$V_s$ : amount of sample solution (ml)

$C_t$ : concentration of lead perchlorate = 0.1 mol/l

By measuring the electrode potentials of exactly known sulfide concentrations of solutions, the calibration curve was obtained and shown in Figure 28.

To measure the unknown concentration of sulfide solution, first, exactly 20 cc of sample solution was obtained and mixed with SAOB (20 cc). Then, the sulfide electrode and the reference electrode were immersed into the sample solution and the electrode potential was measured. From the obtained potential and the calibration curve (Figure 28) the concentration of the sample solution was identified.

The pH of the solution was also measured. The pH measurements were conducted before the sulfide concentration measurements by using combination electrode and Beckman digital pH meter calibrated with pH 4 and 7 solutions.

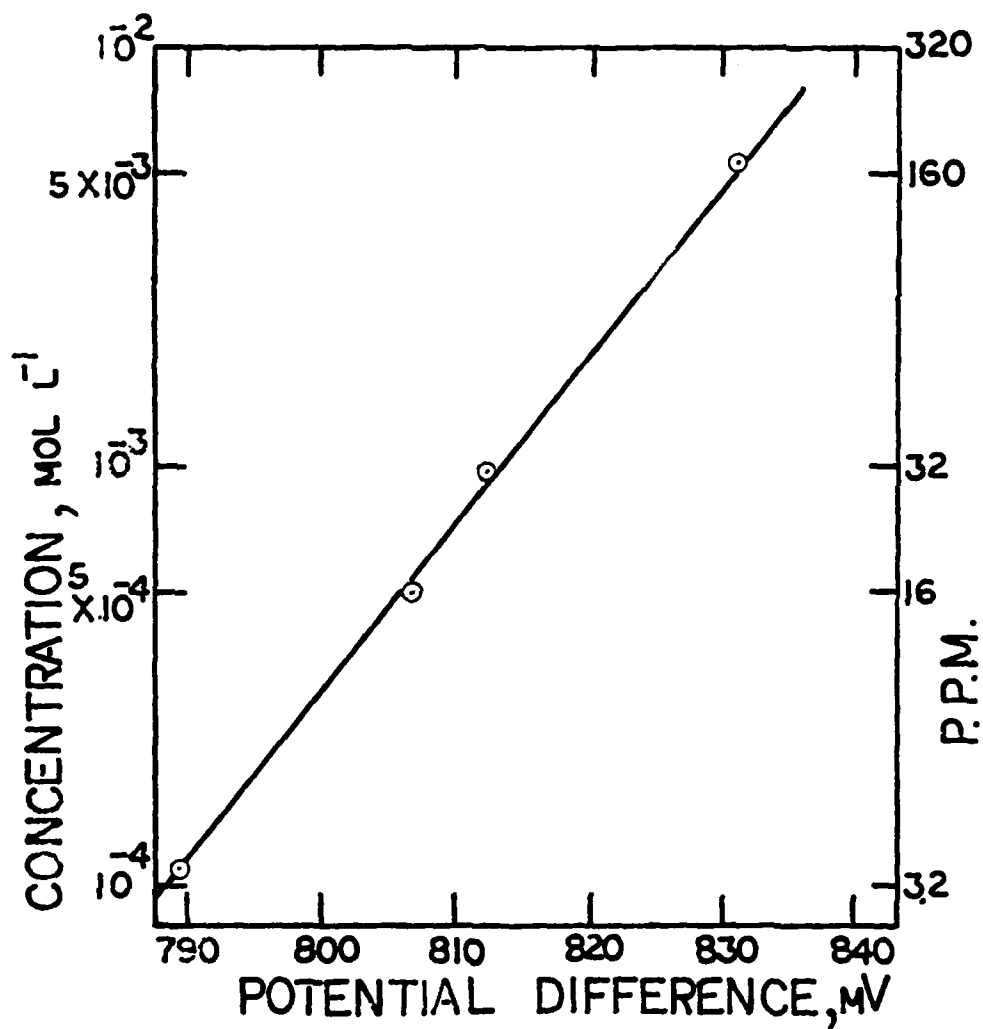


Figure 28. Concentration versus potential difference between the sulfide electrode and the saturated calomel reference electrode.

## VITA

Chiaki Kato was born in Tokyo, Japan, on September 20, 1952. He received his B.S. degree in Metallurgy from Waseda University, Tokyo, Japan, in April, 1975, and entered The Pennsylvania State University in September of that year. He received his M.S. degree in Metallurgy in 1978 and continued his studies in metallurgy as a Ph.D. candidate. While working toward his graduate degrees, he was appointed as a graduate assistant. His tasks as graduate assistant included instruction and research.



DISTRIBUTION LIST FOR TM 81-181

Commander (NSEA 0342)  
Naval Sea Systems Command  
Department of the Navy  
Washington, DC 20362

Copies 1 and 2

Commander (NSEA 9961)  
Naval Sea Systems Command  
Department of the Navy  
Washington, DC 20362

Copies 3 and 4

Defense Technical Information Center  
5010 Duke Street  
Cameron Station  
Alexandria, VA 22314

Copies 5 through 10

DATE  
FILME